Experimental and Numerical Analyses on the Delamination of Beam-Like Geometries at Large Cohesive-Length Scales

by

James Michael Gorman

A dissertation submitted in partial fulfillment
of the requirements for the degree of
Doctor of Philosophy
(Mechanical Engineering)
in The University of Michigan
2019

Doctoral Committee:

Professor Michael Thouless, Chair
Professor Ellen Arruda
Professor John Shaw
Professor Alan Taub
Professor Alan Wineman

James M. Gorman

jagorman@umich.edu

ORCID iD: 0000-0002-5806-9380

DEDICATION

To my family.

ACKNOWLEDGEMENTS

This research was supported by the U.S. Department of Energy (DE-PI0000012), the U.S. Department of Defense (SMART Scholarship), and the University of Michigan Rackham Graduate School (Rackham Conference Travel Grants).

Thank you to my adviser, Michael Thouless, for giving me a chance 6 years ago. There were many professors who were unable or unwilling to take on a physics undergraduate student (with no background in solid mechanics) in a mechanics and materials PhD program. You gave me the opportunity to learn about fracture mechanics, something I have wanted to do for years. I will be the first to say I have more to learn, but I know I have come a long way under your tutelage.

Thank you to John Shaw and Alan Taub for serving on my committee. I am also grateful for Ellen Arruda and Alan Wineman for serving on my committee and your help and encouragement in the early years of graduate school as I learned the new field of continuum mechanics. Thank you to Andy Poli for your non-academia perspective as I finished up my research projects, and for helping me become a better programmer. Thank you to Peter Fritz for being the industry contact and providing the adhesive used in this work, and for reaching out to Michael with the original project.

Thank you to my fellow graduate students and post-docs who have made the years more enjoyable: Jon Estrada, Will LePage, Ben Marchi, Fanbo Meng, Hai Wang, Isha Gupta, Alison Hake, Kisik Hong, Callan Luetkemeyer, Marie Rice, Ryan Rosario, Aritra Sasmal, Madison Strauss, Rachel Vitali, Dandan Wang. In particular: Will, thank you for introducing me to DIC; Fanbo, I appreciate your help very early in my graduate school career when I started learning about mechanical testing of materials; Hai, thank you for helping me get started with CZM modelling.

Thank you to my parents: Joe and Lin Gorman, and Linda Keuneke and Paul Knott. You have always encouraged of my joy of learning, even when it got to the point you had trouble understanding what I was doing. I have especially appreciated your support these past few years.

Thank you to my twin brother Chris. After years of being at the same schools and in the same classes with friendly competition, we finally took separate paths after graduating

from Wabash. But even with you being across the country, you were always there to give an outside perspective, and we were both able to encourage the other when grad school was difficult.

Finally, thank you to my wife Nora. We became friends about halfway through graduate school, and I am thankful for the joy you bring to my life. You have made these last few years more entertaining, and I look forward to the coming years together.

ότι εν αυτῶ εκτίσθη τὰ πάντα εν τοῖη ουρανοῖζ καὶ επὶ τῆζ γῆζ, τὰ ορατὰ καὶ τὰ αόρατα, είτε θρόνοι είτε κυριότητεζ είτε αρχαὶ είτε εξουσὶαιτὰ πὰντα δι′ αυτοῦ καὶ ειη αυτὸν έκτισταὶ καὶ αυτόη εστιν πρὸ πάντων καὶ τὰ πάντα εναυτῶ συνέστηκεν
KOΛ 1:16-17

Εν αρχῆ ῆν ο λόγος, καὶ ο λόγος ῆν πρὸς τὸν θεόν, καὶ θεὸς ῆν ο λόγος. οῦτος ῆν εν αρχῆ πρὸς τὸν θεόν.πάντα δι′ αυτοῦ εγένετο, καὶ χωρὶς αυτοῦ εγένετο ουδὲ έν. ὸ γέγονεν
ΙΩΑΝ 1:1-3

TABLE OF CONTENTS

LIST OF FIGURES

Figure

LIST OF APPENDICES

Appendix

ABSTRACT

Linear-elastic fracture mechanics (LEFM) has been successfully used to model and predict fracture of brittle materials and those undergoing small-scale plasticity. However, with the increasing use of fiber-reinforced composites and rubber-toughened epoxies, LEFM is no longer applicable in these circumstances and other tools must be used to determine crack-propagation. The cohesive-zone model (CZM) is becoming a standard tool to analyze fracture, and it is used here in conjunction with the finite element method to consider the effects of large cohesive-length scales. The cohesive-zone model works by specifying interface separation through characteristic stress-displacement relations (commonly termed cohesive or traction-separation laws). Furthermore, CZM has been shown to bridge the gap between the energy-based and strength-based approaches to fracture.

Over the last few decades, digital image correlation (DIC) has become a standard, non-contact method of analyzing surface deformation. DIC allows sub-pixel displacement measurement, and the quantity of data produced allows one to compare entire specimen results with numerical calculations. When dealing with beam-like geometries, one can use the vast amount of data provided by DIC to reduce error by treating digital data in a continuous (analog) fashion. With this in mind, the work presented here gives a methodology on how one uses full-field measurement techniques to analyze beam-like geometries.

The first specimen analyzed is the symmetric double-cantilever beam (DCB), which is a geometry that is commonly used to extract the mode-I traction-separation law. While many groups have used various methods of extracting the mode-I (opening) traction-separation law using the DCB, the two broad categories generally used are either direct measurement or an inverse method. However, no group has used a directly-measured traction-separation law to predict the cohesive-zone (displacement profile) ahead of the crack-tip. The cohesive-zone measurement was accomplished using the full-field measurement capabilities of digital image correlation. DIC also allows users to measure beam rotation and shear around the crack-tip, and the beam deformation was found to be in good agreement with the treatment of an Euler-Bernouli beam deformation with a root displacement and rotation boundary conditions. It was experimentally observed that the cohesive-length scale evolved during loading, and LEFM predictions agreed with the experimental observations at the smallest resolvable scale.

The single lap-shear joint was the next geometry considered. Initially, the geometry is only loaded via an axial load and bending moment. It has been experimentally observed that the lap-shear joint can behave the same whether a crack or corner is present in the geometry, even though a theoretical analysis using LEFM requires a crack. Here, numerical calculations were run across various fillet angles, and it was observed that the cohesive-length scale determined whether or not the work done against the tractions at a singularity was equivalent to the J-integral. At large cohesive-length scales, all singularities behave the same way and the fine aspects of the fillet angle are swamped by the large cohesive-length. While it has been shown previously that at small cohesive-length scales, when LEFM is expected to be valid, that the phase angle will asymptote to the LEFM value at a crack-tip regardless of the shape of the law, this was not the case for non-crack singularities.

A more detailed analysis of the single lap-shear joint followed. When the lap-shear joint is clamped, an unknown reactionary shear load is imposed on the specimen. This load depends on the traction-separation laws and geometry, and cannot be neglected in general as it can affect the work done at the crack-tip. Geometric constraints were considered, and it was observed that the deformation is pushed towards pure mode-II (in-plane shear) at large cohesive-length scales. To account for the unknown shear load and possible geometric constraints, two methods were developed and carried out on a numerical example: the large-deformation J-integral and the numerical partial-model. The numerical partial-model method was experimentally-validated using the same adhesive characterized by the DCB.

The last aspect considered here is fracture along a dissimilar-material interface. It has been known for some time that LEFM predicts oscillatory stress fields and interpenetration at the crack-tip along a bi-material interface. Even though the cohesive-zone model does not have such a drawback, when dealing with mixed-mode fracture one must know one traction-separation law in order to extract the other. A method around this was was found for an epoxy undergoing cohesive failure (failure within the adhesive layer). The mode-I traction-separation laws describing cohesive failure along a steel-steel interface were found to adequately predict mode-I cohesive failure along a composite-steel interface. Through this assumption, the mode-II traction-separation law was able to be extracted and adequate agreement was found between the experimentally-measured and numerically-predicted cohesive-zone displacements of the lap-shear joint.

CHAPTER 1

Introduction

1.1 Overview

This dissertation is divided into six chapters. This first chapter provides the scope of this work. Furthermore, it provides an introduction to fracture: namely, linear-elastic fracture mechanics and the cohesive-zone model (Section 1.2), and the cohesive-length scale (Section 1.3). Background information is also provided on digital image correlation (DIC) (Section 1.4), which is the non-contact, full-field displacement measurement technique used to analyze the experiments.

Chapter 2 considers the quantitative experimental, analytical, and numerical analysis of the symmetric double-cantilever beam (DCB) geometry. Quantitative replication of experimental results was accomplished, as was the experimental observation of an evolving cohesive-length scale. A detailed method for extracting the mode-I traction-separation law from the DCB is also provided, and this law is validated by comparison of the numerical and experimental cohesive-zone displacements.

Chapter 3 pursues a numerical analysis of the single lap-shear joint when it is loaded only by axial loads and bending moments. The effect of a large cohesive-length scale is considered, in addition to non-180 degree fillet angles (*i.e.* when the geometry does not include a sharp crack). It is shown that at small cohesive-length scales, particularly when LEFM is expected to be valid, the precise nature of the singularity is important; however, as the cohesive-length scale increases the precise nature of the singularity matters less.

Chapter 4 expands on the results of Chapter 3 and considers the loading of the lap-shear geometry via clamped tabs. When loading is done in this way, an unknown shear load and bending moment is applied at the grips and must be considered in the analysis. Geometric constraints on the single lap-shear joint are also considered. A numerical example is analyzed to demonstrate two methods that can be used to account for this unknown shear

load: large-deformation J-integral (valid at small cohesive-lengths) and a numerical partial-model approach (particularly useful when dealing with a constrained field-of-view). The use of a numerical partial-model is experimentally validated using the same adhesive that was characterized in Chapter 2.

Chapter 5 introduces the reader to the unique challenges one faces when considering fracture along a dissimilar-material interface. The significance of the experimental validation results of Chapter 4 are put in context. Finally, the limitations of this method are also considered, along with potential paths forward for this challenge.

Chapter 6 gives some conclusions and provides direction for future work, while Appendix A includes the updated FORTRAN user-defined element (UEL) implemented in Abaqus 6.14 [1] that was used in the numerical calculations performed in this dissertation. This version builds off the work of previous authors [2, 3, 4], and allows for the implementation of a six-part piecewise-linear traction-separation law, with a two-part piecewise-linear compression law. Appendix B is a piecewise-polynomial, C^1-continuous, least squares fitting scheme written in Python 2.7 that was used to fit some of the data.

1.2 Introduction to fracture mechanics

Linear-elastic fracture mechanics (LEFM) has been a standard tool to analyze crack propagation since the 1950s. With the weld failure of numerous Liberty ships [5] during World War II, there was renewed interest to determine why crack propagation occurred. Griffith [6] was the first to quantitatively connect flaw size with crack-propagation, but his analysis assumed perfect elasticity and therefore was only applicable on brittle materials such as glass. Irwin [7] expanded on Griffith's work to include the effect of plastic flow, which allowed crack propagation to be predicted in metals. Further work by Irwin [8] resulted in the common use of stress-intensity factors, with $K_{I,\circ}$[1] and $K_{II,\circ}$ for normal and in-plane shear components, respectively. Being proportional to both stress and displacement, this allowed these quantities to be added vectorially instead of the more-complicated energy relations.

One drawback to LEFM is that it predicts a singular stress field at the crack-tip. This result is physically impossible, as no real material can support an infinite stress but instead will yield first [9, 10] if surface separation (*i.e.* crack propagation) does not occur first [6, 8]. The cohesive-zone model (CZM) is a more-recent model of fracture mechanics that was brought into common use by Hillerborg [11] and Needleman [12] in the 1970s and 1980s. CZM works by using a characteristic traction-separation law defining the normal/shear separation across an interface. An example selection of "uncoupled" laws (explained below) are provided

[1]The "$\circ$" subscript will be used to designate those values which take place at the crack-tip.

in Figure 1.1. The stress response across the interface can be thought of as the resistance (whether through an adhesive layer, van der Waals attraction, hydrogen bonding, etc.) of the two materials being separated from an equilibrium separation. By using a traction-separation law with finite stress values, one removes the singular stress field predicted by LEFM.

The traction-separation laws used in the cohesive-zone model fall into two basic categories: coupled and uncoupled laws. Coupled traction-separation laws [13, 14] recognize the reality that, in general, normal and shear stresses may be dependent on both the normal and shear displacements across an interface. One example of this is in fiber-reinforced composites [15], where fiber-bridging across the interface may cause a shear displacement to induce a normal stress or *vice versa*. As a simplification, particularly when dealing with failure along an isotropic interface (*e.g.* an adhesive layer), one often makes the assumption that normal displacements only induce normal stresses and shear displacements only introduce shear displacements; such laws are uncoupled. This has been shown [3, 16, 17, 4] to adequately describe some experimental systems.

When uncoupled laws are used, a failure criterion must be implemented. It has been experimentally observed that the mixed-mode failure criterion

$$\frac{W_I}{\Gamma_I} + \frac{W_{II}}{\Gamma_{II}} \geq 1 \tag{1.1}$$

can adequately describes crack propagation and failure in some instances [18, 19, 3, 20, 16, 17], where W_I/W_{II} are the mode-I/-II work done by the tractions along the interface and Γ_I/Γ_{II} are the mode-I/-II toughness. While this failure definition could be extended to include the effects of out-of-plane shearing (mode-III fracture) [21, 22], this dissertation only considers planar geometries and therefore this generalization is not considered. The benefit to this formulation is that the failure evolves as loading progresses as a function of the traction-separation laws, without other pre-defined measurements.

It has often been observed experimentally that crack-propagation is mode-dependent [2, 23, 16]; that is, the minimum energy required to drive crack-propagation matters if the crack-tip is opening, shearing, or some combination thereof. From LEFM, the stress-intensity factors determine the phase angle [24, 19], $\psi_\circ$, or mode-mixity at the crack-tip[2]:

$$\psi_\circ = \tan^{-1}\left(\frac{K_{II,\circ}}{K_{I,\circ}}\right). \tag{1.2}$$

[2]This result is rigorously true only when the second Dundurs parameter [25], $\bar{\beta}$, is zero. The complications of analyzing a system when $\bar{\beta} \neq 0$ will be considered in Chapter 5.

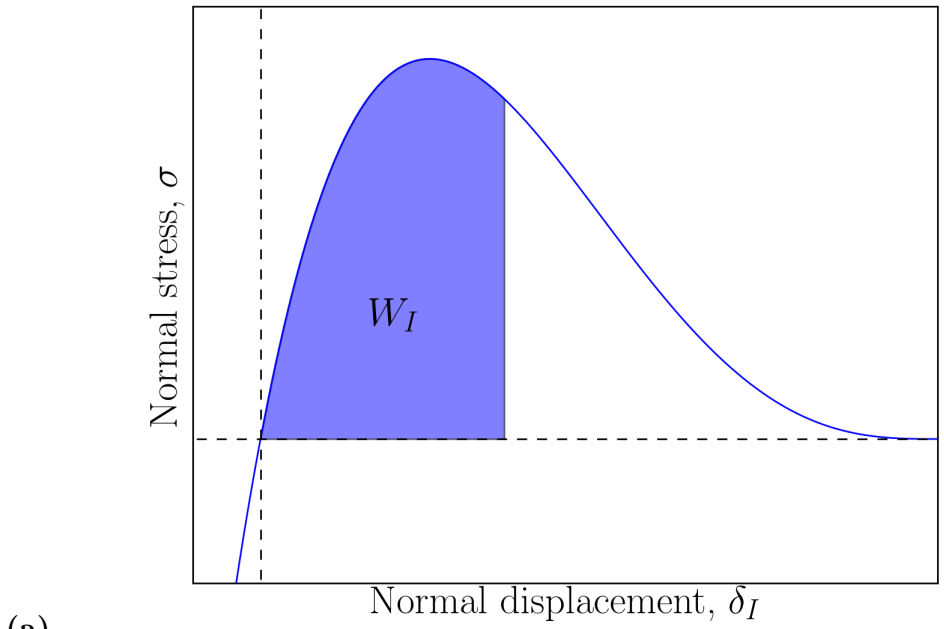

(a)

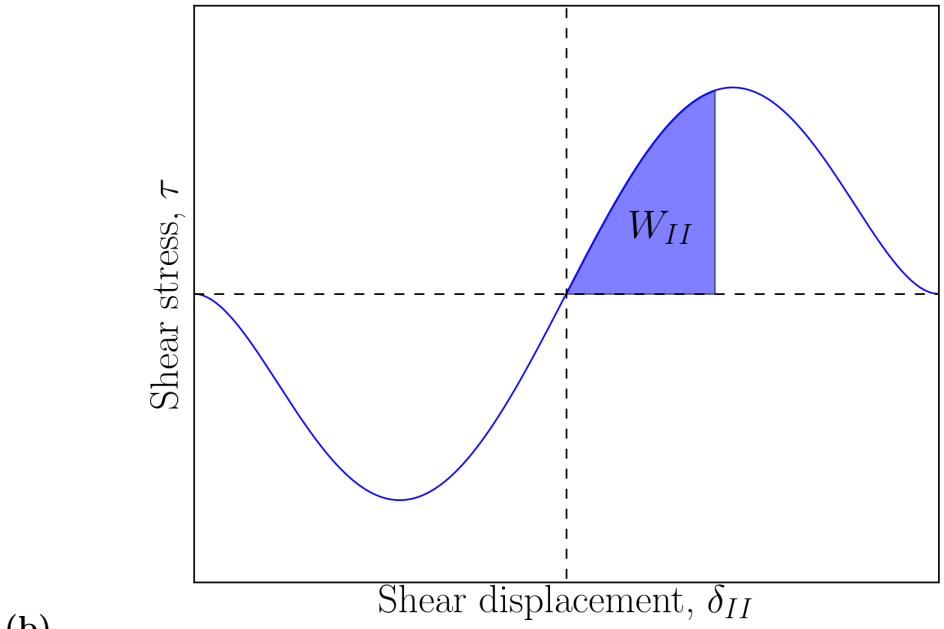

(b)

Figure 1.1: Prototypical (uncoupled) traction-separation laws for **(a)** mode-I (normal) and **(b)** mode-II (in-plane shear). The total area under the mode-I/-II curves is the normal/shear toughness Γ_I/Γ_{II}, while the area swept out from the curve, W_I/W_{II}, is normal/shear work done against the tractions, respectively. The laws are assumed to be uncoupled: the normal stress depends only on normal displacements while the shear stress depends only on the shear displacements. Tractions/stresses resist the interface's removal from equilibrium. In mixed-mode loading, failure occurs when a failure criterion, such as Equation (1.1), is satisfied. Please note that no energy dissipation occurs along the interface until the failure criterion is met.

Therefore, for pure mode-I loading ($K_{II,\circ} = 0$) $\psi_\circ = 0°$, and for pure mode-II loading ($K_{I,\circ} = 0$) $\psi_\circ = 90°$. When using the cohesive-zone model, the phase angle can be defined [3, 20] in a similar manner

$$\psi = \tan^{-1}\left(\sqrt{\frac{W_{II}}{W_I}}\right), \tag{1.3}$$

although the advantage of CZM allows the phase angle to be defined along the entire interface and not just at the crack-tip. While other definitions will use displacements or stresses to define a "phase angle", Equation (1.3) has been shown to approach the LEFM values in the appropriate limit [26, 27].

1.3 Cohesive-length scale

The cohesive-zone model has been shown [26] to bridge the gap between the energy-based (*i.e.* LEFM) and strength-based approaches. Whether energy or stress is the primary driving force behind fracture is determined by normalizing the cohesive-length, ξ, by a characteristic length, l,

$$\bar{\xi} = \frac{\xi}{l}. \tag{1.4}$$

The cohesive-length may be defined for mode-I, -II, or -III; however, as mentioned above this dissertation only considers planar geometries, and therefore analyses will be restricted to mode-I and mode-II fracture. When the mode-I cohesive-length scale $\bar{\xi}_I$ and mode-II cohesive-length scale $\bar{\xi}_{II}$ are the same, the cohesive-length scale will be specified as $\bar{\xi}$. A subscript will be used to specify which fracture mode is being considered when the two cohesive-length scales may not be the same. The normal cohesive-length [28] is defined as

$$\xi_I = \frac{\bar{E}\delta_{I,\circ}^2}{W_{I,\circ}} \tag{1.5}$$

while the shear cohesive-length is

$$\xi_{II} = \frac{\bar{E}\delta_{II,\circ}^2}{W_{II,\circ}} \tag{1.6}$$

where $\bar{E}$ is the elastic modulus, $\delta_{i,\circ}$ is the normal ($i = I$) or shear ($i = II$) displacement at the crack-tip, and $W_{i,\circ}$ is the normal ($i = I$) or shear ($i = II$) work done against the tractions at the crack-tip (energy-release rate). In the case of mixed-mode loading, one can use the previous definitions to define the composite (average) cohesive-length, ξ^*, as

$$\xi^* = \frac{W_{I,\circ}\,\xi_I + W_{II,\circ}\,\xi_{II}}{W_{I,\circ} + W_{II,\circ}} = \frac{\bar{E}(\delta_{I,\circ}^2 + \delta_{II,\circ}^2)}{W_{I,\circ} + W_{II,\circ}}. \tag{1.7}$$

In general, a cohesive-length scale may be defined for singularities other than a sharp crack, and this is considered in Chapter 3.

1.4 Introduction to digital image correlation

The experiments run in this dissertation were analyzed using the experimental measurement technique known as digital image correlation (DIC). DIC is a non-contact method for measuring full-field surface displacements [29, 30] that has become commonplace in the last couple of decades [31, 32, 33, 34, 35, 36]. The method uses a speckle pattern to track the motion of an objects surface. Although natural speckle patterns may be used, many materials do not possess the semi-random, uniform pattern necessary for good correlation. Therefore, speckle patterns often need to be applied to the surface, with two commonly used materials being paint [35] and nanoparticles [37]. Once the speckle pattern has been applied to the sample, an imaging source (for this work, grayscale cameras) captures surface deformations. The grayscale pixels are converted into a smooth surface (cubic-splines are a common interpolation method), and the subsequent pixel motion is tracked for each deformed image. DIC's current theoretical displacement limits are around 0.01 pixel [38]; however, most measurements will have uncertainties larger than this due to other experimental uncertainties (*e.g.* setup vibration, poor speckle quality, saturated pixels, etc.). For additional information on using DIC, the interested reader is referred to Refs. [39, 40, 41].

CHAPTER 2

Analysis of the Double-Cantilever Beam Geometry

2.1 Overview

As mentioned in the introduction, the cohesive-zone model has become a powerful tool for analyzing fracture. Many groups [2, 23, 42, 43, 44] have spent time extracting traction-separation laws, but often the focus of these works has been to only match/predict load-displacement curves. This work distinguishes itself from others in that it captures the deformation of the cohesive-zone ahead of the crack-tip *and* looks to predict adhesive deformation using the independently-measured traction-separation law.

The double-cantilever beam (DCB) was first used to extract fracture properties in 1930 by Obriemoff [45] to analyze mica. When loaded by pure bending moments, the analysis is simplified because the energy-release rate is valid for all cohesive (traction-separation) laws. The downside to the moment-loaded geometry is that one must use special loading rig [46, 47], and this has yet to become standard laboratory testing equipment.

The more common variant of the DCB is where the specimen is loaded via a pin joint at the crack mouth [48, 49, 50]. While these specimens may be easier to manufacture, they are more difficult to analyze because the geometry is loaded by an applied shear load in addition to the bending moment [51, 52, 53]. While many approaches [54, 51, 52, 55, 53, 56, 57, 58, 59, 60] have been used to account for the shear load, Thouless [61] recently unified these analyses.

When one uses a pin-joint to apply a shear load to the DCB, there are various ways one can extract the energy-release rate [62, 63, 64] that do not require a measured crack-length. As will be shown here, the most convenient method to determining this is via the J-integral [65], whereby one takes a contour along the outside of the DCB specimen and needs only to measure the load/width P_∞ and the rotation Θ at the points of loading [66, 67, 68] to give

$$J_{ext} = P_\infty \Theta. \tag{2.1}$$

If one measures the crack-tip opening displacements, $\delta_\circ$, at the same time as J_{ext} for a symmetric specimen, one can differentiate the curve to generate the mode-I traction-separation law [69], or

$$\sigma(\delta_\circ) = \frac{dJ_{ext}}{d\delta_\circ}. \tag{2.2}$$

This approach is used for the work in this chapter, and has been used by others before [70, 71, 43, 44]. Other than this direct method, another approach that has been used by groups is an inverse method [72, 73, 74] whereby measured displacement fields (strains could also be used) are used to back out the traction-separation law from subsequent numerical calculations.

As will be shown in this chapter, the benefit of using the direct method when using DIC is that it allows one to run a separate numerical calculation and compare deformation ahead of the crack-tip with the experimental measurements. Furthermore, the full-field displacements allow one to measure rotations, shear strain [61], an evolving cohesive-length scale [27, 28], and the need for compression in a cohesive law [26]. With full-field measurement techniques now commonplace in labs, the method below provides a guide for those wanting to carefully analyze beam-like geometries and compare extracted cohesive laws with experimental measurements.

2.2 Experimental methods

The geometry used for the work in this chapter is found in Figure 2.1. The beams were made from 4.8 mm thick sheets of 4130 steel, which had a yield strength of 340 MPa [75]. The arms were cut to length of 152 mm, at which point they were milled to a thickness of 21.4 mm. Bonding surfaces were prepared using 100-grit sandpaper, after which a layer of a two-part epoxy (Dow Betamate® 73326M/73327M) was applied onto the surface of one of the beams. 250 micron diameter glass spheres were sprinkled on top of the adhesive layer to ensure a uniform thickness. The second beam, which included Teflon® tape that was used as a starter-crack, was then placed on top of the first beam. After alignment, the sample was clamped using binder clips for two days. The clips were then removed, and the adhesive continued to cure at room temperature for another week. After curing, excess adhesive was ground off and optical observations noted the adhesive thickness was 275 ± 25 microns.

The tabs were made from 3 mm thick, L-shaped, low carbon steel. They were bonded to the system using the same two-part epoxy used for the adhesive layer. The DCB was loaded via pin joints in the tabs, and a lubricant was sprayed on to reduce any friction effects. After polishing the sides of the DCB with 100-grit sandpaper and then 600-grit sandpaper, a black

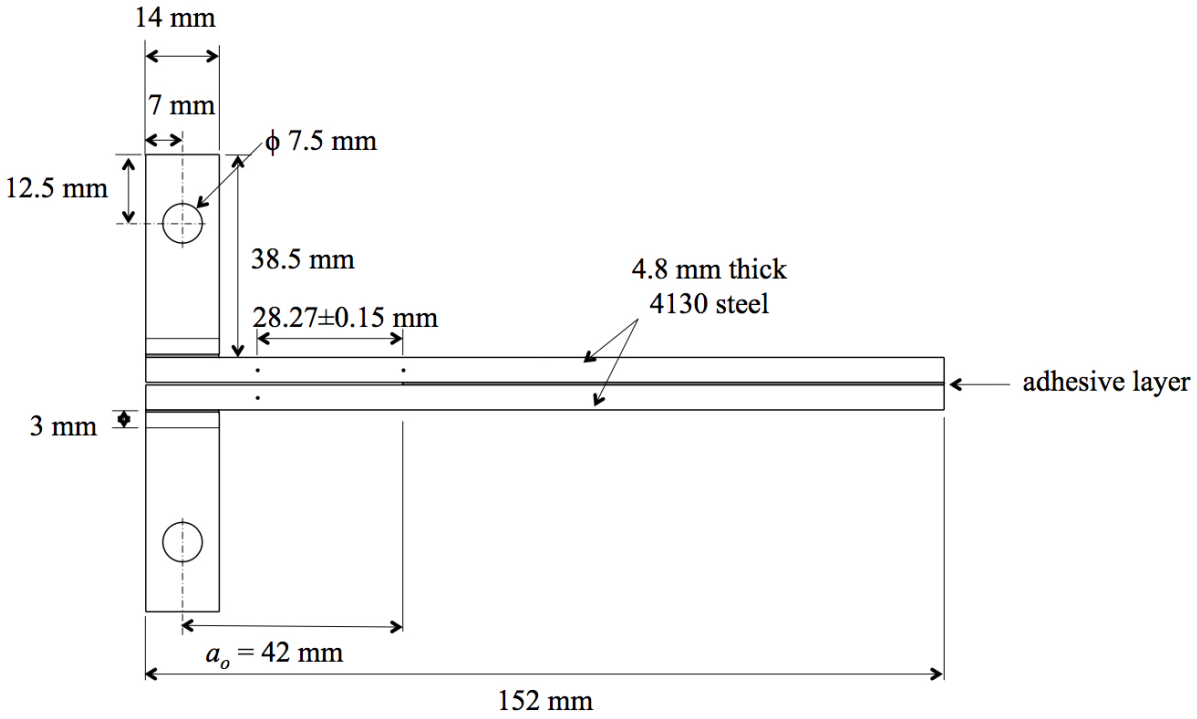

Figure 2.1: Above is an engineering diagram of the double-cantilever beam geometry used in this analysis. The adherends are made of a 4130 steel and are bonded by a two part, structural epoxy (Dow Betamate® 73326M/73327M).

speckle pattern was applied on top of a white basecoat using an Iwata™ CM-B airbrush. Testing was run within 24 hours of the application of the speckle pattern using a servo-hydraulic test machine (MTS 858 MiniBionix II™), which had a cross-head displacement rate of approximately 1.15 mm/min. The original crack length, $a_\circ$, measured from the crack-tip to the center of the loading tabs, was 42 mm. For DIC analysis, two 5-megapixel Grasshopper™ cameras were used to provide synchronized viewing of two separate views: one larger field of view to see beam deformation at the crack-mouth, and a closer field of view to view crack-tip deformation. The commercial software Vic-2D™ was used for (local) DIC analysis. For this analysis, step and subset sizes of 3 and 35 pixels were used, respectively.

Blindly using DIC as a black-box results in excessive noise and differentiation artifacts, particularly when one differentiates the displacement data to acquire strains and/or rotations. In Euler-Bernoulli beam theory, one assumes that plane sections remain plane and this was used for an analog approach for data analysis. Along the length of the beam, vertical lines ("planes") of data were fit with affine approximations and the resulting strains or rotations were calculated. The reader will see in the following sections this allows users to analyze data appropriately in addition to disregarding numerical artifacts.

2.3 Experimental results

2.3.1 Traction-separation law extraction

As noted above, the raw displacement data was used for all calculations rather than relying on the commercial software's numerical output of strains or rotations. Figure 2.2a shows a colormap depicting the vertical displacement of the top beam at load point D (see Figure 2.3 for this definition). Over 4000 data points are shown on this colormap, and yet when the data is plotted as the vertical displacement as a function of the horizontal position along the beam, the results collapse onto a single line. This is displayed in Figure 2.2b for loads A-E (as defined in Figure 2.3). By differeniating the slope of these lines, one finds the rotation of the beam at the point of loading[1]. The same analysis was used for the bottom beam, and the difference in rotations between the two beams, Θ, could be measured and plotted against the applied load, as shown in Figure 2.3. In particular, load points "A" through "E" will be considered in more detail throughout this chapter[2]. Looking at the load-rotation curve, the results may appear to be linear between points "A" and "D". However, it will be shown below true linearity is only valid at loads before point "A" at values smaller than about 1 N/mm.

Strictly speaking, the bonded tabs extended over a finite length of 14 mm, and this may have impacted the measurement of the rotations and, therefore, the validity of Equation (2.1) for the J-integral. This can be verified by changing the location of where the rotations are measured. By changing the location, however, the beam is acted upon by both an applied shear load P_∞ and bending moment $P_\infty l$, where l is the distance from the applied shear load to the point where the rotation is measured. This changes the J-integral to

$$J_{ext} = P_\infty \Theta + \frac{12(P_\infty l)^2}{\bar{E} h^3}. \tag{2.3}$$

Through comparison of the two results, it was determined for this case the correction was negligible.

Using the small field of view images, one can visually identify the location of the crack-tip. This point was also confirmed as the point at which image correlation was lost [76]. Of course, while the vertical location of the crack-tip was known, its position within the adhesive layer was not. Furthermore, though thickness of the adhesive layer is known, the speckle pattern covered up its precise location. To solve this issue, the vertical displacement, v, was plotted as a function of the vertical location, y, at the crack-tip (Figure 2.4a). These

[1] It was determined that the shear effects were negligible.

[2] It should be noted that load points "A" through "E" are distinct from those load points defined in Chapter 4.

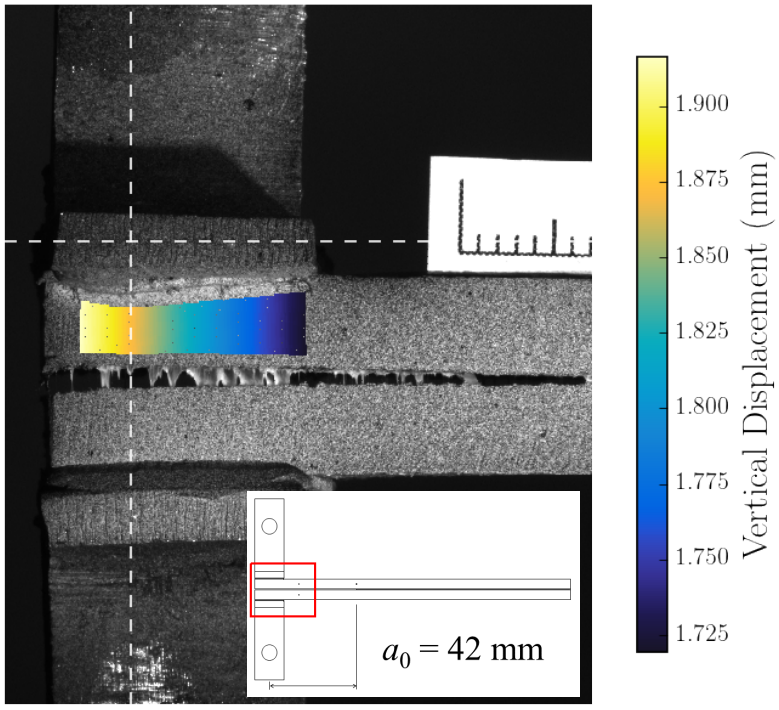

(a)

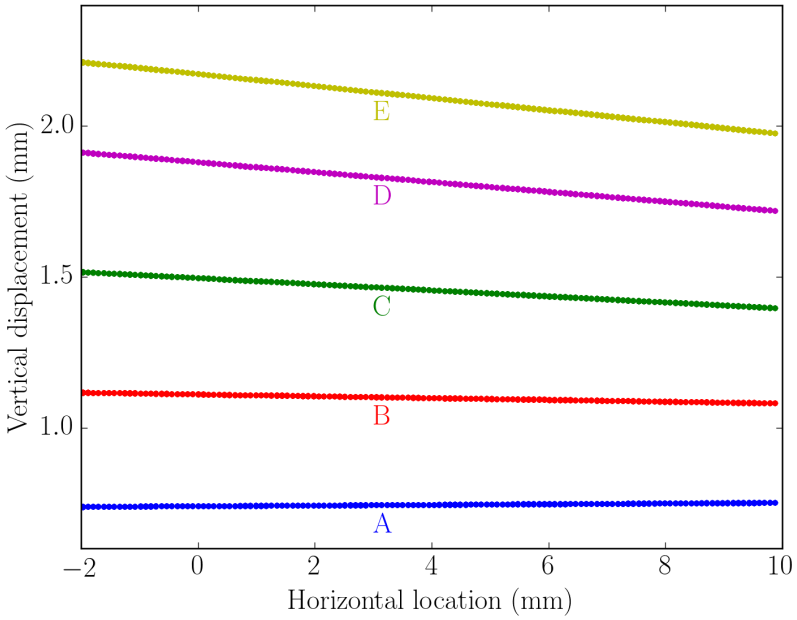

(b)

Figure 2.2: From the results above one sees there exists uniform rotation at the load points. The image in **(a)** shows a color map containing vertical displacement data for one beam, which includes over 4000 data points. Five particular load points (A-E are defined in Figure 2.3) are shown in **(b)**, and it is seen that in each case the results collapse onto a single line. Therefore, one sees the beams are in a state of uniform rotation at the load point. It should be noted that there is no bridging of the adhesive across the interface at the crack-mouth. The white material seen inside the crack-mouth is the Teflon® tape used for the pre-crack.

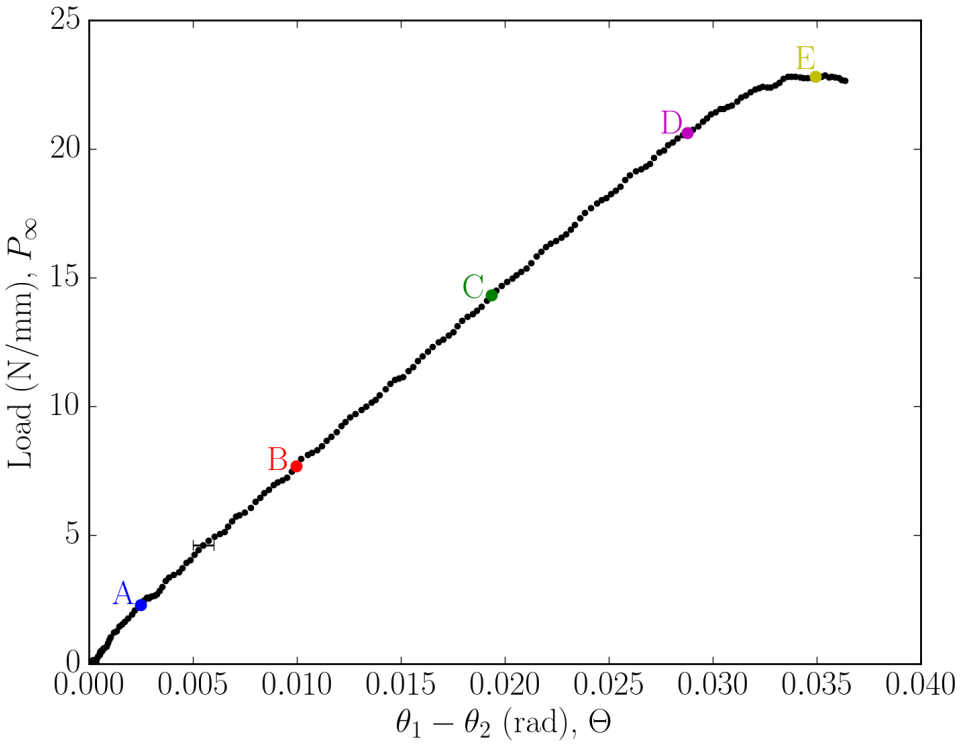

Figure 2.3: By taking the difference of the top and bottom beam rotations at each load point, one can plot the relative rotation against the applied load.

results for five different load points can be found in Figure 2.4b, where one sees a sharp change in the normal strain $\varepsilon_{yy} = dv/dy$ in the steel adherend and epoxy adhesive. This allows one to measure the opening displacement.

Taking a close look at Figure 2.4b, it is worth noting that the measured normal strain ε_{yy} is incorrect. As mentioned above, before the addition of the speckle pattern the adhesive layer was observed to be between 250 - 300 microns. However, here one sees a transition (the "interface region") about 0.6 mm wide. As a consequence of local, subset-based DIC, the displacements are smoothed out beyond the true adhesive/adherend interfaces. The extent of this smoothing is dependent upon the subset size, and the experimentalist needs to balance the increased noise of a small subset size and the larger transition region[3].

While DIC cannot be used to calculate the adhesive layer thickness, one can still measure the opening displacements across an interface by taking measurements just outside of the transition region since the strain in the steel is small[4]. If one were testing a system with adherends that were more compliant than steel, one may need to extrapolate the displace-

[3]Higher camera resolution, a finer speckle pattern, and smaller subset size may also help decrease this smoothing.

[4]In comparison with the manufacturer's datasheet, the adhesive is quoted [77] to have an elastic modulus two orders of magnitude smaller than the steel.

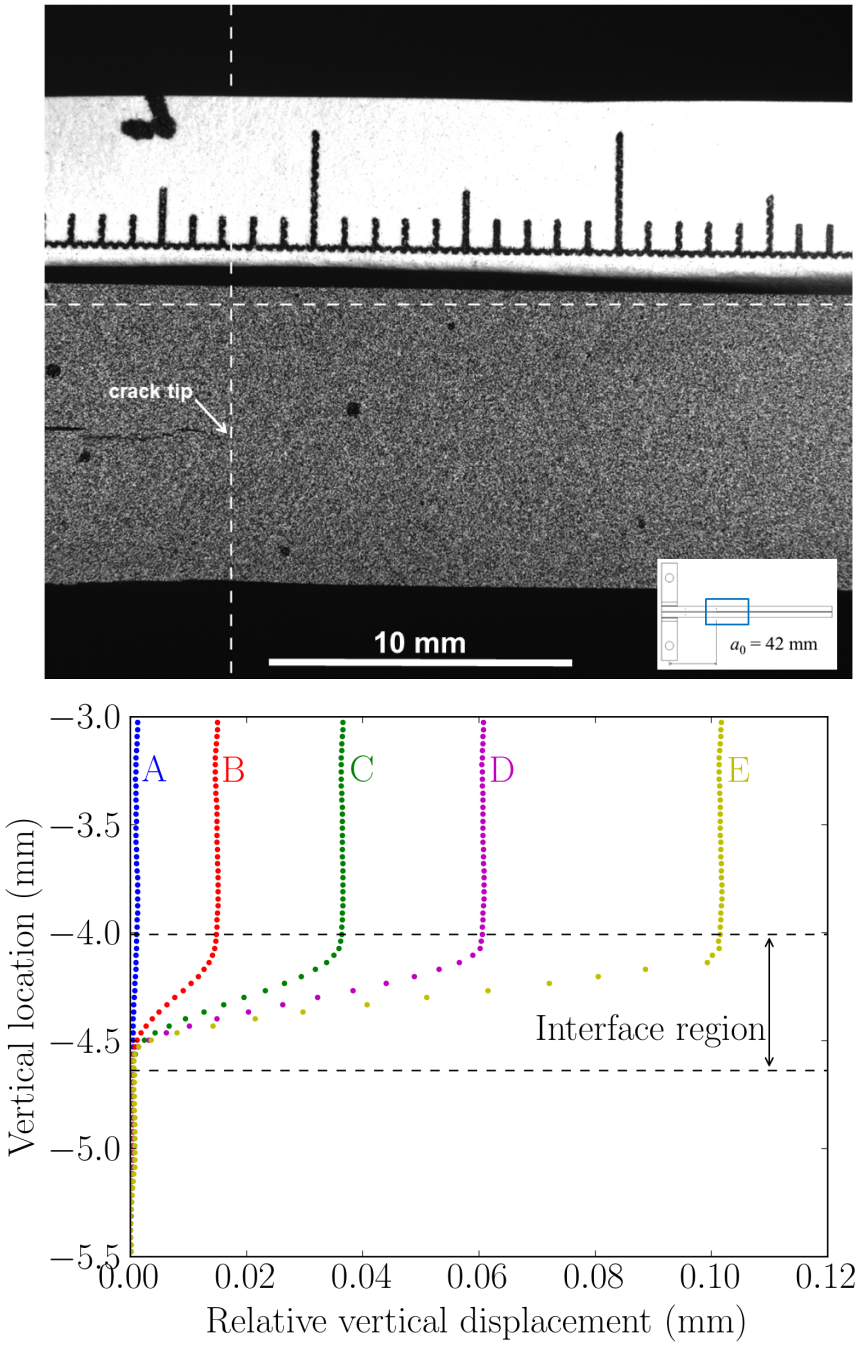

Figure 2.4: Calculation of the crack-tip opening. **(a)** shows a deformed image with the identified crack tip, with the coordinate system inscribed. The vertical axis has been shifted to coincide with the crack-tip. **(b)** shows a plot of the relative vertical displacement as a function of the vertical location. The dotted lines mark the interface region (where the displacements were measured), which one will notice to be much larger than the adhesive thickness that was between 250-300 microns.

ment data to the assumed interface locations. Additionally, due to the use of subset-based DIC, one would incorrectly measure the opening displacements if one directly measured the displacements over only the 275 ± 25 microns of the known adhesive layer. The problems associated with interfacial smoothing might be fixed by using extended digital image correlation (X-DIC), which can handle displacement discontinuities [78, 79]. However, it was beyond the scope of this work to consider this extension.

The crack-tip opening displacement calculations were done for all images acquired during the test. Minor rigid-body rotation corrections were done to correct for any rigid-body rotations that might impact the results. In this case, the coordinate system used had the x-axis lying along the interface and the y-axis perpendicular and pointing toward the surface. Therefore, the crack-tip opening displacement across the interface was computed as:

$$\delta_\circ = \Delta v' cos(\theta) - \Delta u' sin(\theta) + t\,(1 - cos(\theta)) \tag{2.4}$$

where $\Delta v'$ and $\Delta u'$ are the measured displacement differences along the y-axis and x-axis (respectively), t is the thickness of the interface region (*not* the adhesive layer), and θ is the rigid-body rotation about the z-axis. In this instance, the rigid-body rotation correction was smaller than the experimental uncertainty.

Using the load and (relative) rotation data from Figure 2.3, the far-field J-integral was calculated using Equation (2.1). These data were then plotted against the crack-tip opening displacement, and the resulting curve can be seen in Figure 2.5. One should note that J_{ext} is equal to the work done against the tractions at the crack-tip, $W_\circ$. This crack-tip work, $W_\circ$, can then be combined with the elastic modulus of the steel (217 GPa)[5] and the crack-tip opening displacement, along with the beam thickness h as the characteristic geometric length, to compute the (instantaneous) cohesive-length scale during loading. Points "A" through "E" have been identified on Figure 2.5, and the corresponding cohesive-length scale has also been included. As one can see, even at load "A", the smallest identified load, LEFM would no longer be considered a useful approximation.

In Figure 2.5, one notes that the crack began propagating before J_{ext} began to level off. This indicated the crack front was not uniformally propagating within the adhesive layer. At the end of the test, it was observed a thin (< 0.5 mm) layer of adhesive failed via adhesive failure (along the steel-adhesive interface) while the rest of the system failed via cohesive failure (within the adhesive layer). This highlights one drawback of DIC: surface deformation says nothing about what is occuring underneath. In order to continue the analysis, it was assumed the measured surface displacements was a reasonable approximation to the through-

[5]This elastic modulus of 217 GPa is determined in Section 2.3.3 using the experimentally-measured crack-mouth displacements.

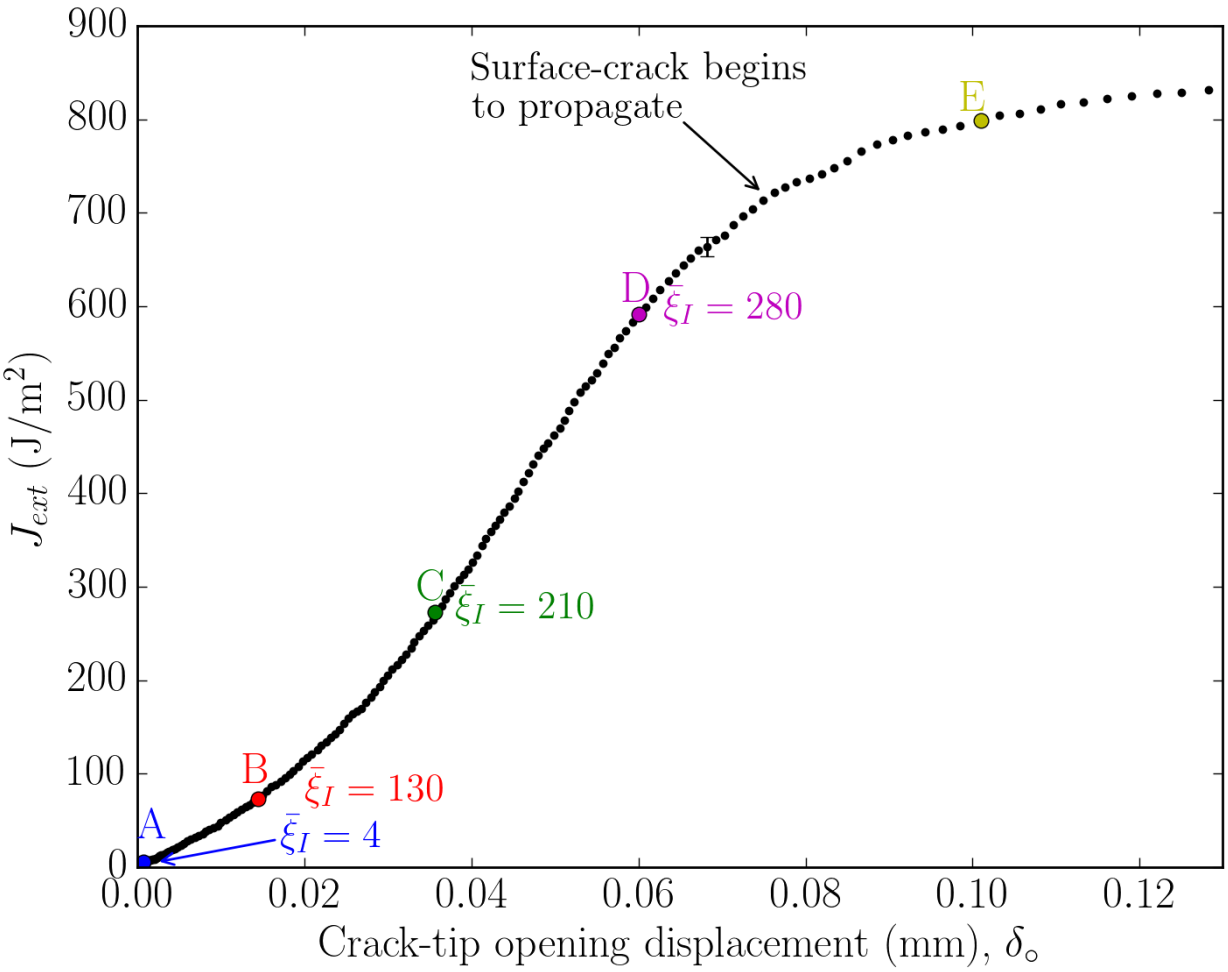

Figure 2.5: The J-integral was calculated using Equation (2.1), from the product of the load and relative rotation at loading points (Figure 2.3). This figure presents J plotted against the corresponding crack-tip opening displacement (obtained from data such as those shown in Figure 2.4). The instantaneous cohesive-length scales were calculated for the reference points using the appropriate values of the J-integral, opening displacement, and an elastic modulus taken to be 217 GPa (as calculated from the data shown in Figure 2.8). It should be noted that the surface crack began to propagate at a load between D and E. The J-integral was still rising at this point and observations following the test indicated on a surface-crack was propagating. Therefore, the appropriate value of the opening displacement is ambiguous after this point, but it was assumed the measured displacements were a reasonable measure of the deformation through the thickness of the specimen.

thickness displacements.

Calculation of the mode-I traction-separation law just involves differentiating the data in Figure 2.5, as specified in Equation (2.2). This differentiation was done using a custom piecewise polynomial, C^1-continuous, least squares fitting scheme (Appendix B) to fit large sections of data. This differentiated curve is given in Figure 2.6. While one might be able to use a ruler to fit a broad peak around 25 microns with a constant stress of around 13 MPa[6] between points "C" and "D", no digital differentiation scheme was able to reproduce this analog approach. The dashed line in Figure 2.6 stipulates the results following the surface-crack propagation to emphasize its uncertainty.

While multiple samples were tested, the results for only one specimen are included in this chapter. Results across the samples were consistent with steady-state toughness and strengths, with about 10% variation in the parameters. All analyses in this chapter refer to a single sample.

2.3.2 Root rotation

Because of the specimen geometry, the DCB beams at the crack-tip are subjected to both shear and rotation [51]. The shear is the result of the applied load via a pin joint, while the rotation is due to the fact that the arms are elastic and not rigidly clamped at the crack-tip. From these phenomena, there exists a relative rotation between the centroidal axes of the beams at the crack-tip, which is termed the root rotation. This root rotation increases with the cohesive-length scale (Figure 2.11), along with a case for perfect bonding when $\bar{\xi}_\circ = 0$ [61].

The root rotation is measured using the full-field measurement capabilities of DIC. Using the same vertical line from which the crack-tip opening displacements were determined (Figure 2.4), one now measures the relative horizontal displacement as a function vertical position along this line. This data is shown in Figure 2.7a. Note that this is the raw data which has not been corrected for any rigid-body rotation. The root rotation can then be found as the relative rotation between the two arms. Outside of the interface region (where the adhesive layer undergoes relatively large deformation), it is obvious the assumption of uniform rotation is appropriate. If one looks closely, one can see some of the fine structure that is a result of the DIC analysis. This is an example of a numerical artifact one must be careful not to propagate by blindly differentiating DIC displacement data.

[6]When uniform tension experiments were run using the same adhesive/steel system, the maximum stress determined in these experiments was about half the cohesive strength in Figure 2.6. However, DIC showed that this "uniform" tension experiment was not actually uniform, and therefore this lower experimentally-measured value is consistent with the DCB results.

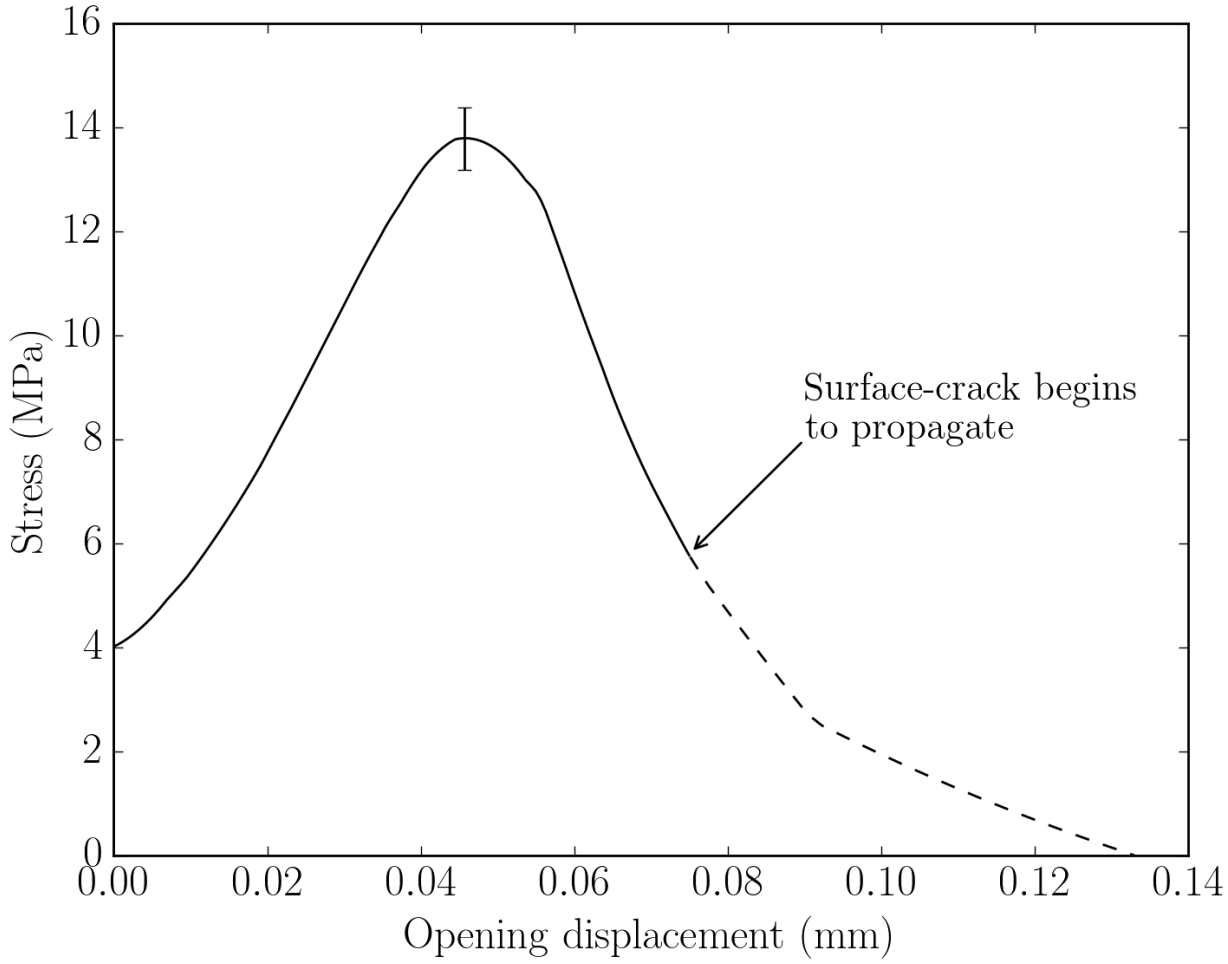

Figure 2.6: Traction-separation law obtained by differentiation of a curve fit to the data in Figure 2.5.

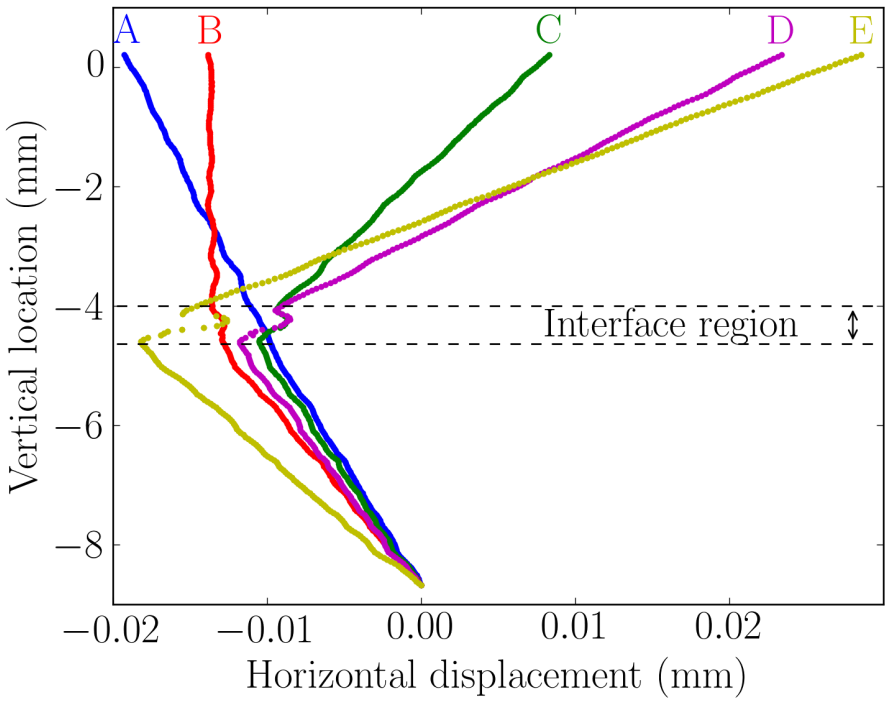

(a)

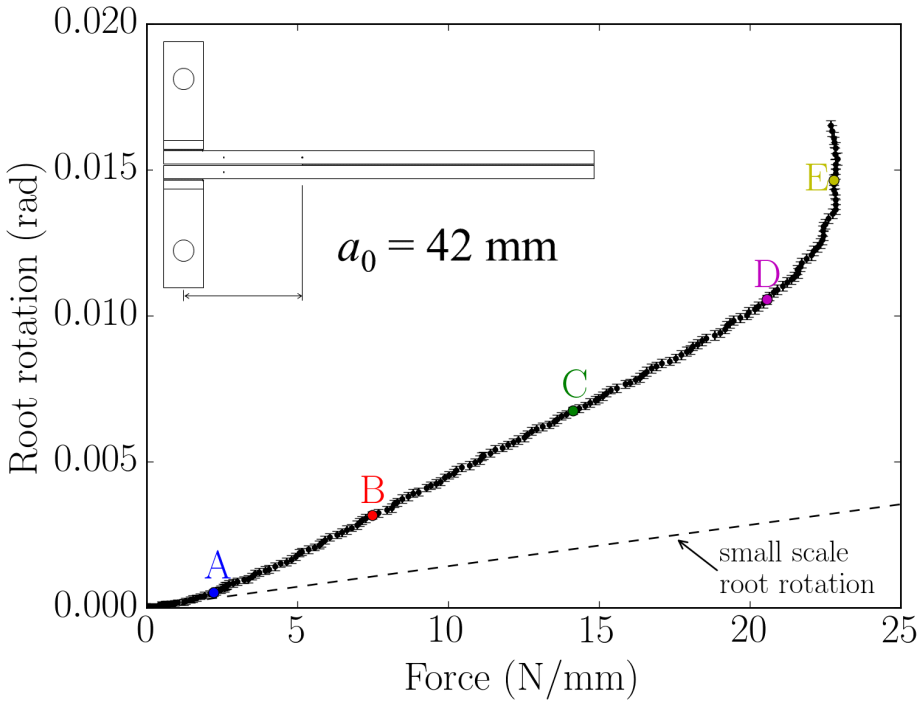

(b)

Figure 2.7: Calculation of root rotation. **(a)** Shows plots of relative horizontal displacement as a function of vertical location at the crack-tip region for the specific loads identified in Figure 2.3, using the same coordinate system specified in Figure 2.4a. Some fine structure in the data may also be observed, which are likely due to the interpolation functions of DIC. **(b)** Shows how the root rotation, defined as the difference in the values of du/dy for both arms, varies with increasing load. The small-scale root rotation is also inscribed on this plot, calculated for the DCB geometry of this paper and an elastic modulus of 217 GPa (see Figure 2.8).

The root rotation $\theta_\circ$ is plotted as a function of load in Figure 2.7b. Please note that the root rotation is defined as the relative difference of du/dy between the top arm and the bottom arm (using the same coordinate system from before), and therefore any effects from the shear load are included. As shown in Ref. [61], this allows one to describe the compliance of a DCB using an Euler-Bernoulli beam and a root rotation (this is expanded upon in Section 2.3.3). The predicted small-scale root rotation from LEFM ($\theta_\circ = P_\infty(5.44 + 16.2a_\circ/h)/(\bar{E}h)$) is inscribed on Figure 2.7b[7].

The only time when the small-scale root rotation accurately replicates the experimentally-measured root rotation is before point "A". This is consistent with the cohesive-length scale results from Figure 2.5 that noted point the CLS at "A" was too large for LEFM to be considered a useful approximation. Therefore, one does not expect the root rotation results after point "A" to coincide with linear-elasticity.

2.3.3 Elastic modulus

As shown in Ref. [61], one can include shear effects at the crack-tip into a root rotation. The compliance of the DCB can then be described by Euler-Bernoulli beam theory, provided one includes the root rotation and displacement[8] as a boundary condition. The crack-mouth opening displacement was evaluated away from the tabs to remove any effects the bonded tabs had on the opening displacement. Therefore, as noted in the engineering diagram (Figure 2.1), the crack-mouth opening displacement was evaluated $a = 28.3$ mm behind the crack-tip. As noted before, when not evaluated at the loading point, the beam is subjected to both an applied shear load, P_∞, and bending moment, $P_\infty(a_\circ - a)$, which results in an opening displacement of [61]

$$\Delta = 8\frac{P_\infty a^3}{\bar{E}h^3} + 12\frac{P_\infty(a_\circ - a)a^2}{\bar{E}h^3} + \theta_\circ a + \delta_\circ. \tag{2.5}$$

The elastic modulus was determined by fitting the theoretical displacements along the entire range of experimentally measured crack-mouth opening displacements, with the best fit plotted in Figure 2.8a. The fitting was sensitive to within 2 GPa for the elastic modulus; however, the modulus was determined to be 217 ± 9 GPa when taking into account the experimental uncertainties. There exists good agreement between the experimental measurements and theory along the entire range of data. As a comparison, a tensile test was run with the

[7] As noted in Section 2.3.3, the elastic modulus is taken to be $\bar{E} = 217$ GPa.

[8] The root displacement is technically defined as the displacement separation between the centroidal axes at the crack-tip [61]. Here, the difference between the crack-tip opening displacement and the root displacement was negligible, and so $\delta_\circ$ was used for all calculations. This is consistent with the previous observation that the steel adherends were about two orders of magnitude stiffer than the adhesive layer.

same steel and it was determined to have an elastic modulus of 204 ± 8 GPa and Poisson's ratio of 0.32 ± 0.07. Therefore, these results suggest the bending modulus falls between the plane stress and plane strain assumptions.

Inscribed on Figure 2.8a is the opening displacement predicted for a perfectly-bonded, linear-elastic system. This is calculated from the linear-elastic DCB given in Ref. [61]:

$$\Delta = \frac{P_\infty}{\bar{E}} \left(8\frac{a^3}{h^3} + 12\frac{(a_\circ - a)a^2}{h^3} + 16.2\frac{a_\circ a}{h^2} + 5.44\frac{a_\circ + a}{h} + 3.66 \right). \tag{2.6}$$

As seen in Figure 2.7 with the root rotation calculation, the linear-elasticity solution fails to describe the measured displacements around point "A", which coincides with the point where the cohesive-length scale is too large for LEFM to be a realistic approximation of the experiment. As seen here, there would be significant error in determining the elastic modulus if one blindly assumed elastic compliance for this system.

More can still be done with the full-field measurement capabilities of DIC. At this point in the crack-mouth opening displacement analysis, only one point behind the crack-tip has been compared with the theoretical calulcations. In Figure 2.8b, the entire opening displacement (calculated from the centroidal axes of the top and bottom beams) behind the crack-tip is compared with theoretical calculations at load point "D". The theory involves an Euler-Bernoulli beam with the experimentally-measured root rotation and crack-tip displacement for the crack-tip boundary conditions. As in Figure 2.8a, it was assumed the combined shear load and bending moment acted $a = 28.3$ mm behind the crack-tip and the elastic modulus was 217 GPa. The good agreement seen here provides experimental support that one can describe the deformation of a DCB by Euler-Bernoulli beam theory if one includes the appropriate root rotation and displacement as the crack-tip boundary condition [61].

2.3.4 Cohesive-zone measurements

If one is just interested in extracting the mode-I traction-separation law, the crack-tip opening displacement is all that is required. However, as observed above, DIC's full-field measurement capabilities allow much more data to be generated. Instead of limiting the analysis to only crack-tip data, it is now time to consider deformation ahead of the crack-tip. Using the same method as described for the crack-tip opening displacements, 6 vertical lines of data, spaced approximately 4 mm apart, are highlighted in Figure 2.9a. The raw displacement data for these vertical lines, without correction for rigid-body rotation, are then plotted in Figure 2.9b for load point "D". Rigid-body rotation corrections were made for subsequent figures.

Data like those shown in Figure 2.9b were analyzed along the entire interface, which allows

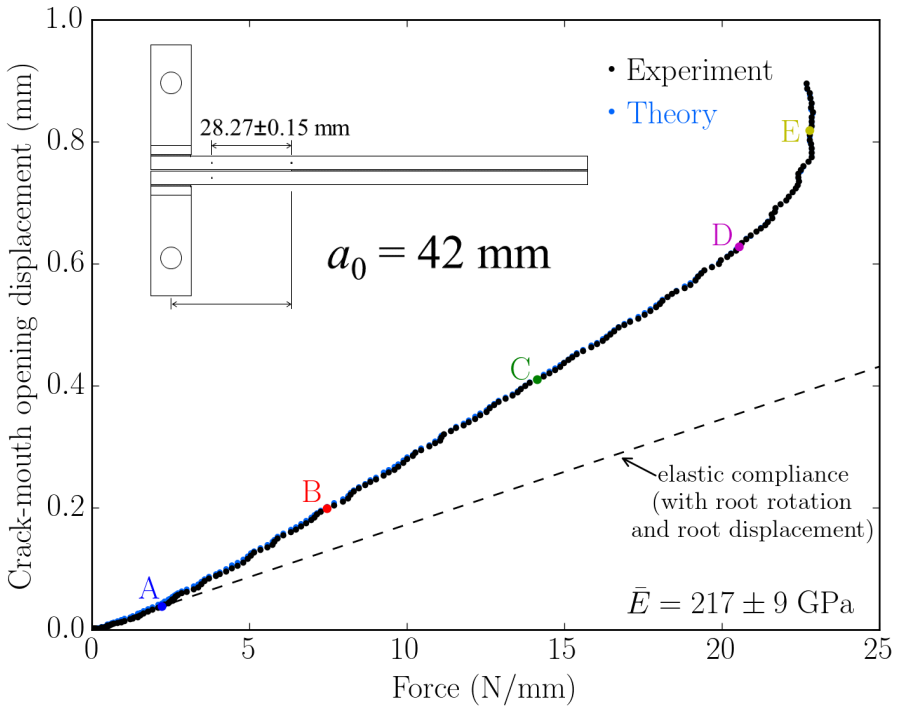

(a)

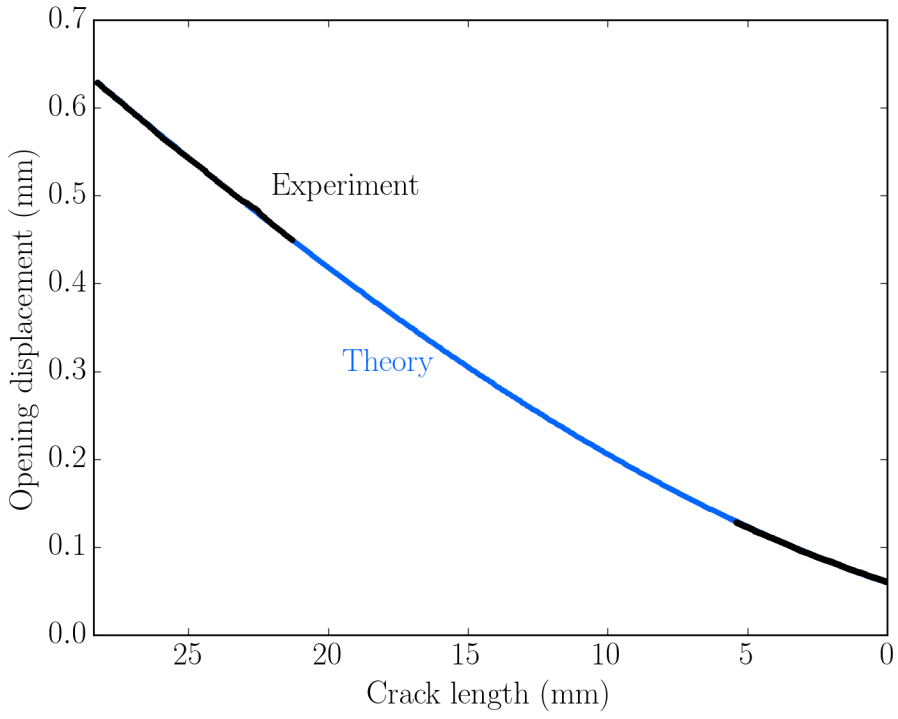

(b)

Figure 2.8: **(a)** The calculated and experimental opening displacements are compared, showing that the effective modulus is 217 ± 9 GPa. These calculations are done assuming an Euler beam acted upon by the appropriate load and moment calculated at a distance approximately 28 mm behind the crack tip, and assuming the root rotation given in Figure 2.7. **(b)** One sees this agreement is found not only at a single point, but rather in both fields of view provided by two separate cameras. The data is taken at load point "D".

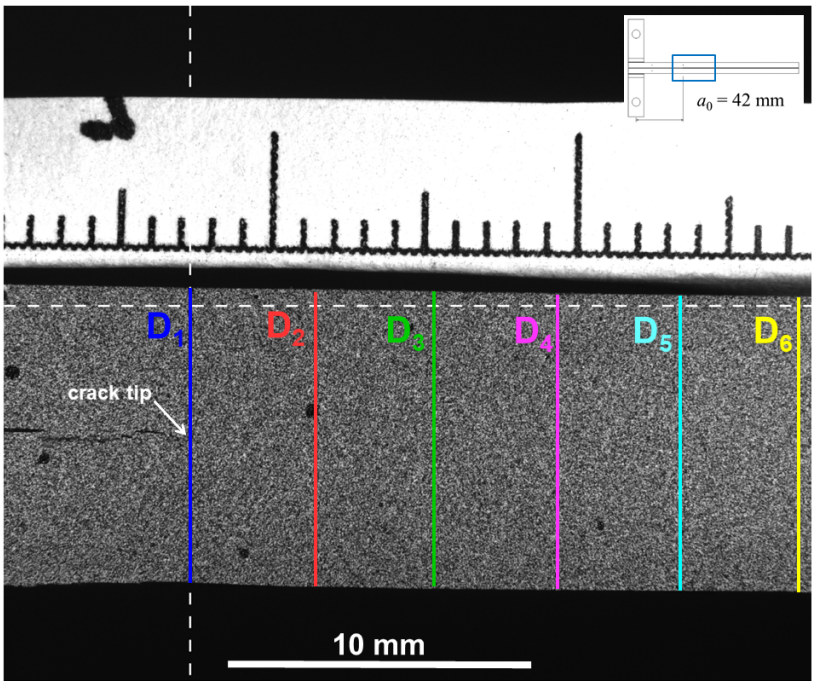

(a)

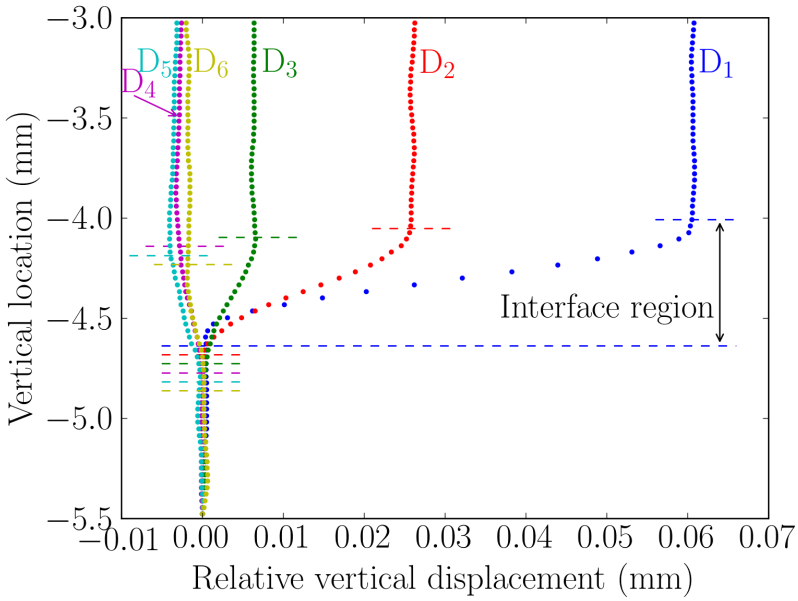

(b)

Figure 2.9: Determination of normal displacements ahead of the crack-tip. **(a)** Example lines along which normal displacements are measured as a function of vertical distance, along with the origin and crack-tip location. **(b)** The corresponding relative displacements for the six lines shown in (a). No rigid-body rotation corrections have been made for these data.

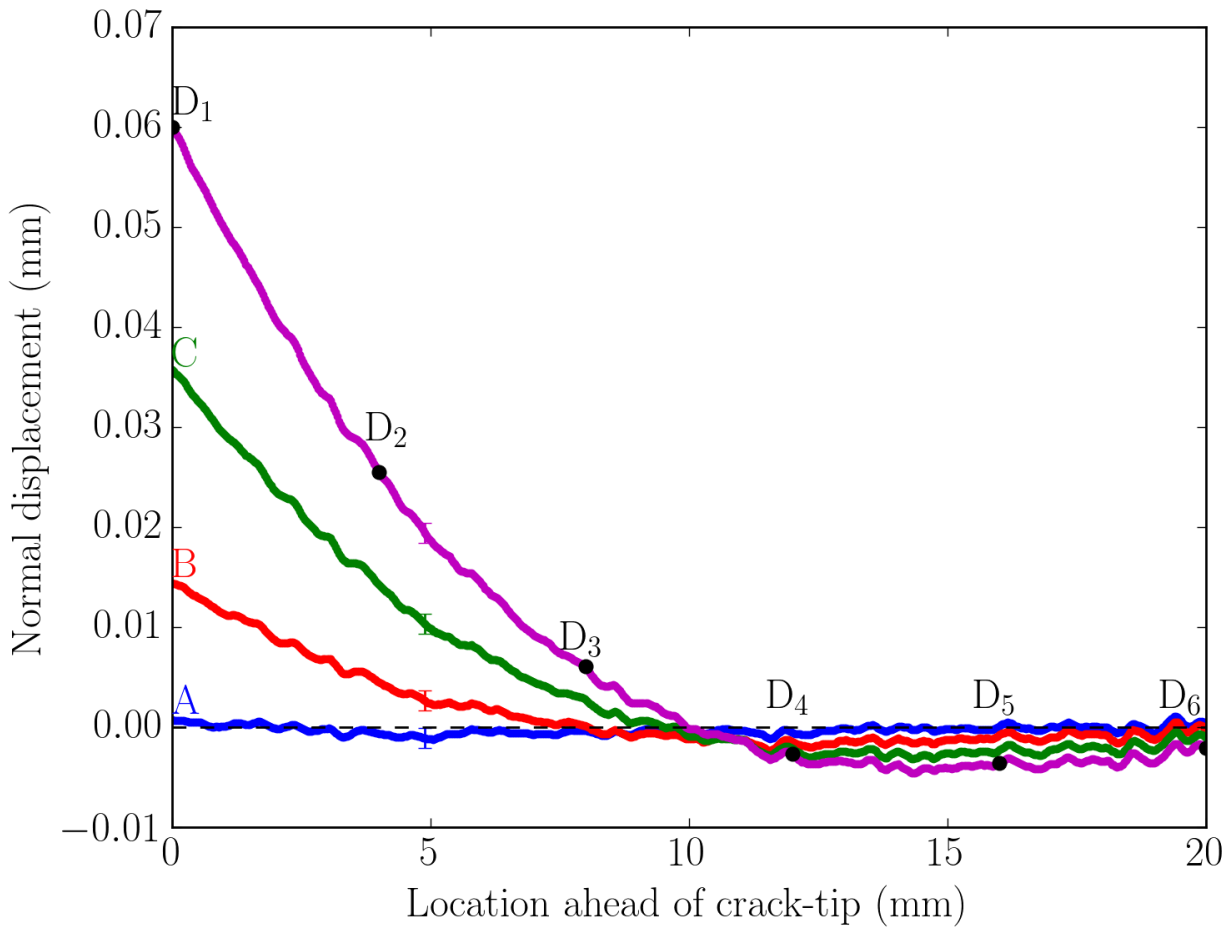

Figure 2.10: Plot of normal displacement ahead of the crack tip calculated in the same manner as Figure 2.4. The four lines correspond to loads A-D from Figure 2.3.

one to see the opening displacement profile ahead of the crack-tip, as plotted in Figure 2.10. As shown on the figure, the measurement uncertainty is approximately 1 micron, which means the opening displacement at point "A" is near the noise floor. In spite of this, one still sees the evolution of the cohesive-zone as the load increases.

Full-field measurement capabilities allows one to measure the length of the cohesive-zone, and measure it as a function of load. This is significant as it does not appear anyone else has done this before. It is worth noting, however, that one should be specific as to the definition of the measured length of the cohesive-zone, d, here defined as the point where the normal displacements first cross from tension to compression. This is necessary because of the large region of compression that may be ahead of the crack-tip.

In Figure 2.11, the normalized cohesive-zone length, d/h, is plotted against the (crack-tip) cohesive-length scale. This result can be found using the model of a beam on an elastic foundation [52, 61]. For a crack-tip loaded by a shear load, $V_\circ$ and bending moment $M_\circ$, the

tractions become compressive at a distance [80]

$$z_\circ = \frac{1}{\beta}\tan^{-1}\left(\frac{V_\circ h}{h\beta M_\circ}+1\right), \tag{2.7}$$

where $\beta = \sqrt[4]{6k/\bar{E}h^3}$, and k is the stiffness of the traction-separation law. For this geometry, $V_\circ = P_\infty$ and $M_\circ = P_\infty a_\circ$, giving

$$z_\circ = \frac{1}{\beta}\tan^{-1}\left(\frac{1}{8.75\,h\beta}+1\right). \tag{2.8}$$

Recalling that $\bar{\xi} = k\bar{E}/kh$ for a linear traction-separation law, one can rearrange the expressions such that $\bar{\xi} = 12/(\beta h)^4$, and gives the cohesive-zone length for this geometry as

$$\bar{z_\circ} = z_\circ/h = 0.537\bar{\xi_\circ}^{1/4}\tan^{-1}\left(1+0.0614\bar{\xi}_\circ^{1/4}\right). \tag{2.9}$$

This analytical expression for a linear traction-separation law (Equation (2.9)) is inscribed on Figure 2.11a.

The root rotation has been been re-plotted as a function of the cohesive-length scale in Figure 2.11b. For a DCB loaded via a shear load $V_\circ$ and bending moment $M_\circ$, the root rotation is given by [61]

$$\theta_\circ = 2*6^{1/2}\left(\frac{\bar{E}}{hk}\right)^{1/2}\frac{V_\circ}{\bar{E}h} + 4*6^{3/4}\left(\frac{\bar{E}}{hk}\right)^{1/4}\frac{M_\circ}{\bar{E}h^2}. \tag{2.10}$$

Since the root rotation corresponding to $k^* = 0.811\bar{E}/h$ is equal to the LEFM value, one can consider a spring constant, k, to arise from two springs in series in order to separate the linear elasticy and cohesive-law stiffnesses: k^* and k_b , where k_b is the stiffness of the cohesive-law. Then, it can be shown that the crack-tip cohesive-length scale is related to k by

$$\bar{\xi_\circ} = \frac{2\bar{E}}{k_b h} = \frac{2\bar{E}}{kh} - 2.466. \tag{2.11}$$

Therefore, for the DCB considered here has the root rotation given as

$$\frac{\bar{E}h\theta_\circ}{P_\infty} = 2*6^{1/2}(0.5\bar{\xi_\circ}+1.233)^{1/2} + 4*6^{3/4}(0.5*\bar{\xi_\circ}+1.233)^{1/4}\frac{a_\circ}{h}, \tag{2.12}$$

where (as before) the shear load is given by $V_\circ = P_\infty$ and bending moment by $M_\circ = P_\infty a_\circ$. This expression is inscribed on Figure 2.11b, noting that $a_\circ/h = 8.75$. The surprisingly good agreement between the results suggests the cohesive-length scale may be able to pro-

vide information concerning the adhesive layer's compliance and cohesive-zone development, independent of the precise shape of the traction-separation law.

2.3.5 Rotation and shear around the crack-tip

As has been done above, the full-field measurements of DIC allowed one to expand from measuring the crack-tip displacements to measuring the displacements of the entire cohesive-zone. Now, the root rotation will be expanded to consider those rotations around the crack-tip. Whereas the root rotation measurement of Figure 2.7 defined the rotation as relative difference of du/dy for the top and bottom beams, now the rotations are separated into average rotation and shear components. The average rotation for each beam (plotted in Figure 2.12a) is defined as $(dv/dx - du/dy)/2$ while the shear strain for each beam (plotted in Figure 2.12b) is defined as $(dv/dx + du/dy)/2$. These definitions are the same as above, where the y-axis is pointing away from the interface.

One notes that in Figure 2.12a, the average rotations decay to zero much more slowly than the normal displacements, which puts the adhesive layer in a state of in-plane tension. Taking the data at "D" as an example, beam rotation would cause the adhesive to extend about 12 microns over about 15 mm, which would correspond to an tensile strain of about 0.0008. This estimate is consistent with the strain measured within the adhesive layer via DIC and the FEM results presented below.

The average shear strain is much smaller than the average rotations, and the largest measured values are larger than the experimental uncertainty (as noted by the errorbar). While it may surprise the reader to see the shear strain increase as one moves ahead of the crack-tip, these results are consistent with FEM results computed for the numerical comparisons in Section 2.4, and in those calculations the average shear strains always returned to zero further ahead of the crack-tip (although outside of the experimental field of view).

2.4 Numerical comparison

Full-field measurement techniques have previously been used to extract traction-separation laws, whether via a direct method [71] or an inverse method [72, 74]. However, what sets this work apart from others is that the traction-separation law (using a direct approach) has been measured independently from the cohesive-zone's opening profile using DIC. One can now compare the experimental measurements and see if they can be replicated numerically using the extracted traction-separation law.

Numerical calculations were performed using the commerical software Abaqus 6.14 [1]. The cohesive-zone model was implemented through the use of a user-defined element that can

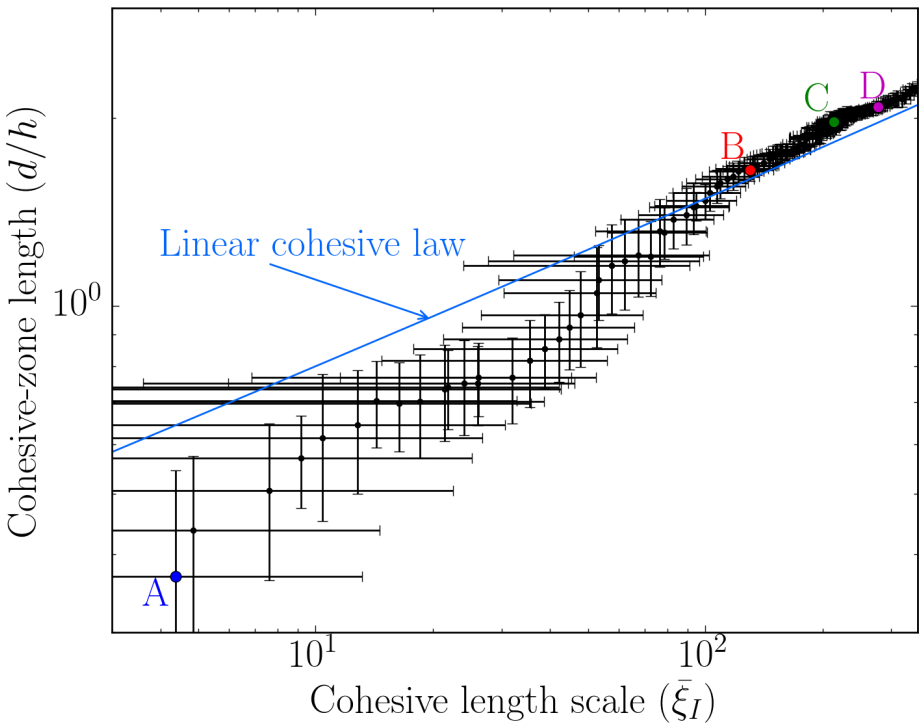

(a)

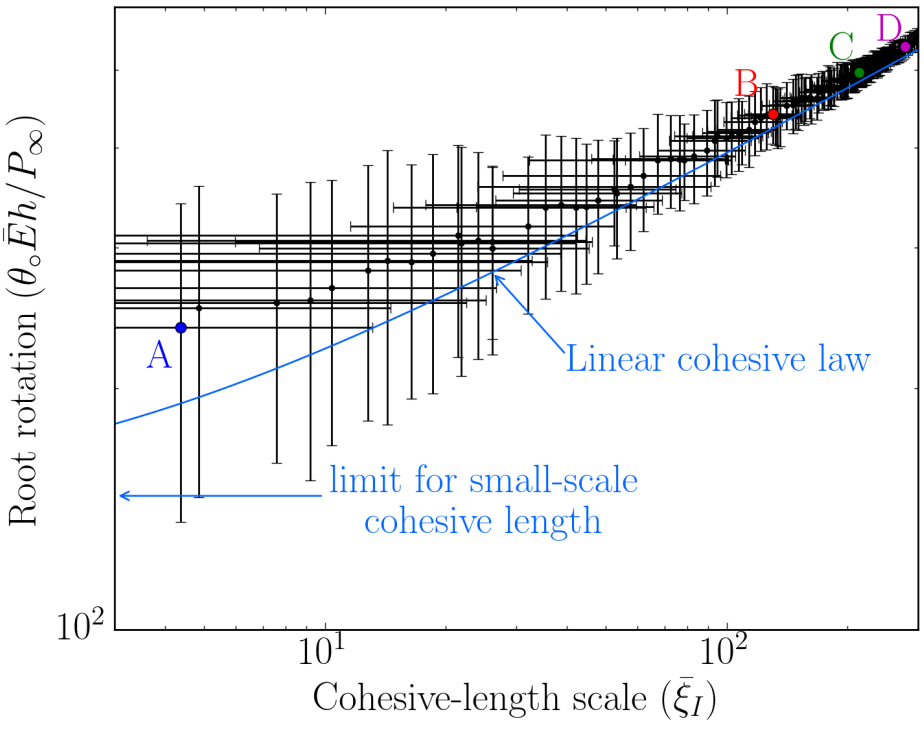

(b)

Figure 2.11: **(a)** A comparison between the "length" of the cohesive zone, defined as the distance from the cohesive-crack tip to the point at which the stresses become compressive, and the cohesive-length scale. **(b)** A plot of how the root rotation varies with cohesive-length scale. Inscribed on these plots are comparisons to the results for a linear cohesive law.

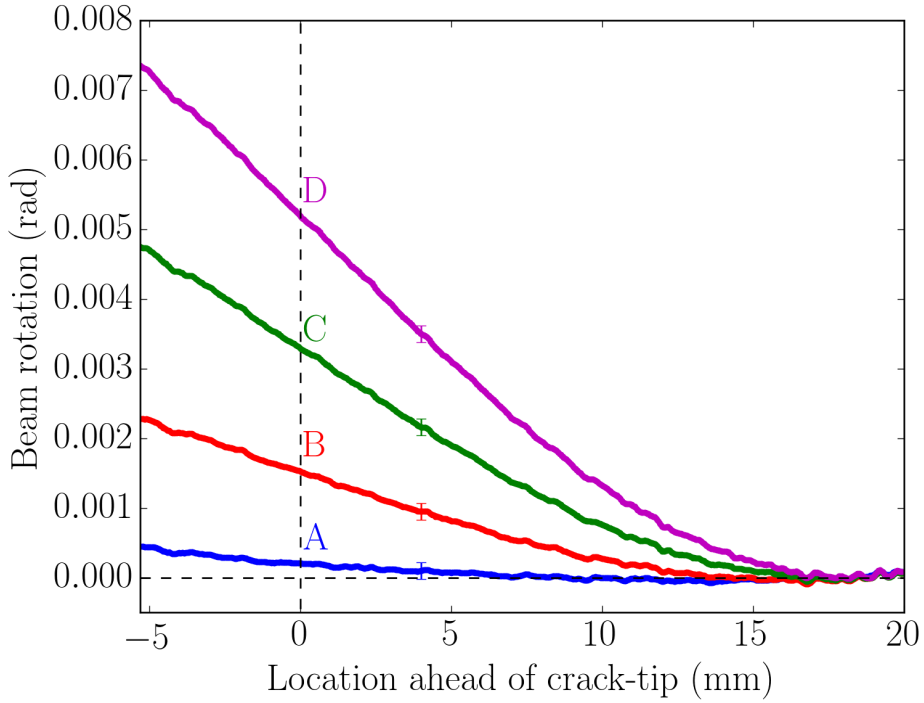

(a)

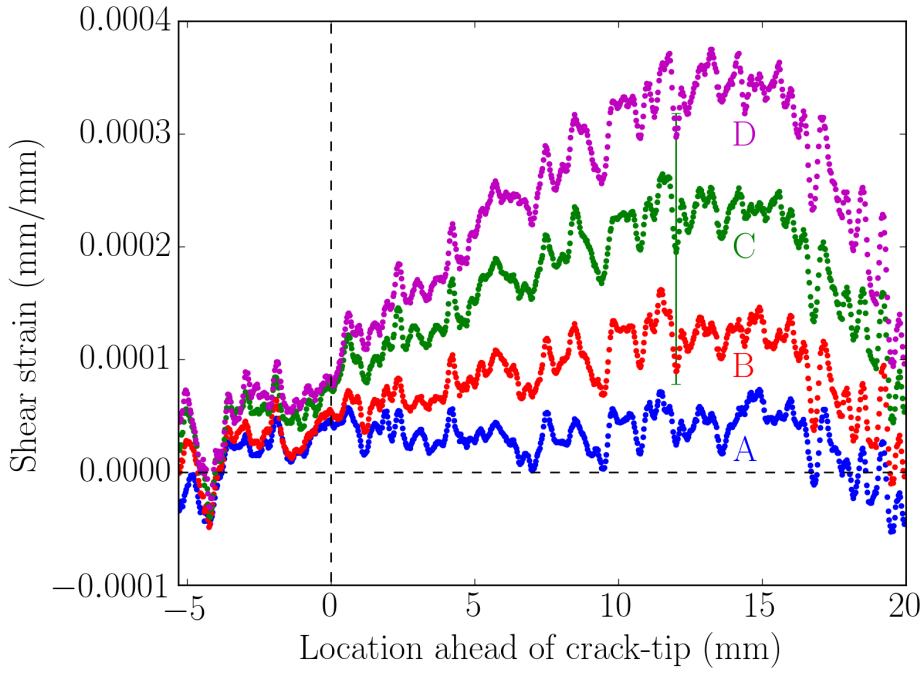

(b)

Figure 2.12: Plots of **(a)** average rotation, $(dv/dx - du/dy)/2$, and **(b)** shear strain, $(dv/dx + du/dy)/2$, around the crack tip for each beam.

be found in Appendix A. The adherend's elastic modulus was set to 217 GPa, in accordance with the findings of Section 2.3.3 for the steel beams' deflections. The initial slope of the mode-I traction-separation law was approximately the elastic compliance of a 275 micron thick adhesive layer with a quoted elastic modulus of 870 MPa [77]. The "yield" for the traction-separation law occurred around 4 MPa at a little more than 1 micron; these values correspond to the lowest measure normal stress in Figure 2.6 and the experimental noise floor.

The importance of the compressive portion of the traction-separation law was not obvious until after the experiments were complete. Ref. [26] showed that the cohesive-zone model with a finite-thickness interface could accommodate compression ahead of the crack-tip. As one sees in Figure 2.10, there is a significant portion of the normal displacement profile that is in compression.

As experimental testing was complete, the numerical experiments were run where the compressive stiffness was varied in the finite-element calculations. It was found that all of the normal displacement data (that is, both opening displacements and closing displacements) could not be replicated unless the appropriate compressive law was included. It was determined the appropriate compressive law was anti-symmetric with respect to the tensile law (with "yield" at -4 MPa). This "yield" in the compressive portion was required to obtain good agreement with the experimental results, for a purely elastic compressive law was not the best fit.

Having determined the shape of the compressive portion of the traction-separation law, Figure 2.13a compares the experimental results with the findings from CZM. As one can see, the agreement is rather good along the entire view. However, when comparing the CZM and experimental results, one notices CZM tends to consistently overpredict the opening displacements. Recall from before that the beam bending places the adhesive into a state of in-plane tension. The cohesive-zone model works by replacing the opening and shear by springs; it is not a continuum and therefore no in-plane tension can build up due to the bending adherends. A subsequent finite-element calculation was run by converting the traction-separation law into a uniaxial-tension stress-strain relation (assuming J_2-flow theory), and implementing this relation into the adhesive layer with the aforemtioned elastic modulus of 870 MPa and a thickness of 275 microns. These findings can be found in Figure 2.13b, and one notes even better agreement with the experimental results. This suggests the small discrepancy in the CZM calculation is from neglecting the build-up of an in-plane tensile stress (estimated to be ~ 0.5 MPa from the strain value quoted above).

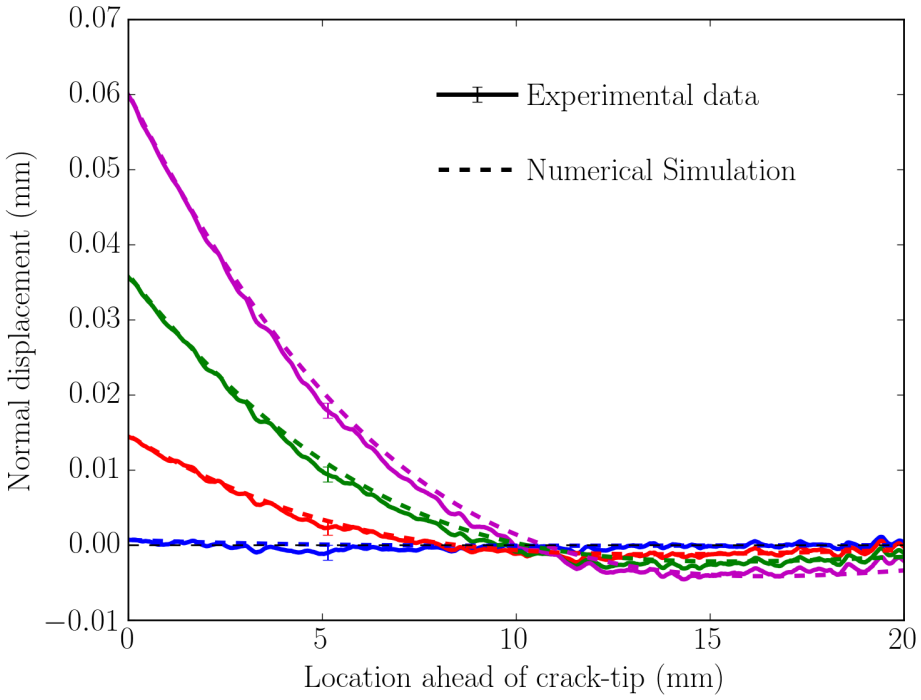

(a)

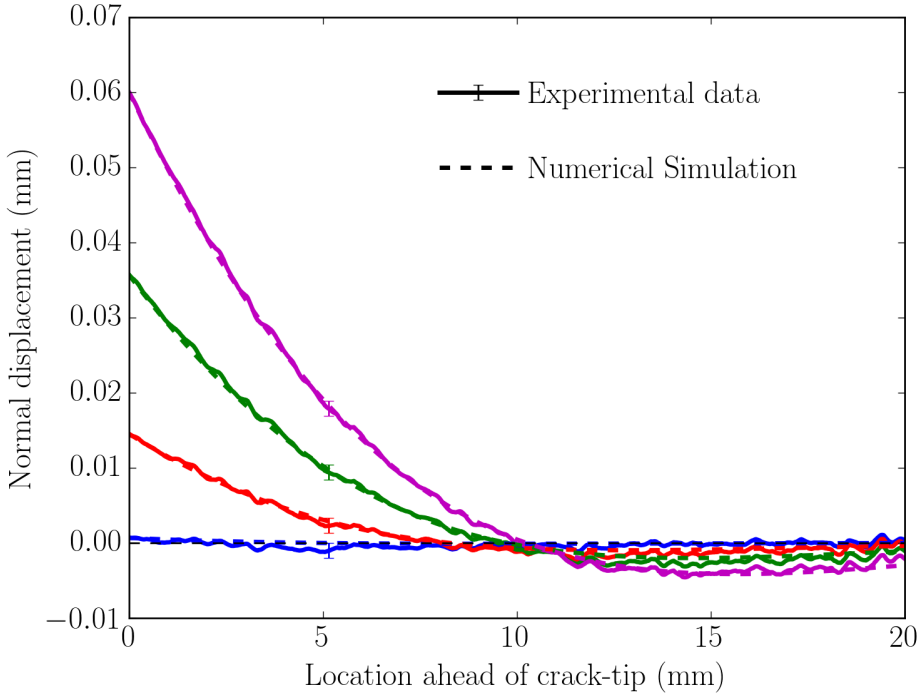

(b)

Figure 2.13: Comparison between the experimentally-measured normal displacements with numerical predictions based on **(a)** a cohesive-zone model where the compressive tractions are of equal magnitudes to the corresponding tensile tractions, and **(b)** a continuum model of the adhesive, assuming J_2-flow theory and a constitutive law based on the traction-separation law used for (a). One notices a slightly better agreement for the continuum model.

2.5 Summary

Digitial image correlation is a powerful tool that has steadily grown in popularity over the last couple decades, and it is becoming commonplace in mechanical testing labs. When analyzing beam-like geometries, it was found that measurement noise was reduced when vertical lines of displacement data were fit to linear functions before differentiation. This was the method used to extract the J-integral by analyzing the displacement data at the load points.

DIC's full-field measurement capabilities allowed one to measure rotations, shear strain, beam deflections, and the opening profile in the cohesive-zone. The fact that the cohesive-length scale could be measured during loading allowed one to see how the cohesive-zone and root rotation evolved. The smallest observable measurements of the root rotation and crack-mouth opening displacement agreed with LEFM predictions, and the experimental results diverged once the cohesive-length scale was too large for LEFM to be applicable.

As noted throughout this chapter, other groups have performed similar work and extracted traction-separation laws. This work is set apart from others because it separately measured the traction-separation law and then compared the numerical predictions with the measured cohesive-zone to find good agreement (with a small error due to neglecting the in-plane tensile stress from CZM). It was found that the compressive portion of the traction-separation law was important for matching both the tensile and compressive portions of the normal displacements ahead of the crack-tip. Finally, a straightforward method (perhaps upon which a new standard could be based off of) is provided for the extraction of the mode-I traction-separation law.

CHAPTER 3

On Varying Fillet Angles and Cohesive-Length Scales

3.1 Overview

From the results of Suo and Hutchinson [24], the energy-release rates of beam-like geometries were calculated for general combinations of axial loads and bending moments. The single lap-shear joint is one geometry to which this analysis could be applied [20], and many theoretical analyses [81, 82, 83, 84, 85, 86, 87] have been done on the geometry to show the stress variation across the bonded interface. In spite of this known stress variation, standards [88, 89] have been written to use the single lap-shear joint to (qualitatively) compare shear strengths of adhesives. If one is only considering the average shear stress, then the geometry ought to be used only for qualitative comparisons because it has been shown [20] the measured shear strength of the bonded ligament is a function of joint geometry.

Fernlund *et. al.* [90] tested some single lap-shear joints with and without cracks, and determined there was no significant difference between the results. The lap-shear standards [88, 89] also make no mention of the necessity of placing a sharp crack in specimens when comparing average shear strengths. These observations cause one to wonder if a crack is necessary. Indeed, this is one benefit of the cohesive-zone model, which has demonstrated [3, 20, 91] a sharp crack is not necessary to predict crack growth. While Mohammed and Liechti [91] looked at the effect of fillet angle[1] for a bi-material interface, the geometry considered was loaded under four-point bending. The work presented below is distinct and does not look to demonstrate the ability of CZM to predict crack-propagation at non-crack singularities.

The following chapter shows when the strict requirement for a sharp crack may be neglected, and when it must be present. This will be accomplished by analyzing a single lap-shear joint and varying the fillet angle (from a crack at 180°, through a corner at 90°,

[1] It should be noted that Ref. [91] uses a different definition for the fillet angle than the one used here.

and to even shallower singularities) and the cohesive-length scale. By using such a wide range of fillet angles, this will give a more general theoretical explanation to the aforementioned experimental observations and show that the corner singularity is not unique. These calculations show that at small cohesive-length scales (when LEFM is expected to be valid) the fine aspects of the singularity are important and determine the deformations of the cohesive-zone ahead of the crack-tip. However, at large cohesive-length scales the deformation ahead of the singularity looks the same regardless of the shape of the singularity. The author suggests this is a result of the large cohesive-length overshadowing the singularity, and making different singularities appear the same.

3.2 Analytical foundations

From elasticity [5], the energy-release rate G is defined as

$$G = -\frac{d\Pi}{da}, \tag{3.1}$$

where Π is the energy available for crack growth, and a is the crack-length (assuming a planar problem). Crack propagation occurs when $G \geq \Gamma$, where Γ is the material's toughness, or resistance to fracture. From the very definition of G, elasticity suggests one must always have a sharp crack. However, from experience one knows this need not the case from a macroscopic perspective, and this is not necessarily the case even in laboratory testing. This is one reason the cohesive-zone model has become such a common tool in studying fracture mechanics: it is well-known that failure does not always initiate at a crack, and CZM allows one to work around LEFM's limitations.

The single lap-shear joint with a crack is a special case of a wedge with an angle $\alpha = 180°$, as defined in Figure 3.1. For the isotropic lap-shear joint with a crack (Figure 3.2 with $\alpha = 180°$), the energy-release rate (*i.e.* work done at the crack-tip) has an analytical solution when loaded via axial loads and bending moments [20]:

$$G = \frac{P^2}{2\bar{E}h} + \frac{6M^2}{\bar{E}h} - \left(\frac{P^2}{4\bar{E}h} - \frac{12(M - 0.5Ph)^2}{16\bar{E}h^3}\right), \tag{3.2}$$

where P and M are defined are the reactionary axial load and bending moment in response to a horizontal displacement u, as shown in Figure 3.2.

An additional finding from Ref. [20] was that there were two limits for the (normalized) energy-release rate of the single lap-shear joint: a low load (undeformed) limit of 1.75 and a large load (deformed) limit of 0.25. In Figure 3.3, a similar energy-release rate vs. load

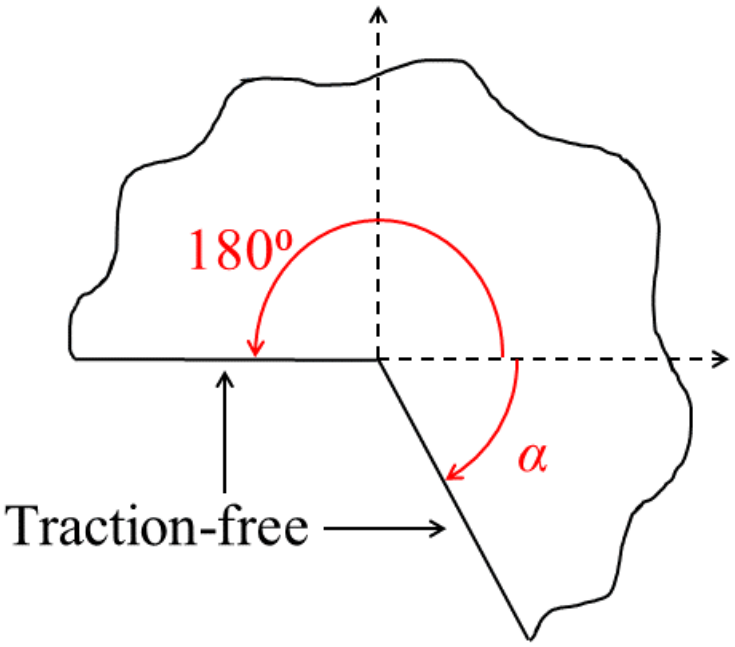

Figure 3.1: A wedge problem is typically defined by the half-angle of the wedge and rotation from the horizontal. However, here the single lap-shear joint is the only geometry considered, and therefore the top half of the wedge is required to be 180° while the fillet angle α is allowed to vary.

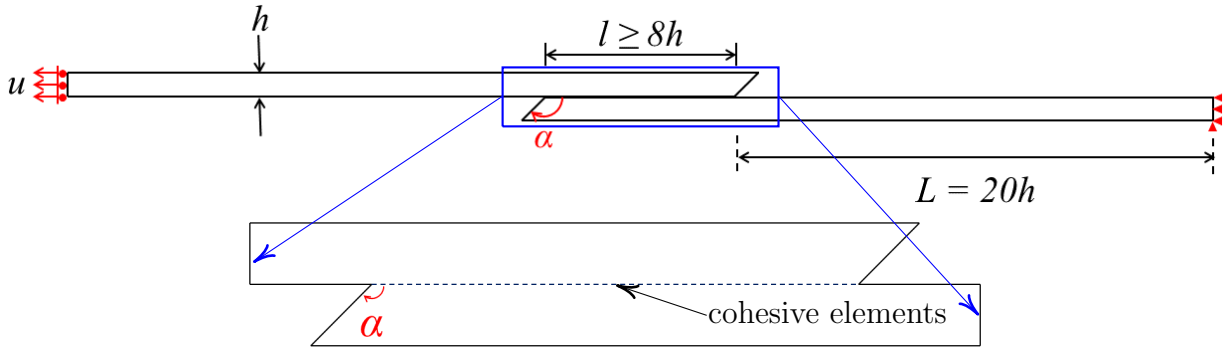

Figure 3.2: For all calculations, identical boundary conditions were used for all lap-shear geometries. The only difference between calculations is the fillet angle. Because the ligament length l may change the value of the J-integral, all comparisons are made to the (elastic) crack-tip calculation for a given load P (with a compensating moment M). The ligament length l was typically chosen to be either $8h$ or approximately 20 times the cohesive-length ξ, whichever was longer, to ensure the geometry was long enough so that any displacements across the interface were negligible. In all CZM calcuations performed here, the lap-shear interface had a single line of cohesive elements along the entire length of the ligament, with the beams being much thicker than the cohesive elements. The singularity work values were taken as the sum of the mode-I/-II work determined from the closest element to the singularity, as determined from the boundary conditions and choice of traction-separation law(s). The arm length is held constant at $L/h = 20$ for all calculations.

plot is reproduced for elastic lap-shear joints of four different ligament lengths. For these (and all subsequent) elastic calculations, the finite element software Abaqus 6.14 [1] was used, with the J-integral calculated via the software's internal capabilities. One observes that the short ligament (*e.g.* $l/h = 8$) geometries require a much larger load to reach the deformed-geometry limit compared to the long ligament (*e.g.* $l/h = 640$) geometries. This is a useful result if one wants an estimate of the energy-release rate and has only limited information of an elastic lap-shear joint.

The cohesive-zone model was implemented using the user-defined element (UEL) found in Appendix A implemented in Abaqus 6.14 [1] for all calculations. Since CZM is being used, the entire lap-shear ligament (interface) was made of cohesive elements and the locations specified in the close-up of Figure 3.2. Linear traction-separation laws are typically used to ensure a constant cohesive-length scale in mode-I and mode-II throughout loading. Displacement boundary conditions were specified, and the resulting interfacial displacements followed from the numerical calculation as the solution to the boundary-value problem. For a given singularity, the singularity work $W_\circ$ is defined as the sum of W_I and W_{II} at the edge of the fillet angle. The term "crack-tip work" will only be used when $\alpha = 180°$.

From a practical perspective, it is numerically impossible to calculate the work done at the crack-tip for a geometry with an infinite crack. Therefore, single lap-shear joints calculations were run with longer and longer cracks until the crack-tip work began to asymptote. Figure 3.4 compares the crack-tip work using CZM (where $\bar{\xi} = 0.0114$[2]) with a separate, elastic J-integral calculation for a long crack of $a/h = 16$ to give $J_\circ$. As the reader can see, the normalized crack-tip work begins to approach the J-integral value around $a/h = 1$. Exploratory calculations outside the load range listed gave similar results to those shown in Figure 3.4. Therefore, it was assumed that a crack length of $a/h = 2$ was a sufficient approximation for an infinite crack for the numerical experiments in the following section. A similar set of calculations were performed for the elastic J-integral calculations, and it was determined an elastic crack length of $a/h = 2$ was also a sufficient approximation to an infinite crack. In all current and subsequent CZM calculations, it was verified that cohesive-zone displacements were negligible along the entire length of the interface.

[2]Provided the cohesive-length scale was small enough such that LEFM was expected to be valid, choosing a different $\bar{\xi}$ did not change the trend found in Figure 3.4.

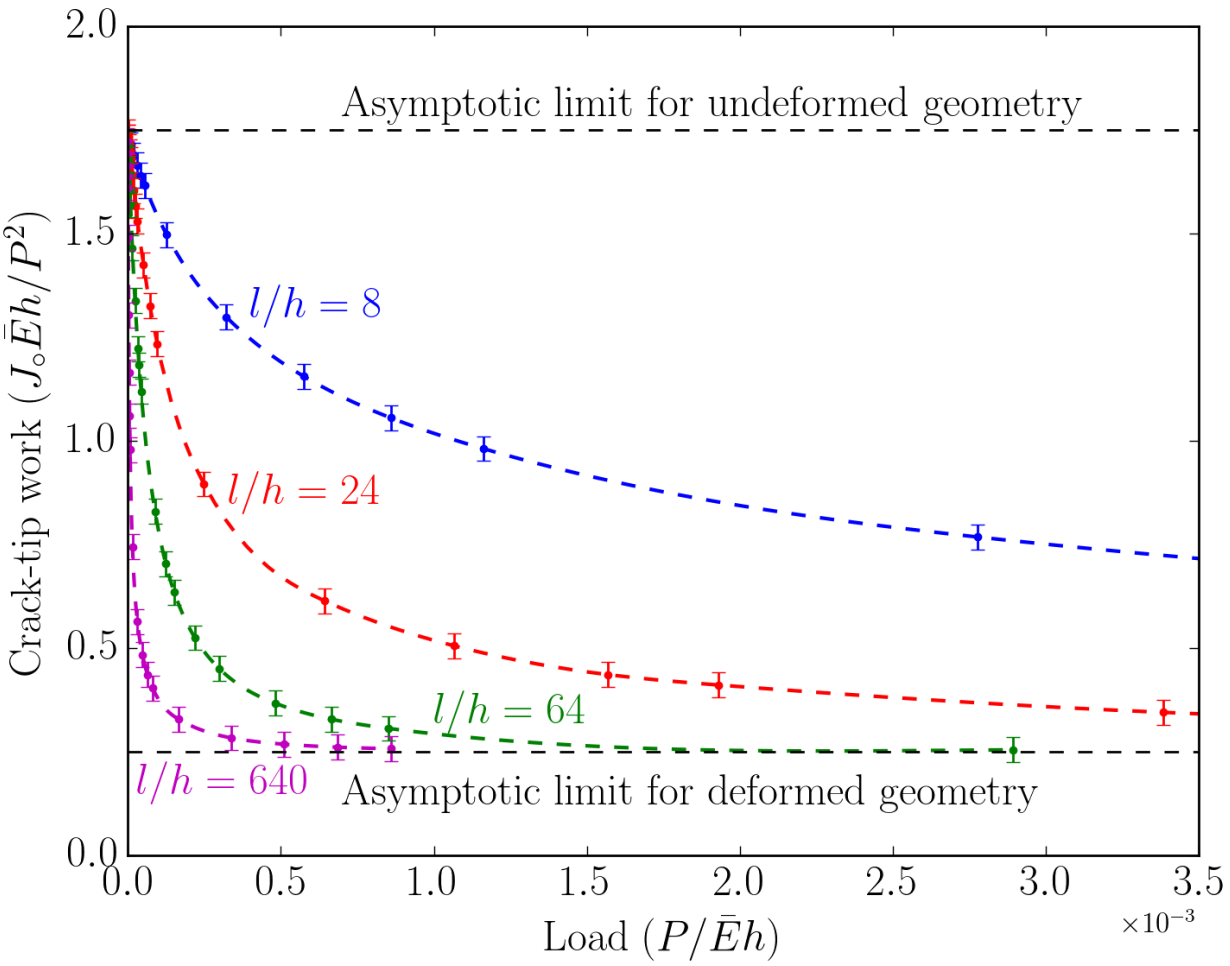

Figure 3.3: Normalized energy-release rate (calculated using the J-integral) for four elastic lap-shear joints with different ligament lengths at varying loads. The results presented here reproduce the trend observed in Ref. [20] where there exist two asymptotic limits for the energy-release rate. The additional calculations show that these two limits may be separated by a relatively large load, depending on the length of the ligament. A crack length of $a/h = 2$ and arm length of $L/h = 20$ were used for these calculations.

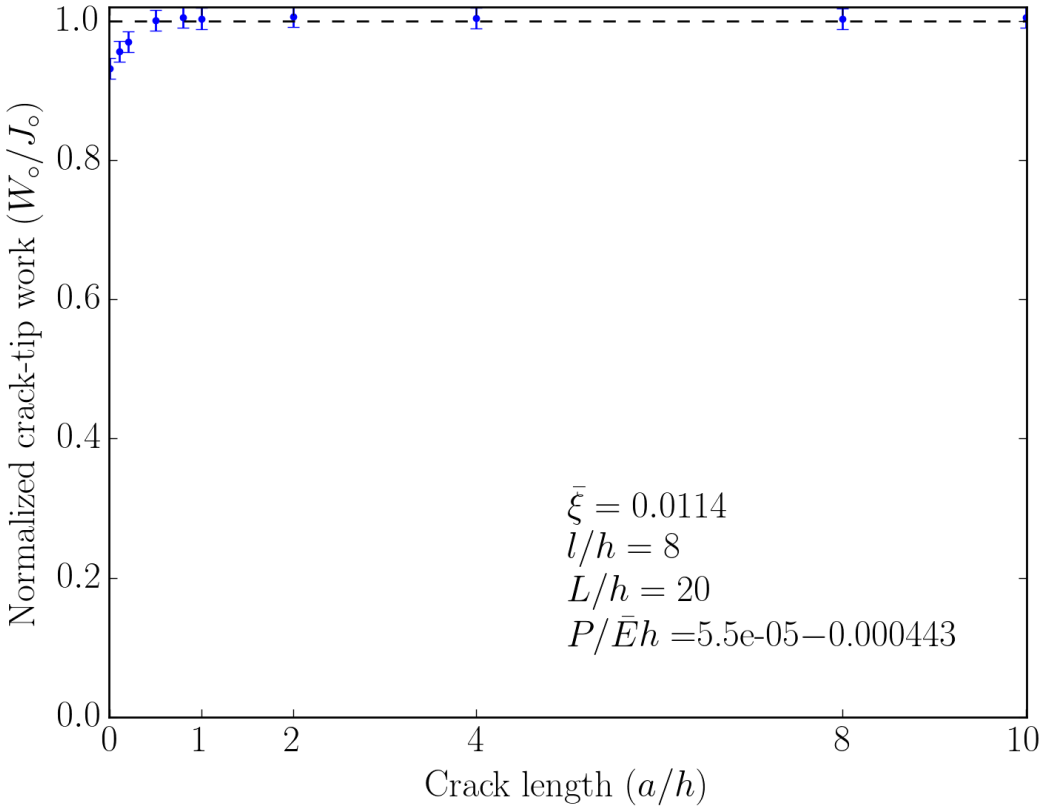

Figure 3.4: CZM crack-tip work $W_\circ$ compared to a long elastic crack ($a/h = 16$) J-integral calculation. To ensure a long enough crack was used for subsequent calculations, elastic FEM calculations with a sharp crack were run with increasing crack length until an asymptote was reached. These results were then compared to similar calculations using crack lengths at a small cohesive-length scale (here, $\bar{\xi} = 0.0114$), and it was found that around $a/h \sim 1$ the crack-tip work started to plateau. Exploratory calculations were run outside the range listed, which gave results similar to those above. Therefore, it was assumed that a crack-length of $a/h = 2$ would be an adequate approximation of an infinite crack at all loads. The crack-lengths of the elastic calculations were varied in a similar manner, and it was found $a/h = 2$ was a sufficient approximation for an infinite crack as well.

3.3 Numerical experiments

3.3.1 Work done at the singularity

For the numerical experiments, the beam thickness was kept much larger than the CZM interface ($h/t_{cz} = 25000$[3] at the smallest CLS values and $h/t_{cz} = 1000$ at the largest values). In the interest of computational efficiency, the mesh density was gradually decreased as one moved away from the singularity. The loads were applied via a uniform horizontal displacement at the left-hand side of the top beam, although the left edge was allowed to move vertically to ensure a shear load was not applied. It was verified that any applied shear load that might be required for numerical stability was negligible. Each separate calculation was compared back to an elastic lap-shear calculations with a crack (with $a/h = 2$), which allows one to compare the effect of varying fillet angles to a separate, fully-elastic J-integral calculation. The ligaments were kept long enough (usually $l/h = 8$ or $l/\xi = 20$, whichever was larger) to ensure the only geometric effects considered during these calculations were from changes in the fillet angle.

As shown in previous work [27, 92], different mesh densities may be required for observing different crack-propagation phenomena. Ref. [27] demonstrated LEFM phase angles could be reproduced when the mesh density was approximately 1% of the cohesive-length for a crack, and this result was reproduced here. However, this estimate only holds true for a crack, and other fillet angles considered here required mesh densities of $\xi/t_{cz} \sim 1000$ or even $\xi/t_{cz} \sim 10000$ before a phase angle plateau was observed. It was observed in mesh-sensitivity calculations that the coarser-mesh results always converged to the results presented here, regardless of whether or not a plateau was present.

It is worth noting the mesh sensitivity required for a phase angle plateau is independent of that for the work done at the singularity. At the smallest cohesive-length scales, the work values did not plateau to a constant value as one approached the singularity[4]. However, by running multiple calculations at varying mesh densities, one noted that the singularity work values began to plateau for a fine enough mesh. The mesh density at which the singularity work plateaued was determined to be $\xi/t_{cz} \sim 300$, regardless of fillet angle. Therefore, this mesh density set the mesh size at the smallest cohesive-length considered here.

Dimensional arguments may be used to show the singularity work is a general function

$$\frac{W_\circ}{J_\circ} = d\left(\frac{l}{h}, \frac{L}{h}, \frac{P}{\bar{E}h}, \alpha, \bar{\xi}\right), \tag{3.3}$$

[3] t_{cz} is the width of the smallest cohesive element at the singularity.

[4] Numerical limitations restricted the mesh density to $\xi/t_{cz} \sim 300$ for the smallest cohesive-length scale. This may explain why no plateau was found for the singularity work at the smallest cohesive-length scales.

where all geometry parameters have been defined in Figure 3.2. The load P is the reactionary force resulting from a horizontal displacement u and $\bar{E}$ is the elastic modulus of the beams. The variation of Equation (3.3) with respect to the load will be the first aspect considered. In Figure 3.5, two different geometries at two different cohesive-length scales are considered at three different loads: low, mid-range, and high. The low and high loads are to consider the singularity work near the asymptotic limits of crack-tip work, and the mid-range value is somewhere in between. It is also clear from Figure 3.5 that Equation (3.3) is (in general) a non-linear function of the fillet angle. The CZM crack-tip work vs. load curves for $l/h = 24$ and $l/h = 640$ are nearly identical to those found in Figure 3.3, and therefore they are not plotted here.

Systems with small cohesive-length scales will now be considered, where LEFM is expected to be a useful approximation. Figure 3.6a gives the crack-tip work vs. load range for three different lap-shear joint calculations. One notices the work-load curves are similar to those from the elastic calculations in Figure 3.3. One also observes in Figure 3.6b that an increase in cohesive-length scale results in a general increase in the singularity work function (this will become more obvious at larger cohesive-length scales). Even though the cohesive-length scale is small enough one would expect LEFM to be a useful approximation, it appears as though there is still some geometry dependence in the singularity work.

One notices a distinct drop in the singularity work as the fillet angles get smaller and smaller for these small cohesive-length scale results. Although there exists geometry dependence, consider the calculations for $\bar{\xi} = 0.114$. If one only measured the singularity work (with no other information), one might be able to explain away the small discrepancy from the J-integral as manufacturing variation and might cause one to suspect there is something special about the corner singularity. However, when one fits the data from all the fillet angles (whether that be through cubic splines or polynomial fits), one notices there is a systematic shift in Equation (3.3) for all the fillet angles, and not just the 90° fillet angle (corner). Therefore, there does not appear to be anything special about the corner singularity.

If one were to take the limit of $\bar{\xi} \to 0$, one could imagine where only the 180° fillet angle would have a singularity work value of unity and $W_\circ/J_\circ$ would drop to zero for all non-crack fillet angles. This would agree with the energy-release rate definition in Equation (3.1), where a sharp crack must be present for the definition to make sense. As for the significance of the local maximum and minimum observed in the singularity work at small cohesive-length scales, that explanation is left as an exercise to the reader.

At larger cohesive-length scales, similar geometry dependence may be observed for Equation (3.3). Figure 3.7a gives the normalized crack-tip work vs. load curves for two different ligament lengths: $l/h = 24$ and $l/h = 640$. As with the small cohesive-length scale results,

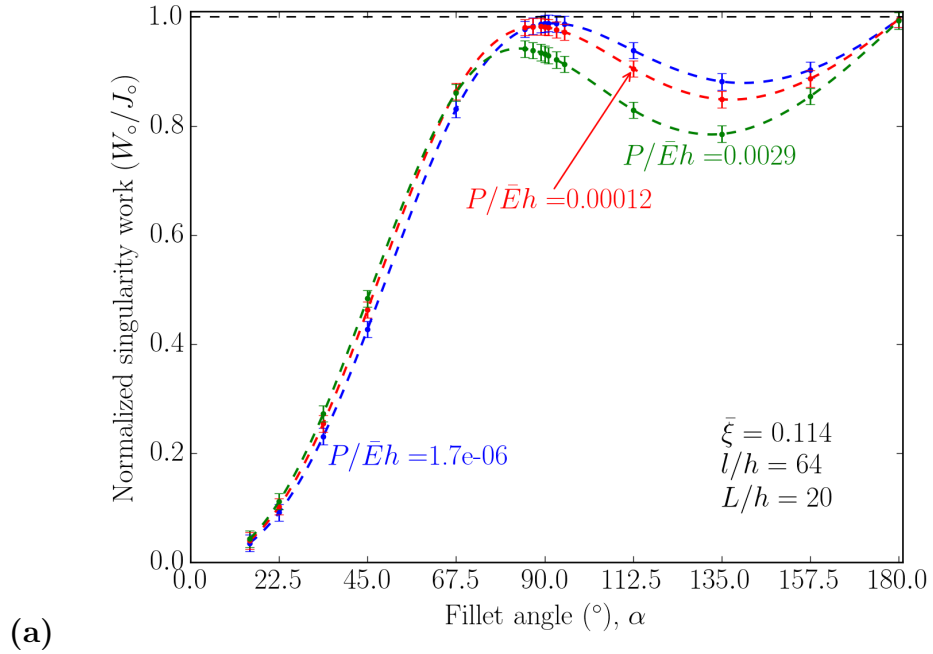

(a)

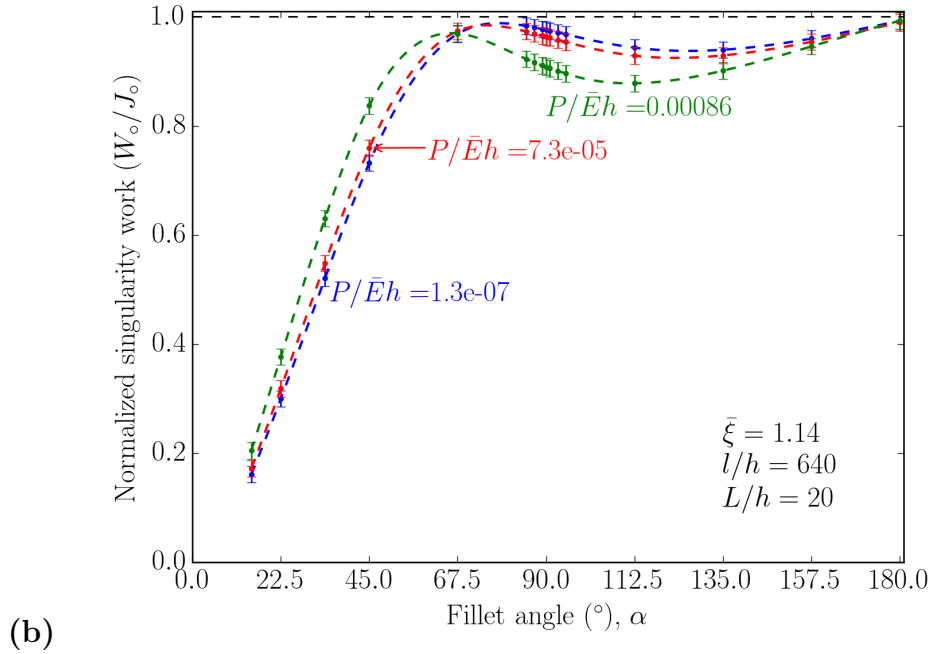

(b)

Figure 3.5: Normalized singularity work for **(a)** $\bar{\xi} = 0.114$ with $l/h = 64$ and $L/h = 20$ and **(b)** $\bar{\xi} = 1.14$ with $l/h = 640$ and $L/h = 20$ at three different loads. The CZM results produce crack-tip work vs. load curves nearly identical to those found in Figure 3.3, and therefore they are not reproduced here. In the results above, one sees how the singularity work varies for low, mid-range, and high loads. As one can see, the load variation is not the same for different geometries/cohesive-length scales. These results reinforce the dependence of Equation (3.3) on the load, $P/\bar{E}h$. It was verified that interface displacements were negligle along the entire length of the ligament.

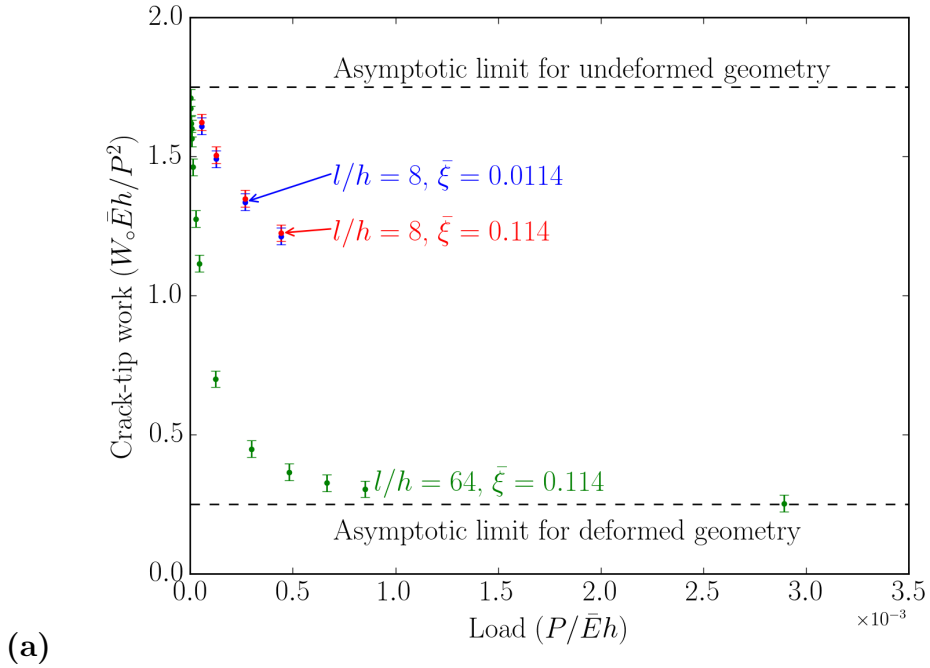

(a)

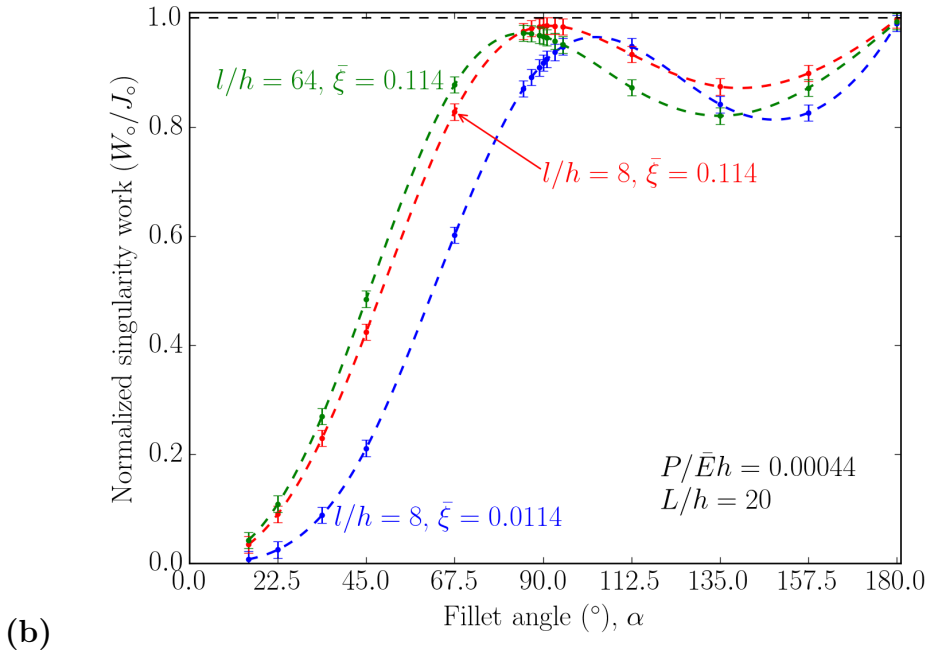

(b)

Figure 3.6: **(a)** The crack-tip work for small cohesive-length scales: $\bar{\xi} = 0.0114$ and $\bar{\xi} = 0.114$. For $\bar{\xi} = 0.114$, two ligament lengths are considered: $l/h = 8$ and $l/h = 64$. As one can see in comparison to the elastic calculations in Figure 3.3, the CZM crack-tip work results fall in line with the elastic results. As before, a crack length of $a/h = 2$ and arm length of $L/h = 20$ were used for these calculations. **(b)** The normalized singularity work at $P/\bar{E}h = 0.00044$ for those results plotted in (a). The results from $l/h = 64$ with $\bar{\xi} = 0.114$ were interpolated from the closest data points. When comparing the singularity work functions between cohesive-length scales, it is observed there is a systematic increase in $W_\circ/J_\circ$. For the same cohesive-length scale, one observes there is a small, but noticeable, difference in the singularity work functions for two different ligament lengths.

the work-load curves are similar to the elastic calculations found in Figure 3.3. In Figure 3.7b, one sees how the normalized work changes as a function of fillet angle for $\bar{\xi} = 1.14$. One sees significant difference in the two curves for $l/h = 24$ and $l/h = 640$.

Still larger cohesive-length scales may also be tested, although one must continue to increase the ligament length to ensure negligible displacements across the interface. Figure 3.8a gives the crack-tip work vs. load plots for the large cohesive-length scale calculations. As the reader can see, all three geometries are approaching the deformed geometry limit at load $P/\bar{E}h = 0.001$. The singularity-work for these larger cohesive-length scales are plotted in Figure 3.8b for this load. Here, one continues to see the general trend of Equation (3.3) increasing towards unity for all fillet angles for large cohesive-length scales. From the results from Figures 3.6, 3.7, and 3.8, one expects $W_\circ/J_\circ \to 1$ as $\bar{\xi} \to \infty$ for all fillet angles.

3.3.2 Mode-mixity at varying fillet angles

A fundamental aspect of LEFM is the singular stress (and displacement) field as one approaches a crack-tip. Specifically, the singular field of $r^{-1/2}$ is expected for a crack, and the cohesive-zone model matches part of this field at small enough cohesive-length scales regardless of the shape of the traction-separation law [26, 27, 28]. Elastic stress fields for a generic wedge [93] may be used to generalize the singular field, of the form

$$\frac{\sigma_{ij}}{\bar{E}} = f_{ij}\left(\frac{l}{h}, \frac{L}{h}, \frac{P}{\bar{E}h}, \alpha, \frac{r}{h}\right), \tag{3.4}$$

where r is the distance from the singularity. The dominant singularity, n, for each wedge of angle α can be found in Figure 3.9. This work only deals with planar geometries, with the normal stress fields are of the form[5]

$$\sigma = K_I\, r^n, \tag{3.5}$$

and shear stress fields

$$\tau = K_{II}\, r^n, \tag{3.6}$$

with the fillet angle α determining the strength of the singular field. This results in the stress-intensity factors of the form

$$K_I = g_I\left(\frac{l}{h}, \frac{P}{\bar{E}h}\right)\bar{E}h^n, \tag{3.7}$$

[5]As shown in Figure 3.9, the exponent n is defined as a negative value.

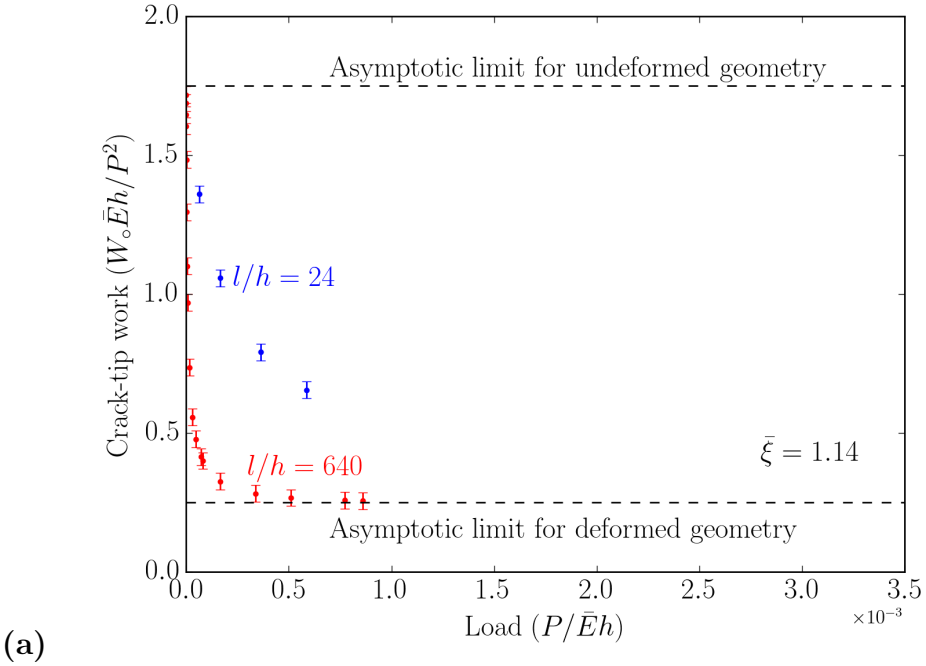

(a)

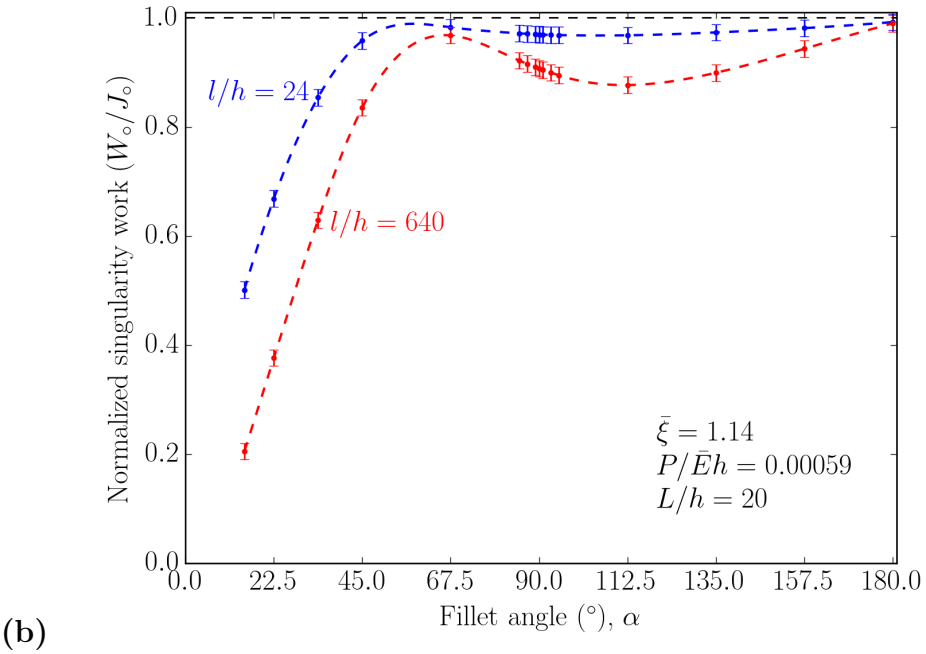

(b)

Figure 3.7: **(a)** The crack-tip work values for $\bar{\xi} = 1.14$ for two different ligament lengths: $l/h = 24$ and $l/h = 640$. As one can see in comparison to the elastic calculations in Figure 3.3, the CZM crack-tip work results fall in line with the elastic results. As mentioned before, a crack length of $a/h = 2$ and arm length of $L/h = 20$ were used for these calculations. **(b)** The normalized singularity work at $P/\bar{E}h = 0.00059$ for those results plotted in (a), where the results from $l/h = 640$ were interpolated from the closest data points. While a similar observation could be made in Figure 3.6, these results demonstrate a clear dependence of Equation (3.3) on the ligament length, l/h.

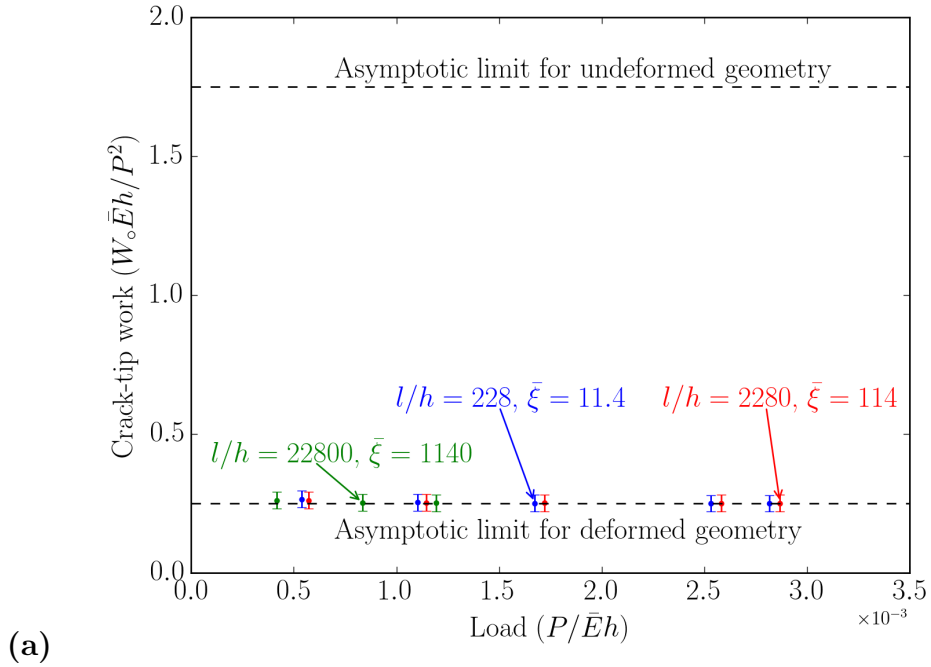

(a)

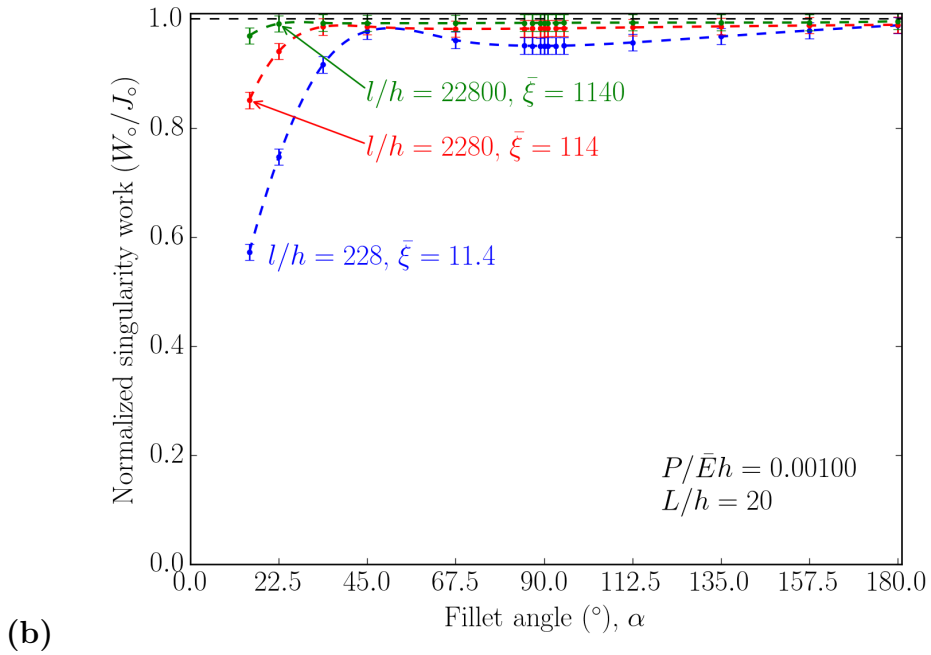

(b)

Figure 3.8: **(a)** The crack-tip work values for larger cohesive-length scales $\bar{\xi} = 11.4$, $\bar{\xi} = 114$, and $\bar{\xi} = 1140$ at different loads. One sees for the results considered, the loads are near the asymptotic limit for the deformed geometry. A crack length of $a/h = 2$ and arm length of $L/h = 20$ were used for these calculations. **(b)** The normalized singularity work for these larger cohesive-length scales, interpolated from the results closest to $P/\bar{E}h = 0.001$. At the largest cohesive-length scales, the singularity work function continues to be pushed towards unity for all fillet angles.

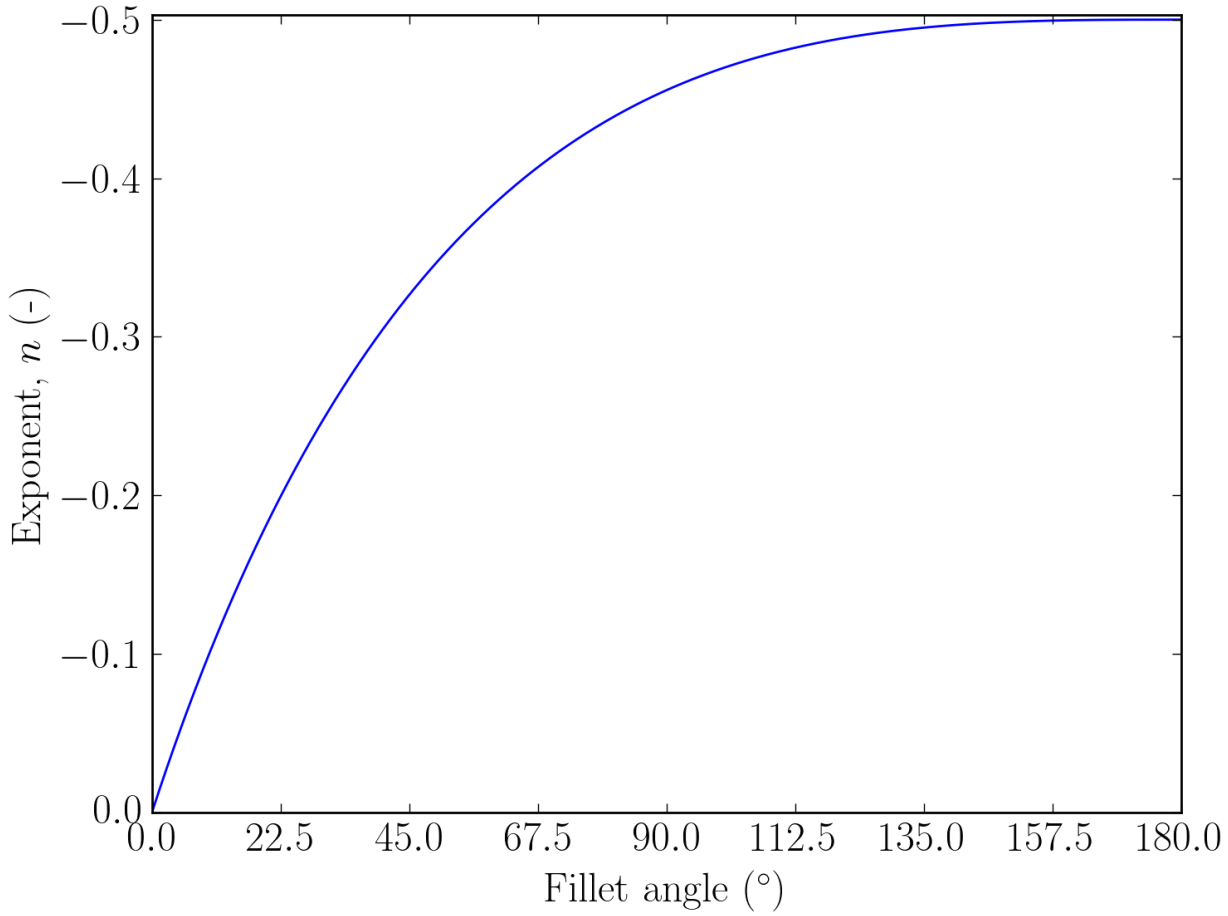

Figure 3.9: The strength of the symmetric singularity that increases with fillet angle [93]. Note that the exponent n as defined is negative.

and

$$K_{II} = g_{II}\left(\frac{l}{h}, \frac{P}{\bar{E}h}\right)\bar{E}h^n, \tag{3.8}$$

because L/h is held constant for all calculations. Any constant due to L/h and the usual factor of $\sqrt{2\pi}$ have been absorbed by the g_I and g_{II} here because of the use of generalized stress-intensity factors [94].

The stress fields, with the appropriate linear elasticity singularities inscribed on the plots, for a couple wedges ($\alpha = 90°$ and $180°$) are found in Figure 3.10. The length over which the cohesive-zone's stress field matches linear elasticity varies with the fillet angle. Similar observations were made for the other fillet angles considered here.

On each plot, the (normalized) stress-intensity factors are inscribed, and using these values one may determine the phase angle. However, with the exception of the crack-tip singularity, no other fillet angle has an analytical solution from LEFM. For the 180° fillet angle,

the measured stress-intensity factors are $K_I/\bar{E}\sqrt{h} = 0.00030$ and $K_{II}/\bar{E}\sqrt{h} = 0.00037$, which matched the elastic calculation. With an measurement uncertainty of about 0.000025, the measured phase angle is 51 ± 4 degrees, which is in good agreement with the LEFM value of 49.1°[6].

Mesh sensitivity calculations were run to verify the stresses converged. However, despite this convergence the 90° fillet angle calculation does not reproduce the stress-intensity factor ratio $K_I/K_{II} = 0.543$ one would expect from Ref. [94]. The theoretical singularity value for K_I as a dotted line while the measured K_{II} value, which agreed with the elastic calculation, is plotted as a dashed line. This suggests that non-crack singularities require a finer mesh to measure the singular field compared to a crack.

While LEFM may not have an analytical result for phase angles of non-crack singularities, the stress fields determined by the cohesive-zone model can still be used to back out a plot of the phase angle as a function of distance ahead of the crack-tip. At the smallest length scales, only the crack-tip singularity has an asymptote, as shown in Figure 3.11a. Here, one sees that the phase angle appropriately asymptotes to the LEFM, low-load phase angle limit of −49.1°[7]. As the cohesive-length scale increases, additional singularities begin to asymptote, as shown in Figure 3.11b.

Since the calculations were run across cohesive-length scales, one can compare all the phase angle plateaus at the LEFM condition, and Figure 3.12 displays these phase angle plateaus as a function of fillet angle. It has been shown [27] that a sharp crack will always asymptote to the LEFM phase angle provided the cohesive-length scales are small enough. One can see this result is replicated here, as all the data points lie around the LEFM phase angle value of -49.1°. The other fillet angles do not share this same property, as one sees that the values can change even when LEFM is expected to be an adequate approximation at all of them.

Having considered the LEFM results, it is now time to move to large cohesive-length scales. In Figure 3.8, it was shown that the normalized singularity work for all fillet angles began to approach unity at large cohesive-length scales. A comparable result is found in Figure 3.13 when one plots the phase angle for different fillet angles. In Figure 3.13a, the crack and orner singularities span around 5° for $\bar{\xi} = 11.4$. As a comparison, one can see that these same fillet angles would have spanned almost 20° for phase angle plateaus for $\bar{\xi} = 0.114$, as shown in Figure 3.11b. This phase angle difference continues to decrease

[6]The stiff adherend, low-load phase angle limit is 49.1° while the compliant adherend, large load LEFM phase angle limit for the single lap-shear joint is 63.1°, as derived in Ref. [20].

[7]Shear displacements are defined as positive for the top interface moving to the right of the bottom interface; therefore, the phase angle is negative here because the shear displacements at the singularities are negative.

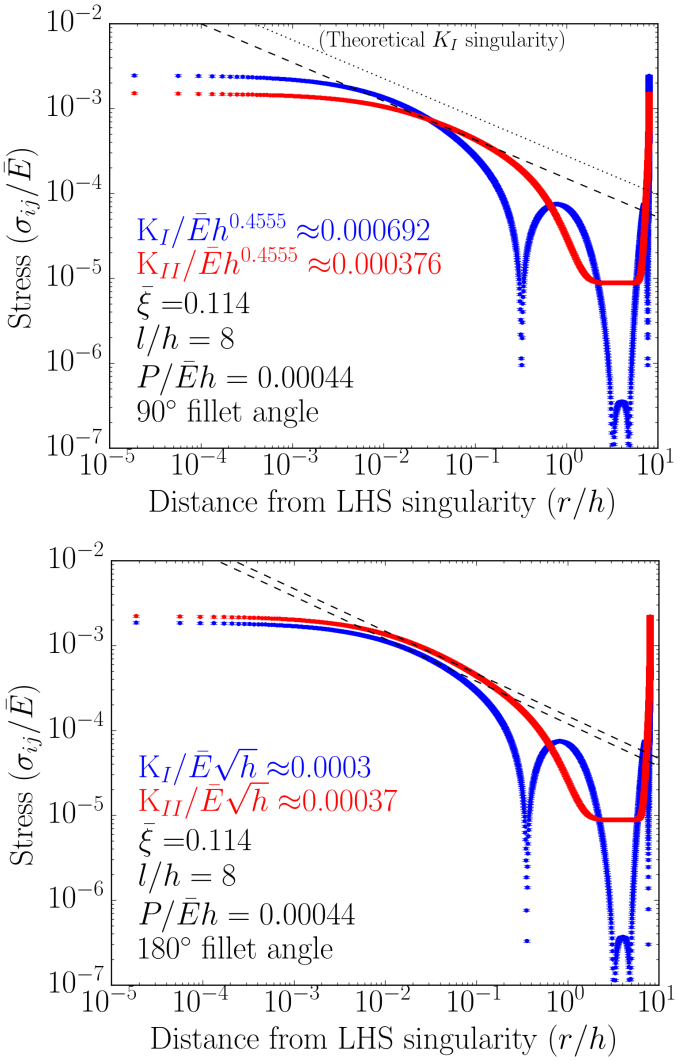

(a)

(b)

Figure 3.10: Absolute value of stress fields for **(a)** 90° and **(b)** 180° fillet angles. The stress fields are normalized by the elastic modulus, and inscribed on each plot is the corresponding singularity from Figure 3.9. In Ref. [27], it was shown for a crack that, provided the cohesive-length scale was small enough, a inverse square root singular field could be seen. Here it is observed, for a small enough cohesive-length scale, a portion of the CZM stress field may be fit to the LEFM singular stress field for non-crack singularities, although the length over which the CZM stress field is singular may be small. It is worth noting for (b), with an uncertainty of about 0.000025 on the (normalized) stress-intensity factors, the measured phase angle is 51 ± 4 degrees, which is in good agreement with the LEFM value of 49.1°. The stress-intensity factors also matched the elastic calculation. Mesh sensitivity calculations were run on the calculations to verify the stresses converged. The results are slightly different for a corner. The shear stress matched the elastic calculation, but the normal stresses did not. If one matches the mode-II stress-intesity factor (SIF), can then calculate the expected mode-I SIF predicted from Ref. [94], where $K_I/K_{II} = 0.543$. As one sees in (a), the mode-I SIF is not reproduced (the theoretical value is inscribed above as a dotted line, as is the theoretical value for K_I). This suggests that non-crack singularities require a finer mesh to reproduce the predicted singular field. $L/h = 20$ for all calculations.

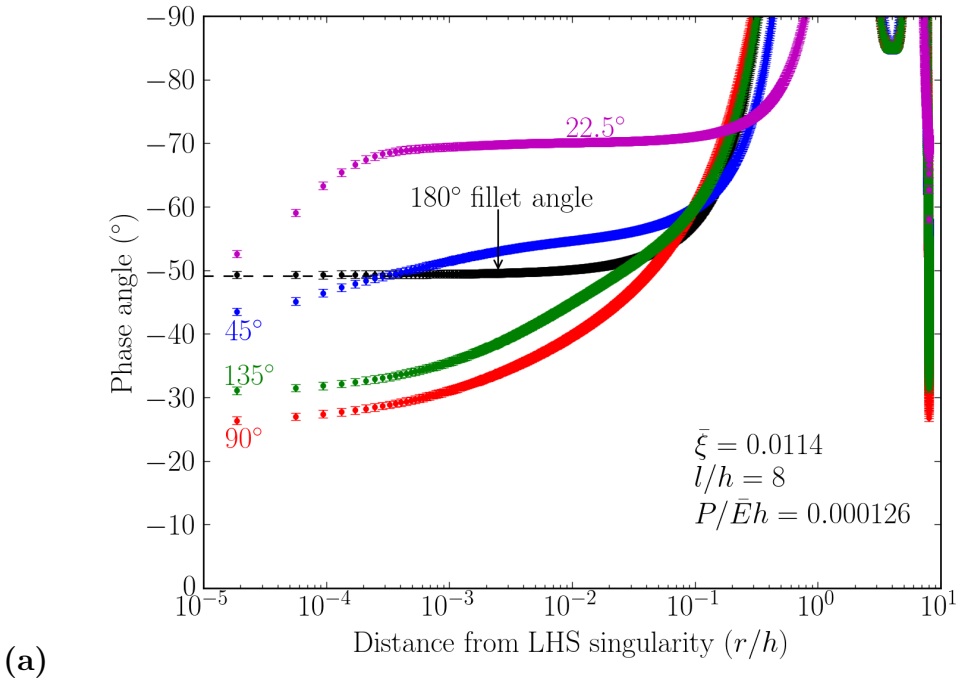

(a)

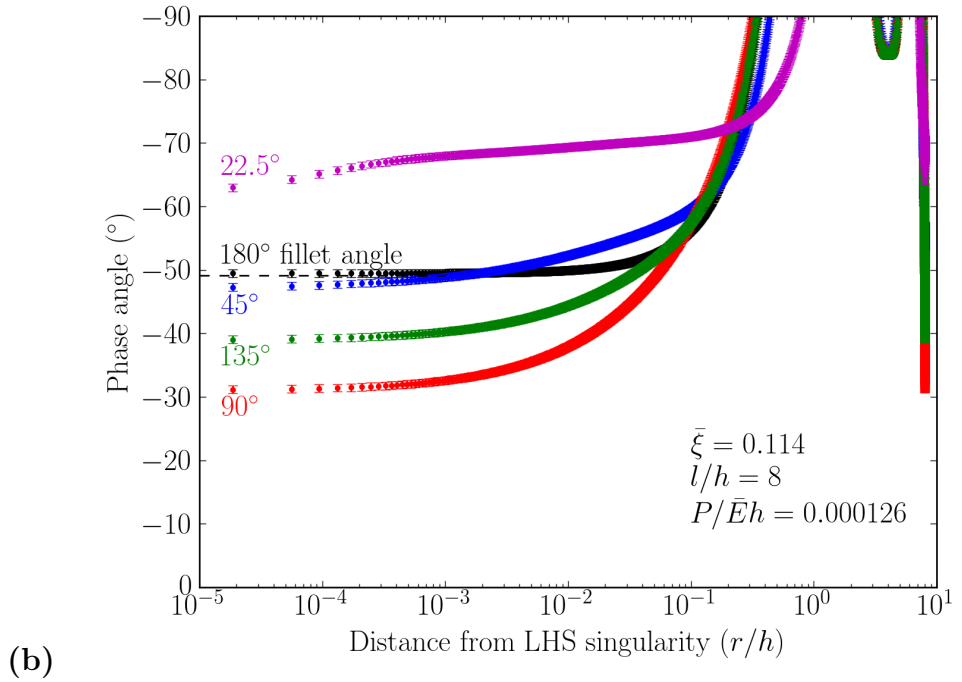

(b)

Figure 3.11: Phase angle plateaus of small cohesive-length scale calculations compared with the LEFM crack-tip phase angle for stiff adherends. **(a)** At the smallest cohesive-length scales, only the 180° fillet angle (crack) asymptotes; no other fillet angles show plateaus. **(b)** When the cohesive-length scale is increased near the edge of LEFM applicability, one begins to see other fillet angles begin to plateau as well. A sensitivity analysis showed that the results were mesh-insensitive. $L/h = 20$ for all calculations.

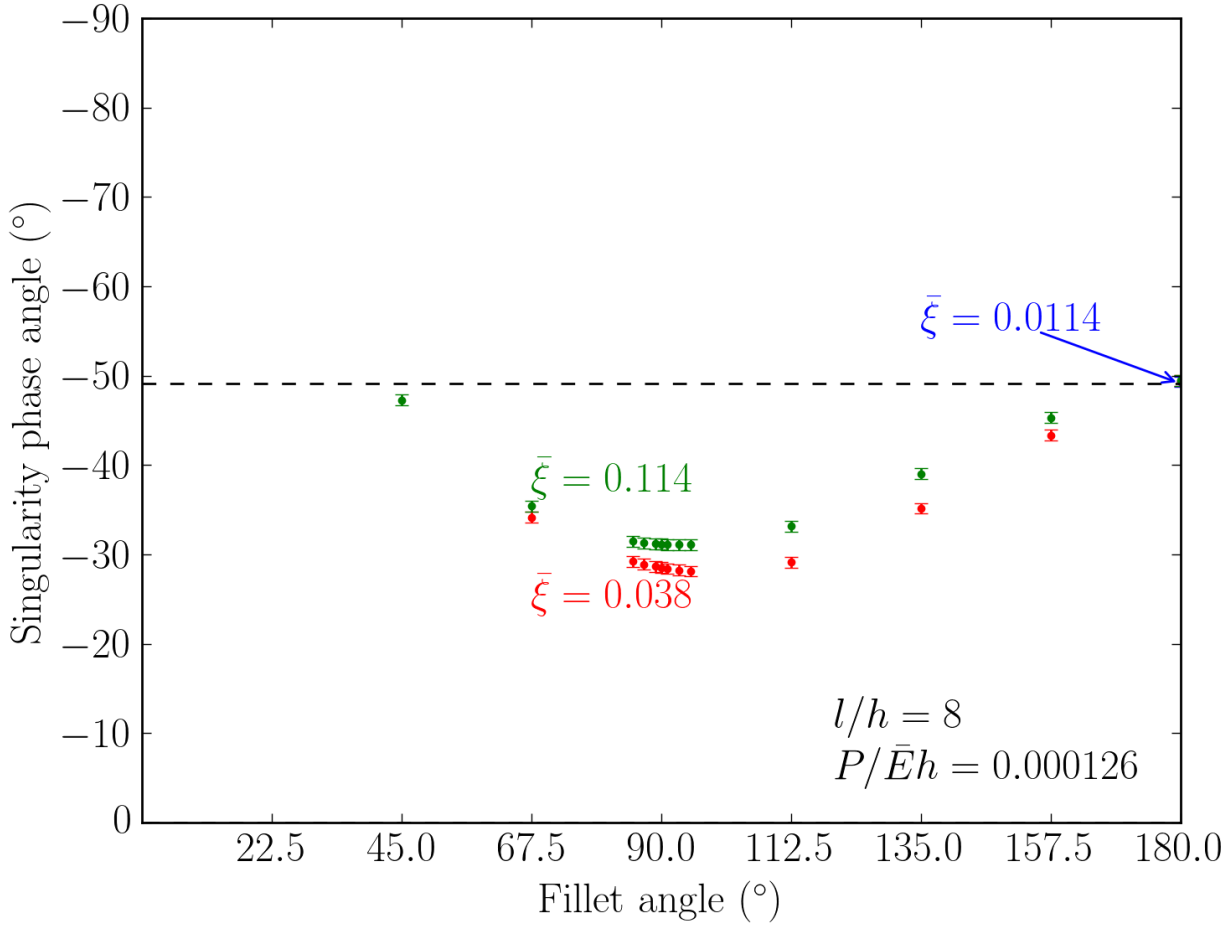

Figure 3.12: Phase angle plateaus as a function of cohesive-length scale and fillet angle. For a given ligament and load, one can see how the phase angle evolves. Please note that the dashed line corresponds to the LEFM crack-tip phase angle ($-49.1°$) for a lap-shear joint with stiff adherends loaded via an axial load and bending moment at small load values. $L/h = 20$ for all calculations.

as the cohesive-length scale increases, and the phase angles can hardly be distinguished in Figure 3.13b, when $\bar{\xi} = 114$.

In comparing the phase angles at large cohesive-length scales, it would be better to consider the relative changes in the phase angles rather than the specific values. Geometric contraints force the ligament length to increase as the cohesive-length scale increases, and these changes could obfuscate the findings and lead to unwarranted conclusions. To that end, the relative phase angle differences are plotted compared to the crack-tip phase angle value in Figure 3.14. The full results are plotted in Figure 3.14a, while some of the results are removed in Figure 3.14b to allow the reader to see the overall trend more easily.

At large cohesive-length scales, the fillet angles' phase angle plateaus converge to the crack-tip value. Above, it was suggested that if the large cohesive-length was large enough, the fine aspects are irrelevant. It is one thing to note, as done in Figure 3.8, that the work done at the singularity is independent of fillet angle at large cohesive-length scales. However, the phase angle information gives additional information: at large cohesive-length scales, fillet angles all have the same work done *and* the deformation occurs in the same manner. With a large enough cohesive-length, the deformation along an interface ahead of a singularity is indistinguishable for different fillet angles.

This ought be held in contrast to data at smaller cohesive-length scales. One should note that for the corner singularity at $\bar{\xi} = 0.114$, one can see that an experimentalist would probably not be able to ascertain the difference between a corner and crack by only considering the measured singularity work. This is most easily seen in Figure 3.6, where it can be observed that the work done at the corner singularity can be within a few percent of the elastic calculation's crack-tip value. The difference is small enough that any (experimentally measured) differences between samples would be dwarfed by manufacturing variability. However, if one had full-field measurement capabilities or another method of separating the mode-I and mode-II work at a singularity, then one might be able to see the differences in mixed-mode loading: the corner singularity is slightly mode-I dominant with a phase angle at almost -30°, while the crack-tip singularity barely has a mode-II preference with a phase angle around -50°.

3.3.3 Traction-separation law shape dependence

As observed in Figure 3.12, non-crack fillet angles change their phase angle plateaus at small cohesive-length scales when LEFM is expected to be valid. This is distinct from the response at a crack-tip [27], which was shown to asymptote to a single value if LEFM conditions were satisfied. As the corner is the typical non-crack singularity, example calculations were run at small cohesive-length scales with small variations in the mode-I/-II

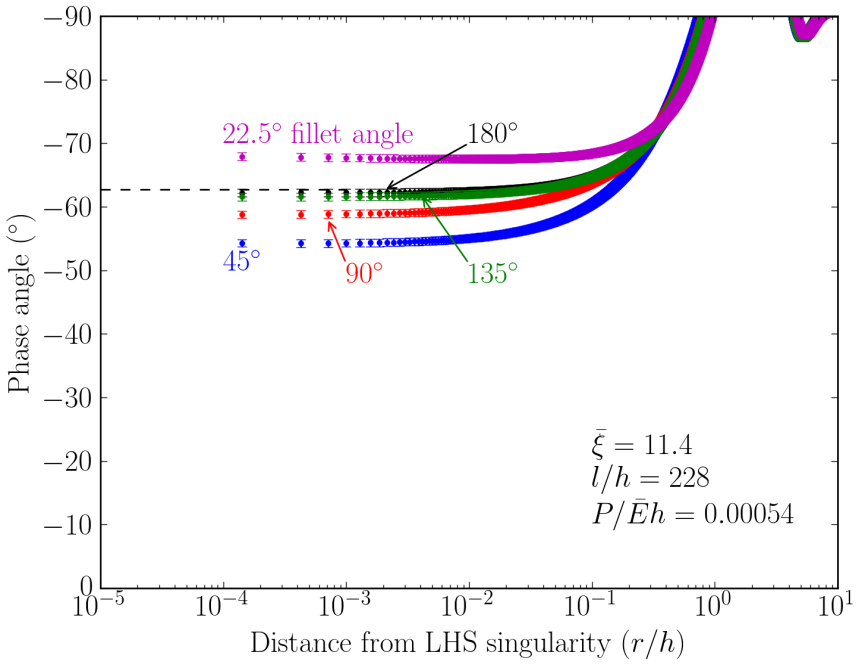

(a)

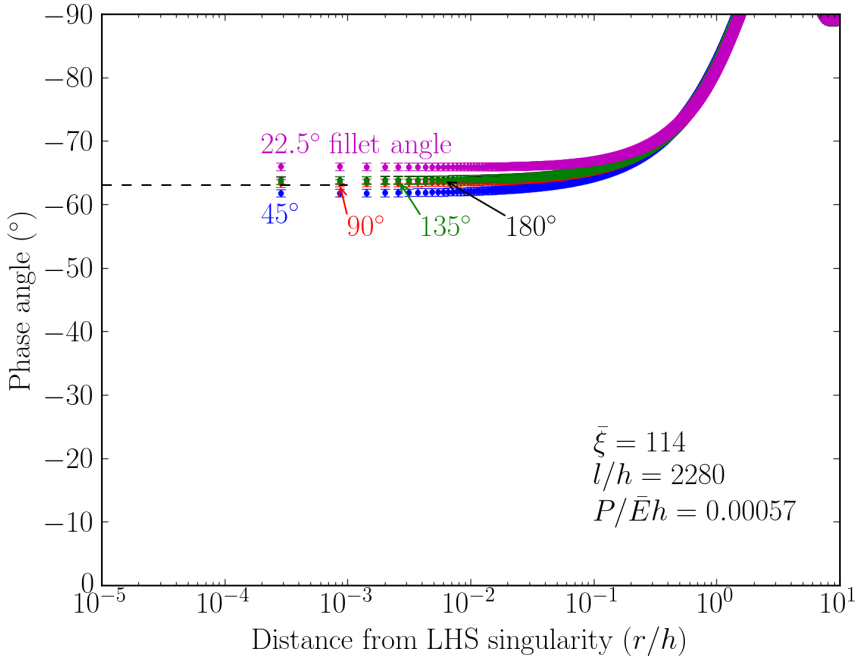

(b)

Figure 3.13: Phase angle plateaus at large cohesive-length scales at **(a)** $\bar{\xi} = 11.4$ and **(b)** $\bar{\xi} = 114$, with the LEFM phase angle inscribed on each plot as a dashed line. At larger cohesive-length scales, the phase angle plateaus begin to collapse onto a single curve for all fillet angles, one corresponding to the crack-tip. Perhaps surprisingly, the phase angles appear to collapse to a single value around the LEFM phase angle. $L/h = 20$ for all calculations.

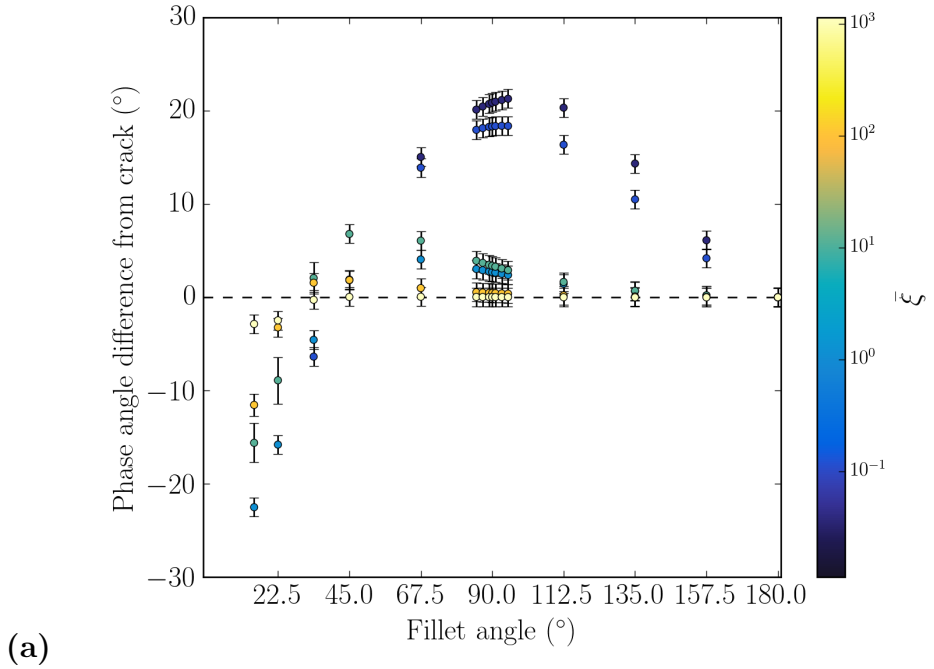

(a)

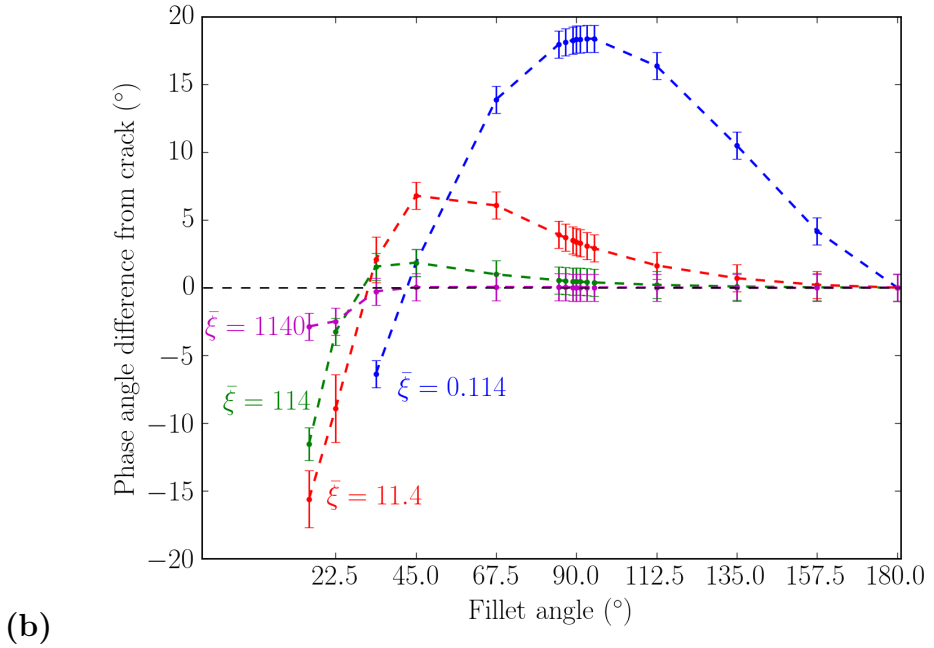

(b)

Figure 3.14: The phase angle convergence seen in Figure 3.13 is clearer when one compares the phase angle asymptotes relative to the crack-tip phase angle. Here, all phase angles are relative to the crack-tip value for all geometries. One notices that at small cohesive-length scales there is large variation from the crack-tip value. However, as the cohesve-length scale increases, all phase angle plateaus begin to collapse onto a single value. These results corroborate the findings in Figure 3.8: at large cohesive-length scales the precise nature of the singularity is irrelevant and a crack cannot be distinguished from different singularities. For $\bar{\xi} \leq 0.114$, $l/h = 8$ and $P/\bar{E}h = 0.00006 - 0.00044$; for $\bar{\xi} = 1.14$, $l/h = 24$ and $P/\bar{E}h = 0.00007 - 0.00059$; for $\bar{\xi} = 11.4$, $l/h = 228$ and $P/\bar{E}h = 0.00054 - 0.00282$; for $\bar{\xi} = 114$, $l/h = 2280$ and $P/\bar{E}h = 0.00058 - 0.00287$; and for $\bar{\xi} = 1140$, $l/h = 22800$ and $P/\bar{E}h = 0.00042 - 0.00119$. $L/h = 20$ for all calculations.

traction-separation laws. When different traction-separation laws are used, $\bar{\xi}_I$ and $\bar{\xi}_{II}$ are independent from each other. This requires that a composite (average) cohesive-length scale,

$$\bar{\xi}^* = \frac{W_I\,\bar{\xi}_I + W_{II}\,\bar{\xi}_{II}}{W_I + W_{II}} = \frac{\bar{E}(\delta_{I,\circ}^2 + \delta_{II,\circ}^2)}{(W_{I,\circ} + W_{II,\circ})h} \tag{3.9}$$

be introduced. In the case where identical linear traction-separation laws are used, $\bar{\xi}^* = \bar{\xi}_I = \bar{\xi}_{II} = \bar{\xi}$.

Figure 3.15 shows five different combinations of linear traction-separation laws, with the composite cohesive-length scale centered around the value $\bar{\xi}^* = 0.06$. Taking into account the numerical uncertainty, the five calculations had equal values of work done at the singularity. Yet, the calculations partitioned this work differently because the phase angles are distinct. This finding was observed for other fillet angles as well.

Looking closely at the data in Figure 3.15, one might notice a systematic trend in the change in phase angle. If one plots the phase angle asymptote versus the composite cohesive-length scale one can find an affine fit. In the other fillet angles analyzed but not shown here, this was also found to be the case. The slope of the phase angle asymptote versus composite CLS affine fits tend to decrease with increasing fillet angle. This seems reasonable, as once the fillet angle reaches 180°, in the LEFM regime it is expected to asymptote to a single value for a fine enough mesh. No significance of this relationship could be determined by the author, other than the observation that in the LEFM regime one would expect small changes in initial conditions would result in small changes in the outcome. It was beyond the scope of this work to pursue this observation further.

Having looked at changes in constant cohesive-length scales, one should consider how the shape of the traction-separation law affects the phase angle. The use of the Dugdale law (a sharp initial vertical slope on the traction-separation law followed by a constant stress) allows quick accumulation of different composite cohesive-length scales. Due to the changing cohesive-length scales, the Dugdale law calculations were run first to determine the mode-I/-II cohesive-length scales. Then, the geometry, loads, and cohesive-length scales were matched to original calculation to ensure the only difference between the calculations was the shape of the traction-separation law.

The results of these separate sets of calculations can be found in Figure 3.16, with the Dugdale law results plotted in (a) and mixed-linear law results in (b). When qualitatively comparing the plateaus in Figure 3.16a and Figure 3.16b, one sees the shape of the traction-separation laws play a role in the phase angle plateaus for the corner singularity. This expands on the findings from Ref. [27] where the shape of the traction-separation law was shown to change how the phase angle behaved ahead of the crack-tip. For any fillet angle,

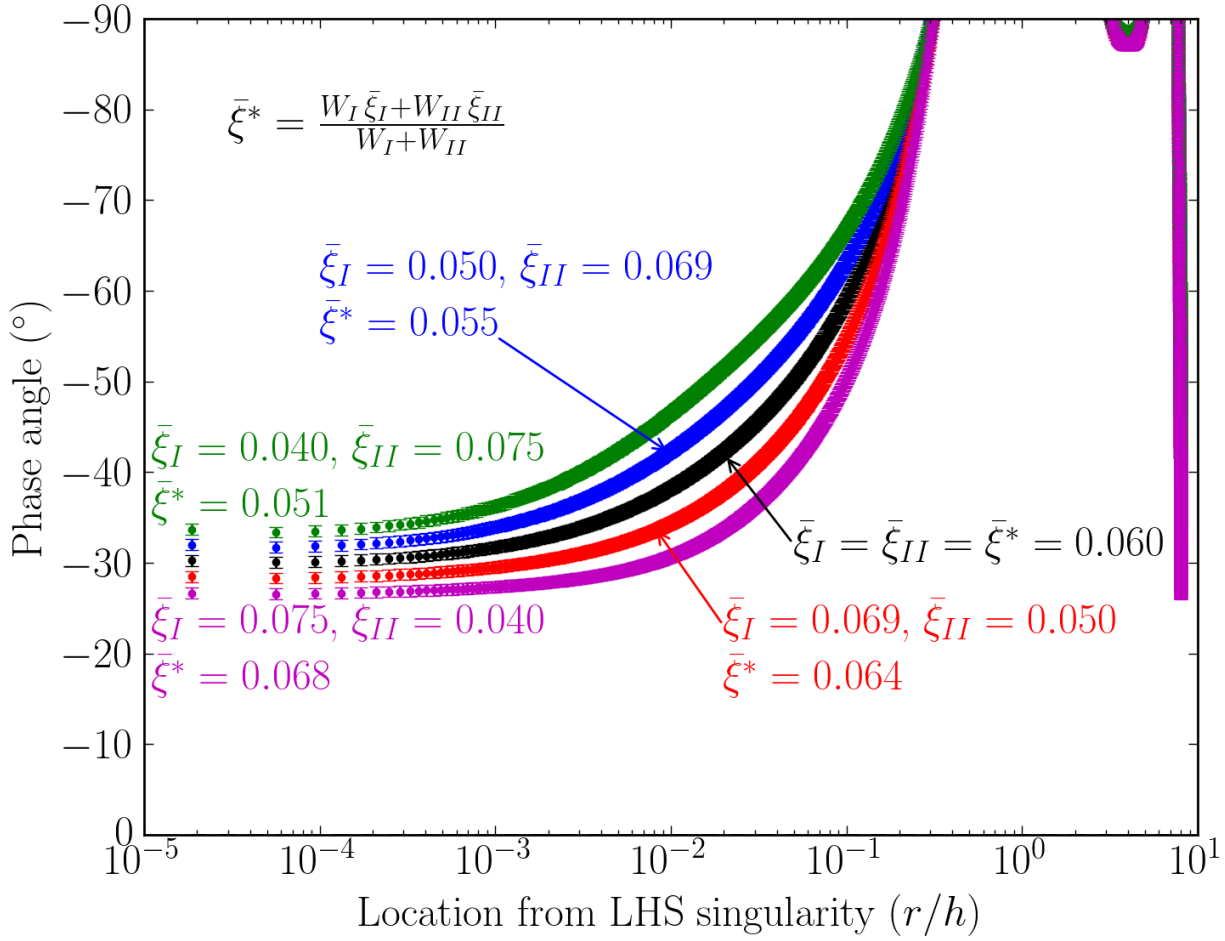

Figure 3.15: Using the 90° fillet as the prototypical example, the composite cohesive-length scale is kept at an approximately constant value of $\bar{\xi}^* = 0.06 \pm 0.01$. In doing so, one observes a shift in the phase angle as the $\bar{\xi}_I$, $\bar{\xi}_{II}$ combination changes, even with only small variations. Shifts in the phase angle asymptote were seen with other fillet angles as well, with the exception of the crack (Ref. [27] showed for a crack that all traction-separation laws approached the LEFM phase angle, provided the cohesive-length scales were small enough). The other non-dimensional groups for these calculations: $l/h = 8$, $L/h = 20$, $P/\bar{E}h = 0.00044$, and $\alpha = 90°$.

the shape of the cohesive laws will play a role in how the phase angle behaves ahead of a singularity.

Above it was shown for non-crack singularities that the phase angle asymptote changes with the cohesive-length scale, even when LEFM is expected to be a useful approximation. Here, it is demonstrated that the shape of the traction-separation law *also* changes the phase angle asymptote, even when the load and composite cohesive-length scale is held constant. This is exemplified in Figure 3.16a, where the mixed-linear law asymptotes from Figure 3.16b have been inscribed. Again, the only difference between the two sets of calculations are the shapes of the cohesive laws: Dugdale laws in Figure 3.16a and mixed-linear laws in Figure 3.16b. It is worth noting that simply using the individually-indentified cohesive-length scales (*i.e.* $\bar{\xi}_I \equiv \bar{E}\,\delta_{I,\circ}^2/W_{I,\circ}\,h$ and $\bar{\xi}_{II} \equiv \bar{E}\,\delta_{II,\circ}^2/W_{II,\circ}\,h$) does not necessarliy imply the same composite cohesive-length scale $\bar{\xi}^*$[8] due to the work partitioning at the singularity. There exists a negligible difference between the singularity work for the separate different traction-separation laws, but the work is partitioned slightly differently at the corner for different traction-separation laws.

3.4 Summary

Many groups previously observed, whether qualitatively or quantitatively, that sharp cracks and corners could be interchanged in single lap-shear joints without effect on failure, even though linear-elastic fracture mechanics requires a crack theoretically. It was shown that at relatively small cohesive-length scales (when LEFM is still a useful approximation), the work done at the corner is experimentally indistinguishable from that at the crack-tip. This might have led some to conclude there was something special about the 90° fillet angle singularity. However, looking at the broader context one realizes there is nothing special about the 90° fillet angle and similar results would be found for the 85° or 95° fillet angles. The corner singularity stands out because it is easiest non-crack singularity to manufacture. These findings also suggest it might be more appropriate to move away from the term "energy-release rate" when using the cohesive-zone model and instead use "singularity work" or "crack-tip work" to distinguish between linear-elastic fracture mechanics and the cohesive-zone model, as there is still work done against the tractions at the singularity.

As one increases the cohesive-length, the fine aspects of the singularity are swamped and the singular field disappears. Furthermore, at a large enough cohesive-length, all the

[8] A few of the calculations required a brute-force attempt to reach agreement between the composite cohesive-length scale values, and the data plotted differ by less than 1%. However, it should be noted that the phase angle data plotted in Figure 3.16b was negligibly different than the original calculations which used the individually-indentified cohesive-length scales: $\bar{\xi}_I \equiv \bar{E}\,\delta_{I,\circ}^2/W_{I,\circ}\,h$ and $\bar{\xi}_{II} \equiv \bar{E}\,\delta_{II,\circ}^2/W_{II,\circ}\,h$.

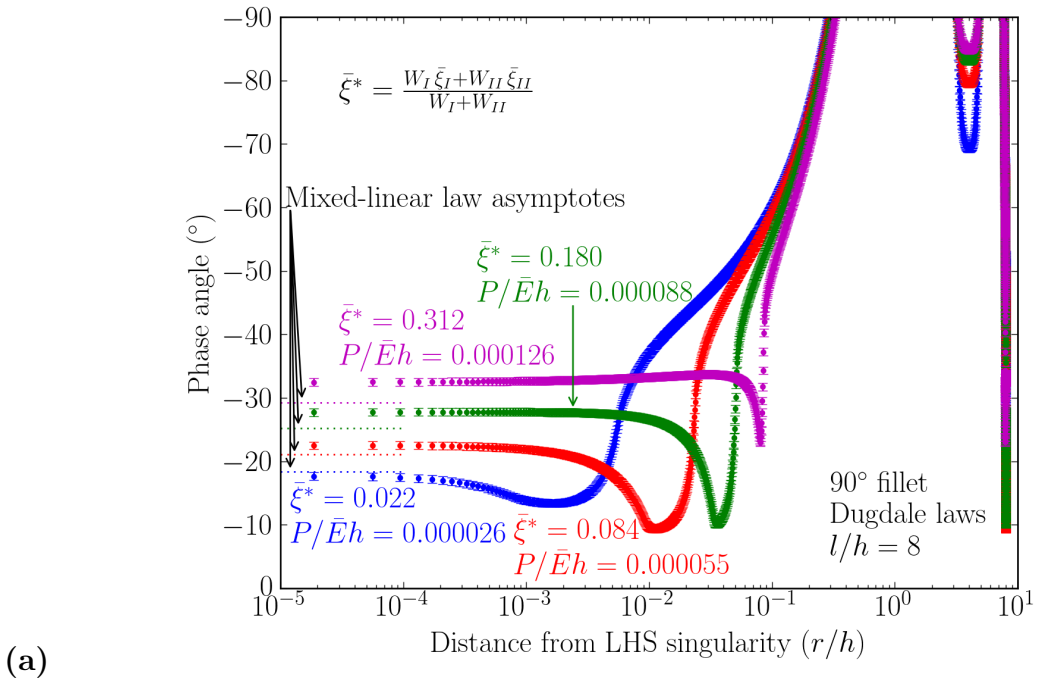

(a)

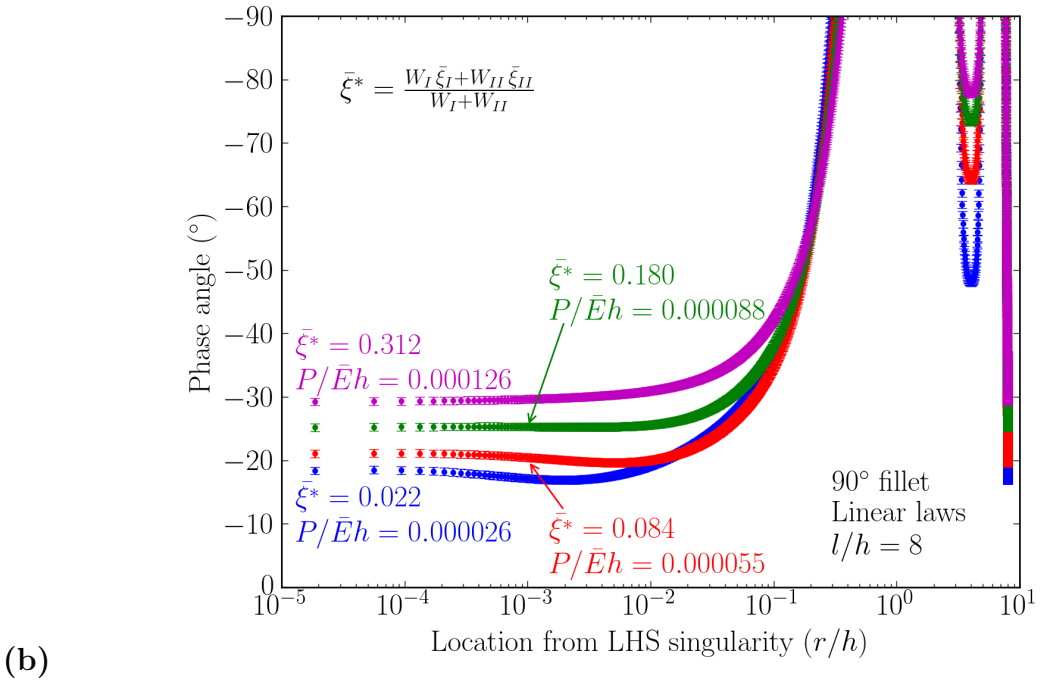

(b)

Figure 3.16: Effect of different traction-separation laws on the phase angle plateau for non-crack fillet angles. **(a)** These plateaus are generated using Dugdale laws, where four instances were chosen with different composite cohesive-length scales. These same composite cohesive-length scale values were then implemented using mixed-linear laws in **(b)**. For comparison, the dotted lines in (a) correspond to the mixed-linear law asymptotes from (b). These findings suggest that the asymptotic phase angle of a fillet angle depends on the shape of the traction-separation laws for non-crack fillet angles, as the only difference between the two calculations was the choice of the cohesive laws. The paired calculations had equivalent values of work done at the singularity to within numerical uncertainty. $L/h = 20$ for all calculations.

work done at the singularity (for all fillet angles) approaches the crack-tip work value, and the phase angles converge to the crack-tip value. Therefore, when the cohesive-length is large enough, the deformation ahead of the singularity gives no indication of the singularity present in the lap-shear joint.

Unlike the crack-tip singularity, it was observed that non-crack singularities have cohesive-length scale phase angle plateau dependence. Furthermore, the phase angle plateau is determined by both the cohesive-length scale *and* the shape of the traction-separation law. Although only these conclusions were made using the single lap-shear joint, one expects these findings to be applicable to other specimen geometries as well.

CHAPTER 4

Implications of Shear Loading and Geometric Constraints on the Single Lap-Shear Joint

4.1 Overview

Having laid groundwork in Chapter 3, one may now consider additional aspects of the single lap-shear joint. In the previous chapter, geometry considerations were neglected with the exception of the fillet angle, and the lap-shear joint was loaded only via an axial-load and bending moment. Now it is time to relax some of the geometric assumptions and include a reactionary shear load to provide a more complete description of the single lap-shear joint.

Goland and Reissner [95] were the first to consider the effect of an applied shear load on the lap-shear joint; however, the significance of this shear load appears to be missed by many [81, 82, 96, 85, 97]. One consequence of neglecting the applied shear load is that the compensating bending moment required for moment balance may be incorrect unless measured separately. These unknown/incorrect loads would then result in an incorrect measurement of the crack-tip work if only the axial load is measured.

ASTM standards [88, 89] provide a qualitative method for comparing shear strength's of lap-shear joints for one set of geometry parameters, but they are not able to provide quantitative information because it has been shown the joint's geometry affects the average shear strength [20]. A number of groups [90, 20, 98, 99, 100] have considered geometric effects when analysing the lap-shear joint. None of these analyses, however, considered how a varying cohesive-length scale changed the specimen's response and how geometry constraints may change delamination.

This chapter is divided into four main thrusts. The first will introduce some of the complications that arise in the single lap-shear joint due to an unknown shear load that must occur in the general loading (*i.e.* when it is clamped) and why it should not be ignored. Next, some initial findings will be presented concerning the effect of a constrained ligament

size with an increasing cohesive-length scale. A virtual experiment will then be used to introduce two methods one can use to analyze a single lap-shear joint with an unknown shear load: the use of the large-deformation J-integral and a numerical partial-model. The chapter concludes with the experimental validation of the numerical partial-model method.

4.2 Complication due to shear

As shown in the previous chapter, there are benefits to loading the lap-shear joint via axial loads and bending moments, but this loading configuration is often not achieved during testing. The necessity of the applied shear load can be determined through careful consideration of the free-body diagram. In Figure 4.1a, one sees how the lap-shear joint is commonly drawn, with an axial load N acting at each end of the specimen. However, when the geometry is loaded in an experiment and the ends of the lap-shear joint (with or without tabs) are clamped, the vertical motion is restricted. The case of wedge grips is considered in Figure 4.1b, where the two tabs are clamped. Due to specimen geometry, if only an axial load were applied in Figure 4.1a, the two tab regions at either end would move away from one another (and probably rotate). Restricting this vertical motion implies a reactionary shear force must be applied, and a compensating bending moment is required for moment balance and to restict any rotation in the tabs, as shown in Figure 4.1c.

The unknown shear load complicates the analysis of the lap-shear joint. Ref. [55] used FEM to calculate the increase in the energy-release rate due to an applied shear load, and notes the effect of shear depends on the details of the crack-tip deformation. Recall from Ref. [20] that geometry variations changed the failure load of the single lap-shear joint. One finds the same challenge when dealing with the unknown shear load. Therefore, not only does the size of the shear load depend on the geometry, but the effect that the shear load has on the crack-tip work is also dependent on the geometry.

The shear load may be determined anywhere along the beam-like geometry using a full-field measurement technique like digital image correlation. Unfortunately, DIC often requires users to balance the amount of the geometry one wishes to measure with the measurement resolution; therefore, one may not be able to capture displacements along the entire specimen. Such a constrained view is considered in Figure 4.1d. Assuming one measures the axial load via a load cell, one has three unknown values: an unknown shear load[1] V and two unknown bending moments, M_1 and M_2. The number of unknowns can be reduced using the moment

[1]The author advises against using the measured shear strain results from DIC to compute the shear load, as the rotations are expected to be the larger derivative value instead of the strains. Therefore, the author suggests using the beams' curvatures to extract the moments, and then using moment balance to extract the shear load. If one has high enough strain resolution, the measured strains could be used as a sanity check.

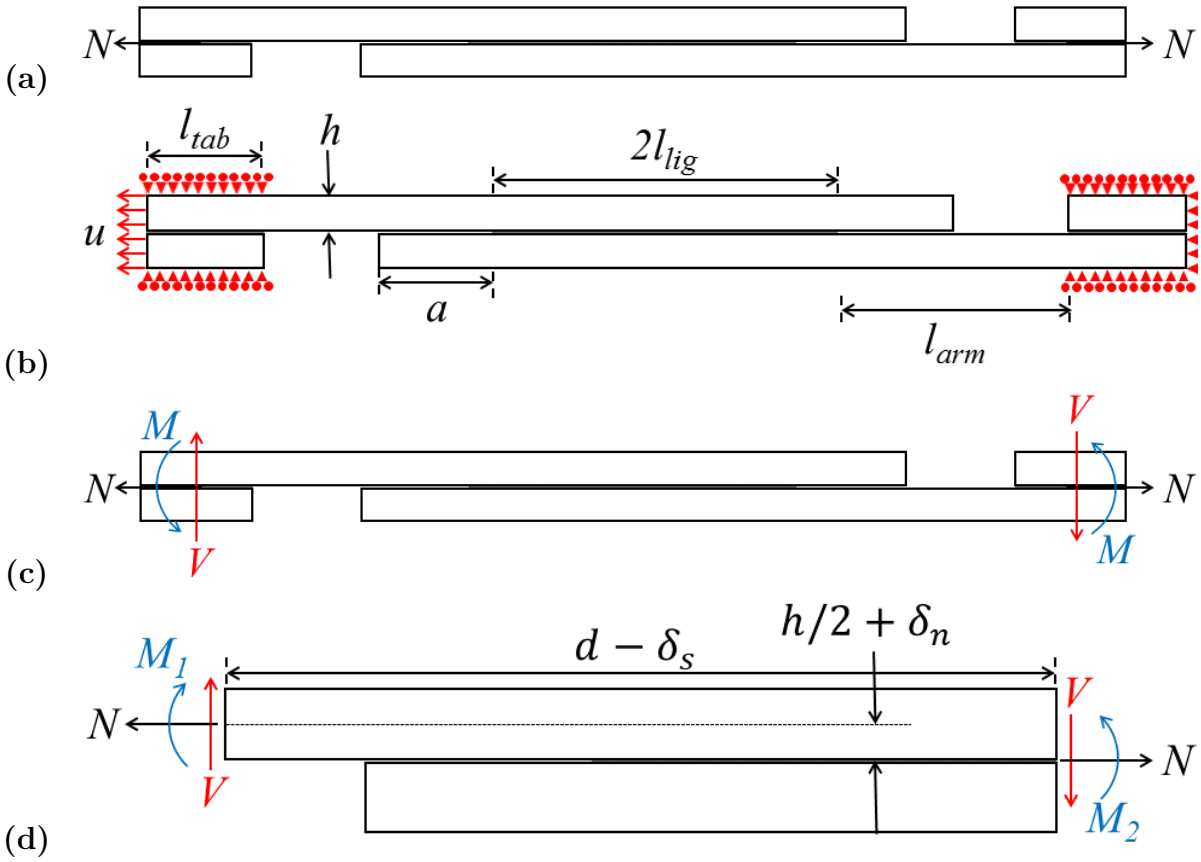

Figure 4.1: **(a)** Free-body diagram of the lap-shear joint how it is often drawn. **(b)** By testing the lap-shear joint using wedge grips (or another method that clamps the ends), the vertical displacement of the two ends are restricted. **(c)** By restricting the vertical motion, an unknown shear load and bending moment is required for the tabs not to move vertically nor rotate within the grips. **(d)** When considering the general loading of the single lap-shear joint with a constrained field of view, one must measure the axial load, shear load, and two bending moments. The axial load is typically measured via a load cell in an experiment. However, the shear load and bending moments are (generally) unknown. Using full-field measurement techniques, one can extract the curvatures at two points and use moment balance to determine the unknown shear load. Note that in an anti-symmetric lap-shear joint, the bending moment in the middle of the joint must be zero, and in this case only one of the bending moments would need to be determined. However, in general one may not assume the second bending moment is known.

balance equation, which requires

$$N(\frac{h}{2}+\delta_n)-V(d-\delta_s)-M_1+M_2=0 \tag{4.1}$$

for an lap-shear joint with a neglible interface thickness and beam arms of thickness h, where δ_n and δ_s are the relative normal and shear displacements from where the loads are taken. In the case of an anti-symmetric system, one also knows the bending moment in the middle of the lap-shear joint must equal zero.

Starting with the displacement data, one may differentiate the results by treating the data as a continuous, analog function of position. After extracting the beam rotations, $(dv/dx - du/dy)/2$, one may then differentiate the rotation data along the length of the beams to extract the curvature. Using beam theory, one can determine the bending moment from the curvature κ using

$$M = \bar{E}\, I_{\bar{E}}\, \kappa, \tag{4.2}$$

where $\bar{E}$ is the elastic modulus and $I_{\bar{E}}$ is second moment of area. With the bending moments now able to be determined, the shear load is the only unknown in the moment balance, Equation (4.1). With the capabilities of full-field measurements, one can extract the shear load at multiple locations along the beams since the curvature can be extracted along the entire length. This was done in a numerical example in Section 4.4.

To see the extent to which the reactionary shear load may vary, a selection of numerical calculations were run. The commercial finite-element software Abaqus 6.14 [1] was used for the calculations used here and below, and the cohesive-zone model was implemented using a FORTRAN subroutine (Appendix A) as a user-defined element. The ligament and arm lengths were chosen to span commonly-used sizes from the literature [88, 89, 20, 98, 99, 85, 86, 3]. In Figure 4.2a, one sees the relative shear load increases significantly for lap-shear joints with short ligaments and stubby arms. Furthermore, one sees that as the arm length becomes significantly greater than the ligament length the relative shear load tends toward zero.

While it is good to know the unknown shear load changes with geometry, this is particularly important because the shear load impacts the crack-tip work, and, therefore, when a crack will propagate along the interface. Figure 4.2b shows the difference in the normalized crack-tip work when one assumes only an axial load is acting at the crack-tip versus when the reactionary shear load is present. It was initially surprising to the author that the clamped calculation had a smaller crack-tip work. This can be reconciled when one looks at the free body diagram and realizes the bending moment acting at the crack-tip is smaller because the shear load portion is acting opposite to the axial load.

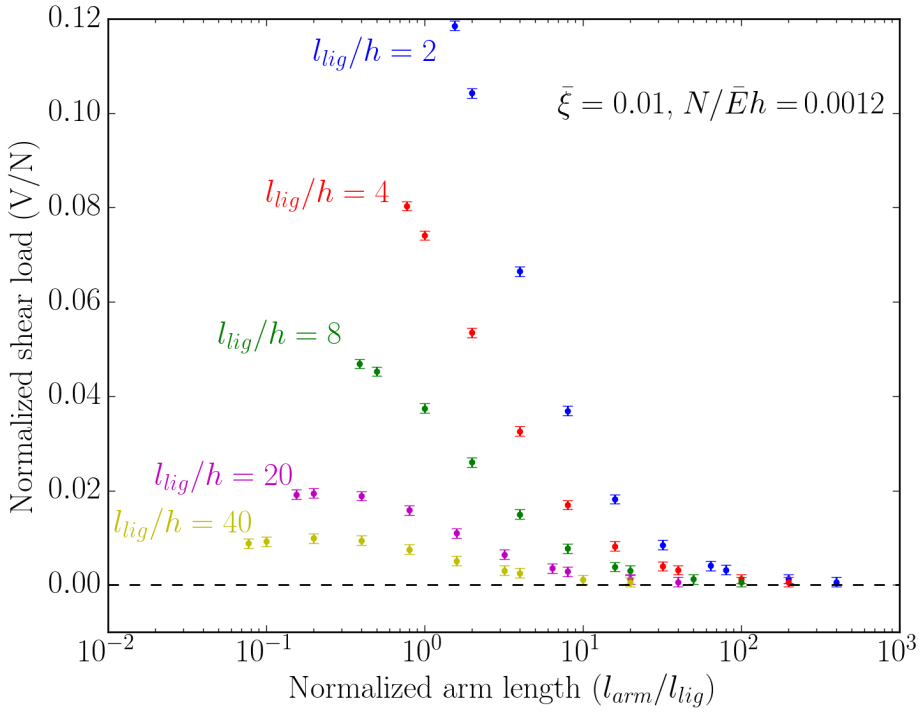

(a)

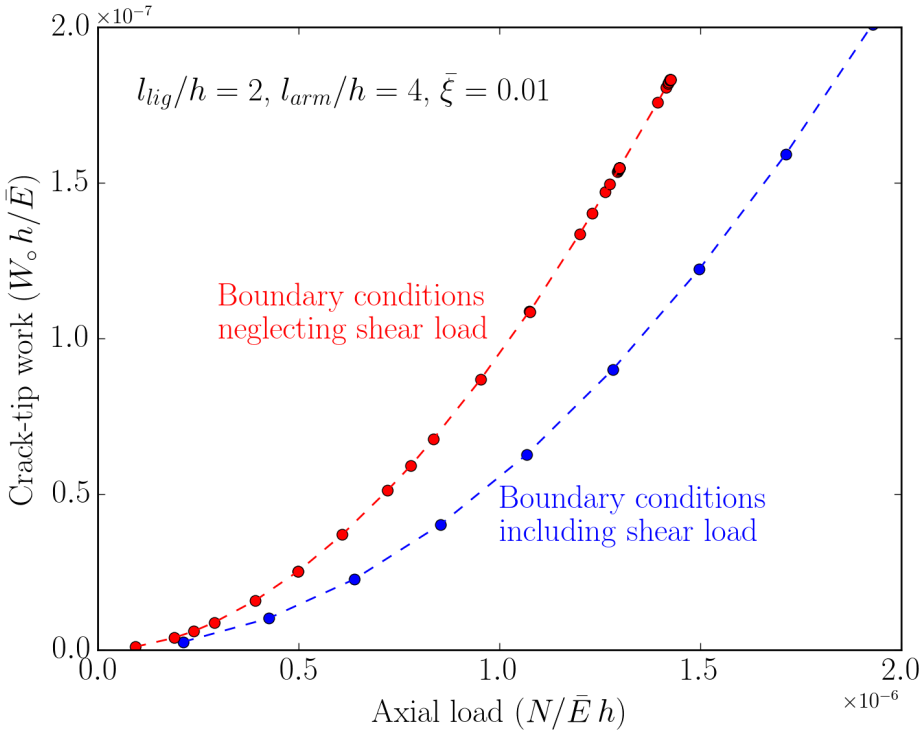

(b)

Figure 4.2: The effect of the reactionary shear load. **(a)** Shear load variation compared to the normalized arm length for four different ligament lengths. In the plot above, one sees how changing the arm length or ligament length will change the reaction shear load at the gripped tabs. **(b)** This unknown shear load can change the crack-tip work. One sees that neglecting the unknown shear load can overpredict the crack-tip work.

When the arm lengths are long enough, the difference between the two crack-tip work values becomes negligible, as shown in Figure 4.3a. For the ligament lengths considered here, the difference between the crack-tip work becomes negligible depends on the length of the bonded ligament. For the ligament lengths considered here, that can be between $2h$ and $50h$. Similar differences may be seen between the two loading assumptions for the crack-tip phase angle. However, in this instance the differences of crack-tip work partitioning (*i.e.* phase angle) are negligible at even smaller smaller arm lengths that can be $1h$ or less, as seen in Figure 4.3b.

In all cases considered here, the systems with the stubby-armed lap-shear joints were most affected by the shear load. While one solution might be to simply increase the length of the arms, there are unintended consequences with this approach. For thick enough arms that remain elastic, this will lead to additional stored energy in the beams that may cause catastrophic failure once a crack begins propagating. If the beams are thin enough and loads high enough, one then needs to worry about plasticity effects [20], which might change the traction-separation law behavior of the bonded adhesive. Two experimental methods to deal with the effect of shear are presented in Section 4.4.

4.3 Geometric constraints

While some of the geometry effects have been explored in the previous section, all the work thus far has been at small cohesive-length scales where LEFM has been applicable. Geometric constraints are generally not a concern when dealing with brittle materials, because the (crack-tip) singular stresses decay quickly, and the opening and shear displacements drop off quickly as well. However, as shown in Refs. [26, 28, 92], the stress and displacement fields take longer to decay at large cohesive-length scales. Recall from Chapter 3 that when the total bonded ligament length was twenty times the cohesive-length, the stresses and displacements had become small enough as to be neglected. From Chapter 2, one sees an instance experimentally of an adhesive with a (mode-I) cohesive-length on the order of a meter during the course of loading. Such systems would be experimentally impractical if all testing required bonded joints to have ligaments twenty times (or even ten times) such a large cohesive-length.

When the cohesive-length is not significantly smaller than all other geometric feature, the stress field has been shown to become more uniform [26, 28]. This phenonmenon is observed in Figure 4.4. In both cases (and those not included here), the increase in cohesive-length scale for a constrained geometry pushes the phase angle toward pure shear. This finding is similar to the findings of Ref. [26] where a mode-I preferred geometry was pushed towards

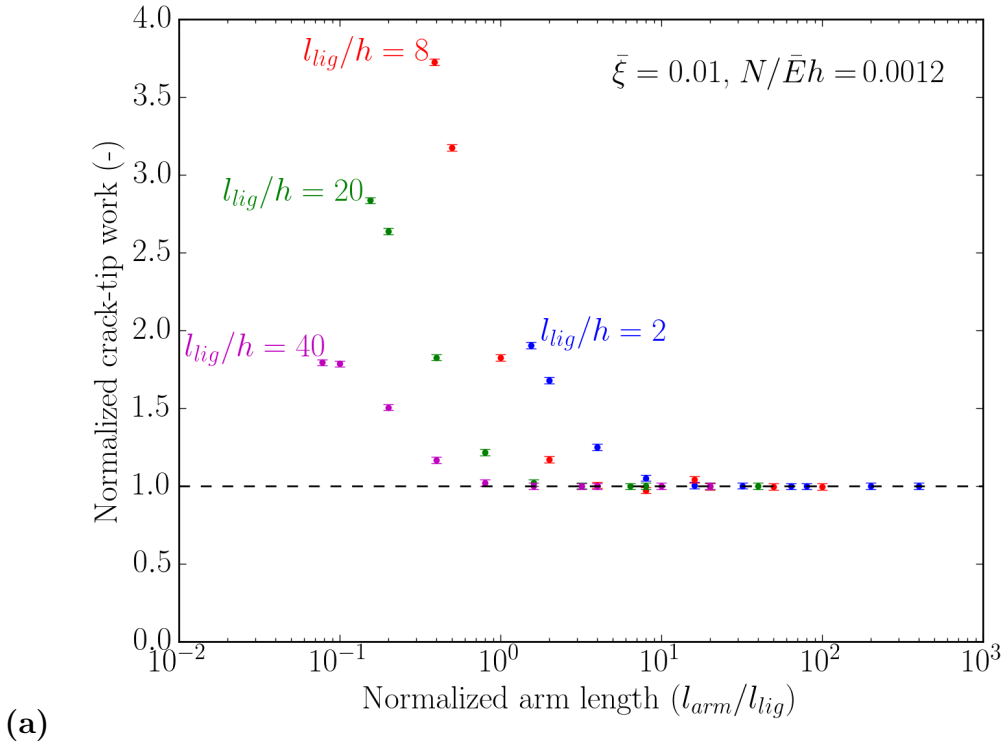

(a)

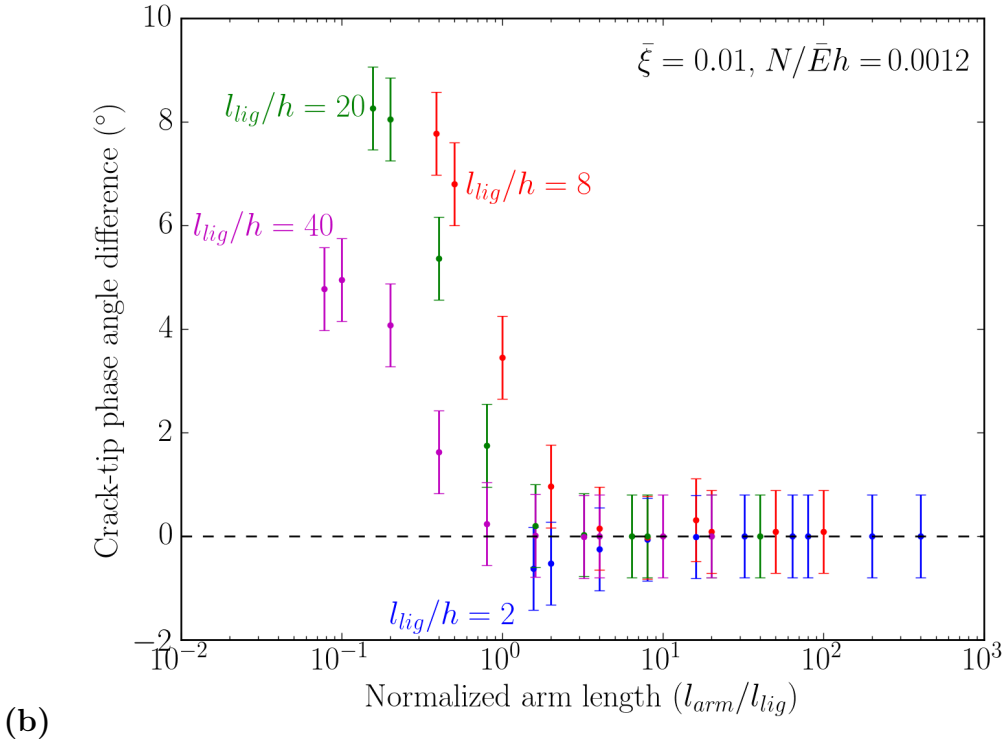

(b)

Figure 4.3: The effect of the reactionary shear load at the crack-tip. **(a)** One see the crack-tip work can be significantly overpredicted if the shear load is not taken into account, particularly at small l_{arm}/l_{lig} ratios. **(b)** With different loads assumed for the two different calculations, it is not surprising the crack-tip phase angles are different. The phase angles converge at much smaller l_{arm}/l_{lig} ratios than the crack-tip work.

pure opening at large cohesive-length scales.

The findings from Chapter 3 demonstrate how the choice of fillet angle can slightly change these overall trends. Recall from Figures 3.11b and 3.15 that at small cohesive-length scales the corner singularity is slightly mode-I dominant, and from Figure 3.14 that at large cohesive-length scales the two singularities behave the same way because the fine aspects are swamped. Had a corner singularity been used instead of a crack, this results in a switch in the phase angle from a mode-I to mode-II preference with an increasing cohesive-length scale, although these results are not included here.

Apart from changing the type of loading across the interface, a large cohesive-length scale can also change the magnitude of the reactionary shear load in a constrained geometry. In Figure 4.5, one sees how the relative shear load can change as one changes the cohesive-length scale. Furthermore, the calculations are normalized by the horizontal displacement because the axial load is also changed by the cohesive-length scale. Therefore, the reaction forces are dependent on not only the geometric features of the specimen, but also the shape of the traction-separation laws.

From a practical perspective, loading large cohesive-length adhesive joints in this manner may cause catastrophic failure in constrained geometries. Therefore, while large cohesive-lengths are beneficial in that it makes joints flaw-insensitive, this may cause sudden, unexpected failure in an engineering application and an appropriate safety factor should be used in design. Furthermore, the results from Chapter 3 extends this result for arbitrary fillet angles and not just cracks. Experimental support of this claim is provided below.

4.4 Numerical example

Despite the complications of the applied shear load, there are methods of accounting for its effects. The two that will be considered here involve using the J-integral and a partial-model. The J-integral method requires a small enough cohesive-length such that the displacements are negligible across the interface for a valid contour integral. The partial-model method, on the other hand, allows for non-zero displacements across an interface. Both require the use of full-field measurement techniques as displacements need to be extracted, and possibly rotations and curvatures as well.

It should be noted that Ruybalid *et. al.* [101, 73] developed a similar method for analyzing geometries in a constrained field-of-view. The method detailed below was developed independently, and is based off one of the findings in Chapter 2: when dealing with beam-like geometries, it is best to treat displacements along vertical lines as a combination of a rotation and extension. The partial model idea works in a manner similar to when one takes

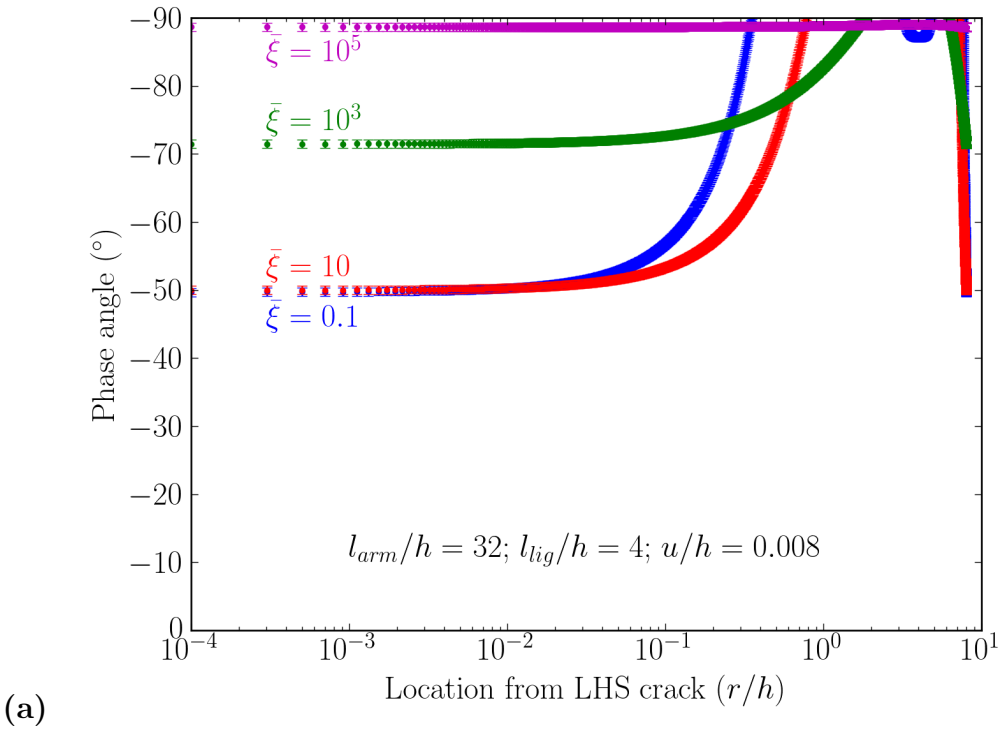

(a)

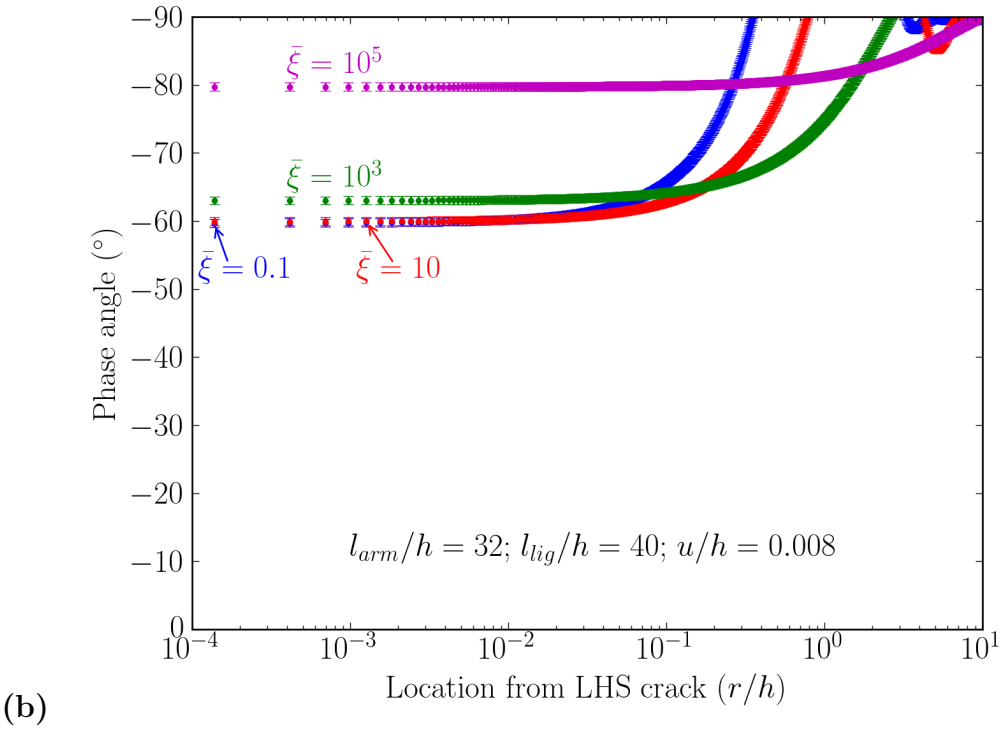

(b)

Figure 4.4: Crack-tip phase angle asymptotes for two different ligament lengths as a function of cohesive-length scale. In **(a)**, the bonded ligament is $l_{lig}/h = 4$ while in **(b)** the bonded ligament is $l_{lig}/h = 40$. One observes that the increase in cohesive-length scale always increases the phase angle in a lap-shear joint with a constrained ligament length, regardless of that length.

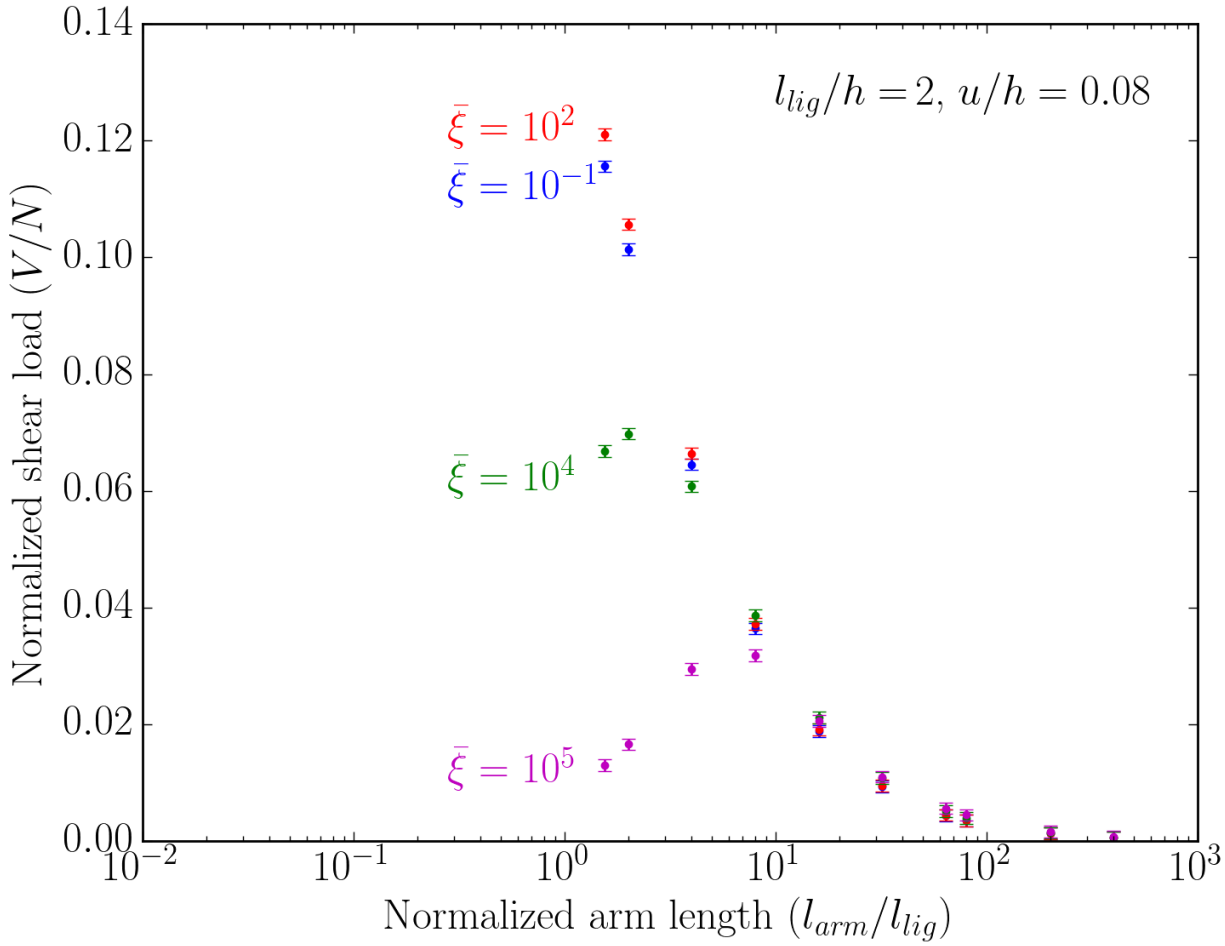

Figure 4.5: In a constrained geometry the cohesive-length scale, and therefore the shape of the traction-separation law, can also change the unknown shear load in the single lap-shear joint. The horizontal displacement is normalized instead of the axial load, because the magnitude of the axial load is also affected by the cohesive-length scale.

a "cut" in a free-body diagram: when one cuts away a portion of the specimen, the appropriate axial load, shear load, and bending moment (for planar calculations) must be added to ensure force and moment balance. From variational mechanics, one typyically uses either Neumann (*e.g.* load, moment) or Dirichlet (*e.g.* displacement, rotation) boundary conditions. The author suggests the use of displacement over load boundary conditions, as displacement data are the direct output from 2-D (*i.e.* surface) full-field measurements. Although not considered here, this same method could be expanded for use in 3-D imaging techniques like digital volume correlation.

Both methods will be used to analyze a numerical example below. An engineering diagram may be found at the top of Figure 4.7, and the lap-shear joint has the following geometric specifications: $a/h = 3$, $l_{arm}/h = 16$, $l_{lig}/h = 8$, and $l_{tab}/h = 4$. Linear traction-separation laws are used so that the cohesive-length scales remain constant.

4.4.1 Large-deformation J-integral

Fernlund *et. al.* [90] derived a large-deformation J-integral that takes into account an applied shear load. For the single lap-shear joint with loads defined in Figure 4.1d and negligible interface thickness, their expression reduces to:

$$J = \frac{N^2}{4\bar{E}h} + \frac{M_1^2}{\bar{E}h^3}\left(6 - \frac{3M_2^2}{4M_1^2}\right) + \frac{N}{2}(\theta_1^2 - \theta_2^2) + V(-\theta_1 + \theta_2), \tag{4.3}$$

where θ_1 and θ_2 defined as the beam rotation where the loads are applied along the centroidal axes of the beam sections. Note that the bending moments are those values at the crack-tip, and therefore any motion of the beams that would change the moment-arm of the axial load or shear load needs to be taken into account.

Now, one just needs to accurately measure the different components of the general loading. Assuming the axial load is known from a load cell, above it was mentioned that one could extract the two bending moments by using full-field measurement data to determine the curvature of the beams, and then the bending moments. From there, one simply needs to use moment balance to extract the shear load as a function along the free arm, an example of which is shown in Figure 4.6a. Assuming one finds a constant shear load, one may be relatively confident the value is correct.

These load values can then be plugged into the J-integral, Equation (4.3), and a similar plot of J along the free arm can be plotted. The significance of the data in Figure 4.6b suggests that one could perhaps extract useful displacement, rotation, and curvature data for the J-integral about $1h$ away from discontinuities. Therefore, if a geometry behaves like a beam, this analysis is worthwhile. Curiously, these findings suggest slightly less stringent

requirements than St. Venant's principle [102].

It should be emphasized that if one chooses this approach, one should have a sharp crack present in the lap-shear joint. The presence of a sharp crack is merely practical: DIC (or other full-field imaging techniques) correlate with greater confidence at sharp cracks rather than corners because one is far from an edge. Therefore, while one may be able to extrapolate the corner displacements from the interface results, the most accurate method would involve using a crack with a large enough length such that the displacements may be properly correlated.

The benefit to using this J-integral approach is that it allows one to extract the mode-II traction-separation law directly, similar to the way the mode-I law was extracted from the symmetric double-cantilever beam in Chapter 2. For the lap-shear joint, one must assume mixed-mode loading at a crack-tip in general, and therefore

$$J = J_I + J_{II}, \tag{4.4}$$

where J_I and J_{II} are the mode-I and mode-II components of J, respectively. From there, if one knows the mode-I law, then one can subtract off the mode-I component and be left with the mode-II component, J_{II}. Then, one can differentiate the mode-II crack-tip work by the shear displacements at the crack-tip, $\delta_{II,\circ}$,

$$\tau(\delta_{II,\circ}) = \frac{J_{II}}{\delta_{II,\circ}}, \tag{4.5}$$

to get the initial portion of the mode-II traction-separation law, τ. Only the intial portion of the law will be known due to mixed-mode failure, and the mode-II toughness, Γ_{II}, will need to be estimated using a failure criterion. However, this is a direct method of extracting the mode-II traction-separation law.

4.4.2 Partial model

Unfortunately, not all systems are brittle enough to allow the use of the J-integral. If the displacements do not approach zero along an interface (both the normal and shear displacements for planar problems), then there is no guarantee the J-integral will give the crack-tip work. Therefore, one must turn to a different method to extract the mode-II traction-separation law. If one still intends to analyze the lap-shear joint, the author suggests using the partial-model approach. The same model is used as in the previous section, but this time the slope of the traction-separation laws is decreased such that $\bar{\xi} = 10$, which results in non-zero shear displacements along the full length of the interface.

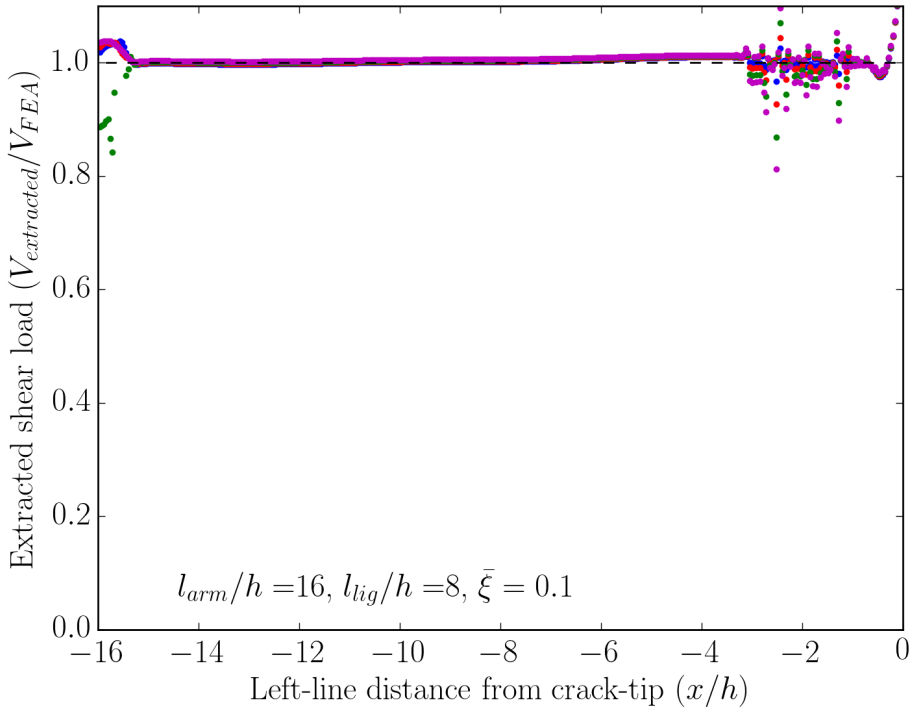

(a)

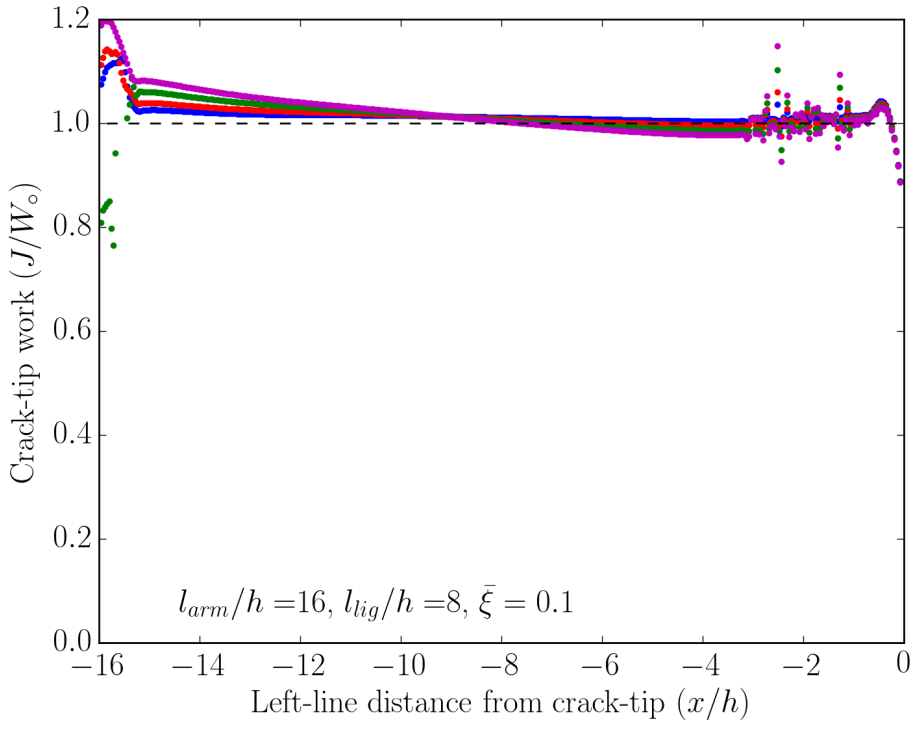

(b)

Figure 4.6: Measurement of the reactionary shear load V and crack-tip work $W_\circ$ using full-field data and axial load from a "load cell". As mentioned before, treating the digital data as analog allows one to remove obvious numerical artifacts. As such, the results above suggest one may use this method to extract the unknown shear load and J-integral within about h of any edge, such as a crack or a clamped boundary. The data presented above are for four different load values: $N/\bar{E}h = 0.000148, 0.000299, 0.000529$, and 0.000762.

After the full calculation was complete, displacement data is exported (the same as one would do for an experiment using DIC). One can then take two vertical planes of displacements (one to the left of a crack-tip and the other to the right of a crack-tip), and implement these displacement boundary conditions in a separate (partial) lap-shear calculation, as shown in Figure 4.7. In comparing the calculations in Figure 4.8, it was found the average difference between the two calculations for the displacment results was less than 1% for the shear displacement and less than 2% for the normal displacements. It should be noted that the average percent error in the normal displacements is significantly increased if there is a change from tension to compression (as is the case here).

When implementing the displacement boundary conditions, it is important to "tie" the edge displacement conditions so that the beam deforms as one would expect from beam theory ("plane sections remain plane"). In Refs. [101] and [73], displacements were prescibed at multiple points along the center of the beams were enforced to provide "DIC" boundary conditions. In the calculations performed here, two points on a vertical plane were given prescribed displacements, and then ties were used to ensure the entire plane moved/rotated as one unit. As seen in Figure 4.8, this was found to be satisfactory. Although not included in the comparison above, the reaction forces between the full-model and partial-model in this instance differed by less than 0.6%.

Experimentally, one must balance the desired displacement resolution with the ability to observe as much of the specimen as possible. Therefore, if one is trying to measure/predict the cohesive-zone displacements, the field-of-view should be no larger than what allows for an acceptable displacement resolution. Of course, the closer the partial model is to the full model, the closer the stress distributions along the arms should be, and the better the agreement will be between the two partial model and the full model. This was observed in other numerical examples which are not included here.

If one is simply trying to validate previously-determined traction-separation laws, and the new geometry of choice is the lap-shear joint, the method is rather straightforward. One must measure the constitutive properties of the adherends, and then use a full-field measurement techinque to implement the displacement and rotation boundary conditions, along with the appropriate measure of uncertainty. An additional benefit is that one need not worry about extracting the beam rotations and curvatures to extract the shear load. The task is more challenging if one is trying to extract the mode-II traction-separation law, but one method of accomplishing this is presented in the next section.

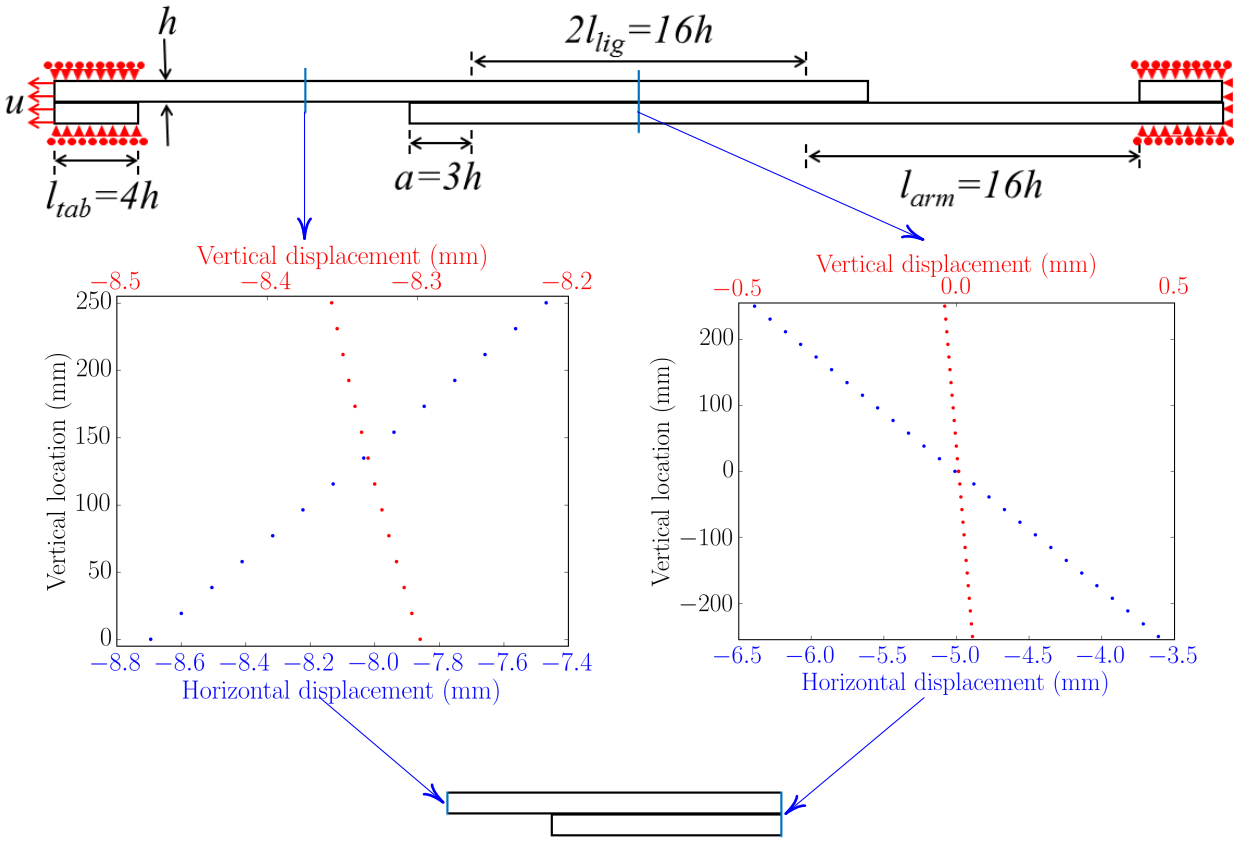

Figure 4.7: Method for using displacement boundary conditions. Using DIC (or any other full-field measurement technique), one can extract displacements along two vertical lines of data from the analysis. One can make a partial model of the specimen, and then implement those displacements as boundary conditions in the numerical model. Provided one knows the constitutive properties of the adherends, the applied axial load, shear load, and bending moment will be applied. However, the *identical* stress distribution will not be implemented, and therefore one should implement the displacement boundary conditions as far from the edges as possible to minimize these effects. For the displacements given above, the load is $N/\bar{E}h = 0.00074$.

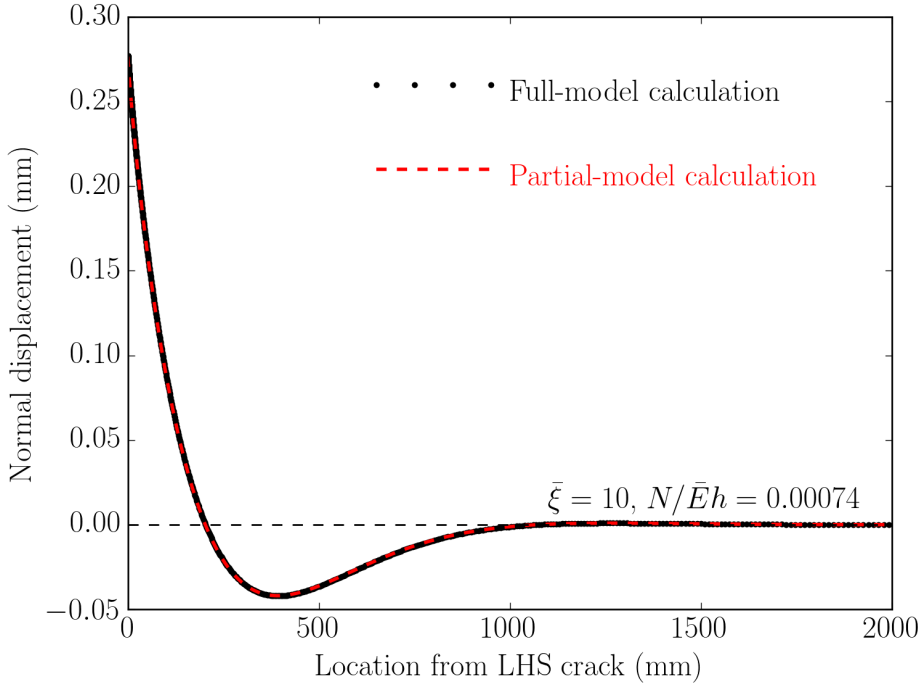

(a)

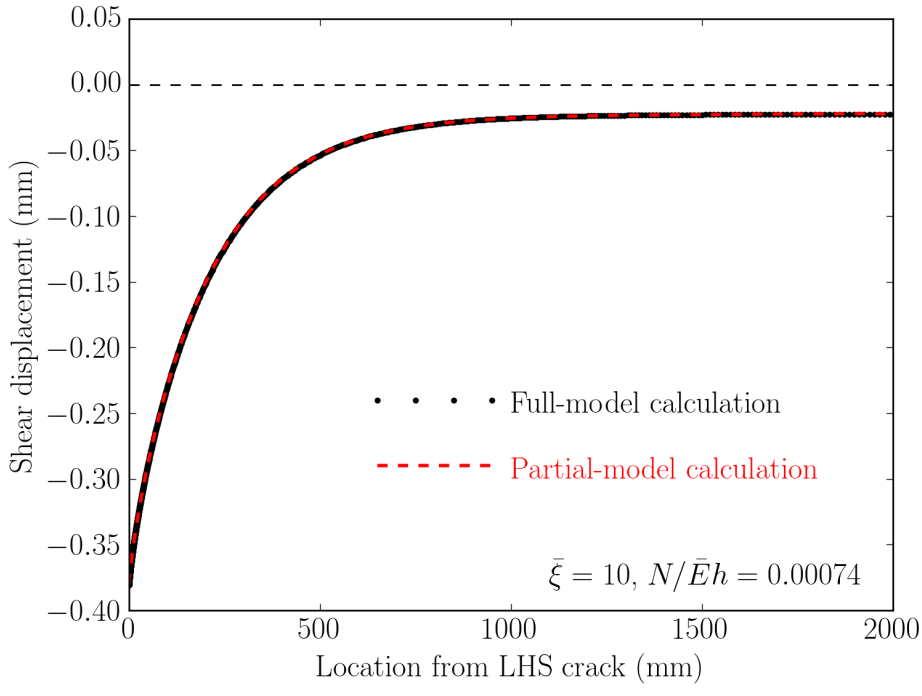

(b)

Figure 4.8: Comparison of the displacement output of the original full-model lap-shear joint calculation and the subsequent partial-model lap-shear joint where displacement boundary conditions were extracted from the full model. Therefore, provided one knows the constitutive properties, boundary conditions, and traction-separation laws, the two results are nearly indistinguishable.

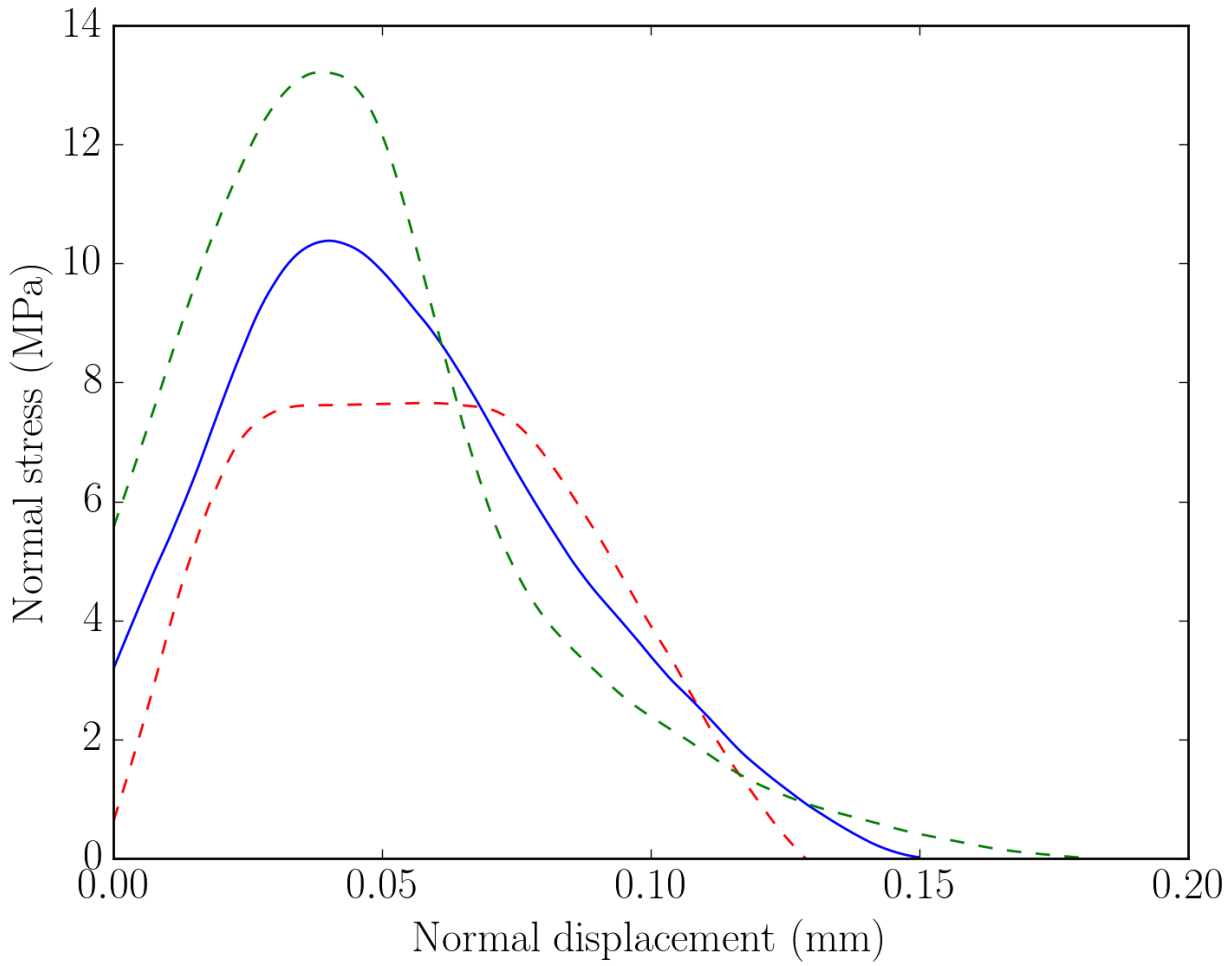

Figure 4.9: Example mode-I traction-separation laws with a characteristic range of strength and toughness values for the adhesive used in this study. The same adhesive (Dow Betamate® 73326M/73327M) from Chapter 2 was used, and this spread of values was determined using the method presented there.

4.5 Experimental validation

Having laid the appropriate groundwork above, one may now proceed to experimental validation. The adhesive considered is Dow Betamate® 73326M/73327M, the same one tested in Chapter 2. While the specifics of only one test were considered there, multiple samples were run on the symmetric steel DCB system. From that testing, a characteristic range of mode-I traction-separation laws determined from these previous tests can be found in Figure 4.9.

It should be noted that in post-mortem analysis, there were some small patches of darker adhesive that may have been unmixed portions of one of the components or due to voids. These small portions may have resulted in increased variability in the adhesive properties

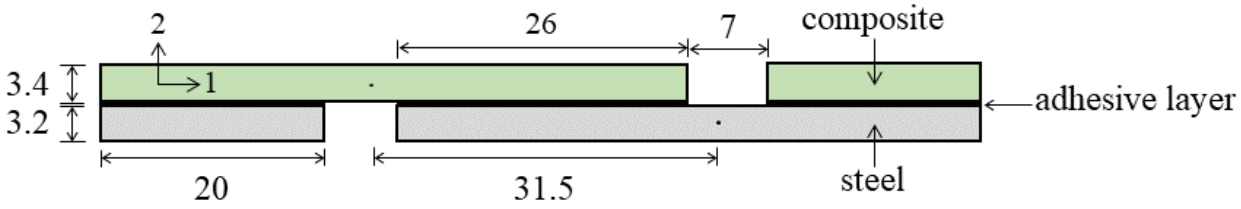

Figure 4.10: Engineering diagram of the composite-steel lap-shear joint analyzed in this chapter. All dimensions are in millimeters. The fibers in the composite are aligned in the 1 and 3 (out of the page) directions.

(approximately 10-15% variation in the peak strength and toughness). Furthermore, no residual stress analysis was performed. These shortcomings might have increased the variability in the adhesive. However, because the testing was performed at approximately the same curing time ($\sim$ 10 days after mixing) and clamping method (binder clips), any residual stress effects were expected to be similar. As explained below, the same adhesive mixing and curing methodology was performed in the following testing.

From the analysis done in Chapter 2 for this system, one knows that the adhesive has a large (mode-I) cohesive-length. This suggests the large-deformation J-integral approach will not be valid because the cohesive-zone displacements do not go to zero, and this will be shown to be the case below. Therefore, the numerical partial-model method will be used to extract the mode-II traction-separation law.

4.5.1 Experimental methods

The validation of the single lap-shear joint partial model will take place on a composite-steel joint, and the engineering diagram of the specimen is given in Figure 4.10. The complications due to fracture along a dissimilar-material interface will be considered in Chapter 5. For now, the focus will be on how one analyzes the single lap-shear geometry using full-field measurement techinques.

When one uses numerical models, one needs to make sure the material constitutive properties are accurate. As mentioned in Chapter 2, a tensile test was run on the 4130 steel used had an elastic modulus of 204 ± 8 GPa and Poisson's ratio of $\nu = 0.32 \pm 0.07$, and had a yeild strength of 340 MPa [75]. The G-10 Garolite composite's material properties were measured to be: $E_{11} = E_{33} = 24.5 \pm 2.0$ GPa, $E_{22} = 11.8 \pm 0.9$ GPa, $\nu_{12} = 0.44 \pm 0.21$, $\nu_{13} = 0.15 \pm 0.11$, $\nu_{23} = 0.23 \pm 0.10$, $G_{12} = G_{23} = 3.7 \pm 0.6$ GPa, and $G_{13} = 4.8 \pm 0.2$ GPa. Post-mortem inspection of the specimen showed no inelastic deformation on the composite, and therefore only the elastic constants were determined. A plane-stress assumption was used for all calculations [3, 16]. The fibers in the composite are in the horizontal direction

and through the thickness.

The composite beams were measured to have a thickness of 3.37 ± 0.02 mm, while the steel beams had a thickness of 3.15 ± 0.01 mm thickness. Beams of each material were cut to a length of approximately 53 mm, and then milled to a width of 25.9 mm. The bonding surfaces of each beam were polished to a level of 100 grit, after which a layer of the two-part epoxy (Dow Betamate® 73326M/73327M) was applied to the surface of the composite beam. Glass spheres of 250 micron diamter were sprinkled onto the adhesive layer to ensure uniform thickness. The steel beam was then placed on top and then aligned. The specimen was clamped using binder clips for two days. Afterwards, the clips were removed and the adhesive was allowed to cure for another week. The excess, extruded adhesive was removed, and optical observations determined the adhesive thickness to be 260 ± 20 microns. Complementary beam sections of each adherend were bonded to the lap-shear joint (as shown in Figure 4.10) to ensure there was no rotation of the lap-shear joint within the wedge grips used for testing.

The side of the lap-shear joint was polished using 100-grit sandpaper followed by 600-grit sandpaper. A white basecoat was then applied, followed by a black speckle pattern using an Iwata™ CM-B airbrush. Testing was performed within one day of applying the speckle pattern. Mechanical testing was performed using a servo-hydraulic test machine (MTS 858 MiniBionix II™), and the nominal cross-head displacement rate was 0.17 mm/min. For DIC analysis, a single 5-megapixel Grasshopper™ camera was used to record images at a frame rate of 2 Hz. In the images, a pixel had a width of approximately 17 microns. The commercial software Vic-2D™ was used for local, subset-based DIC analysis. A subset-size of 27 and step-size of 3 were used for the analysis. As mentioned in Chapter 2 when analyzing the double-cantilever beam specimen, the single lap-shear joint is a bonded geometry made up of two beams. As such, deformation along the beams will be treated as in an Euler-Bernoulli beam where plane sections remain plane. This approach once again proved to be useful in removing numerical artifacts.

For a nice geometry like the symmetric double-cantilever beam under elastic deformation, there exist multiple ways to extract the mode-I traction-separation law [70, 71, 43, 44, 72, 73, 74]. In geometries that are not as analytically robust, such as the T-peel or edge-notched flexure specimens, comparisons are often made to load-displacement curves to determine or validate traction-separation laws [2, 23, 103, 21, 42, 104, 16]. Therefore, the mode-II traction-separation law will be determined by using the appropriate numerical-partial models and fitting the results from the numerical load versus centroidal-axis displacement data to the experimental results. The comparison of full-field measurements (*e.g.* normal and shear cohesive-zone displacements) with the numerical predictions was made only *after* the mode-

II traction-separation law was found by fitting numerical results to the load-displacement curve.

Figure 4.11 shows the load versus centroidal-axis displacement curve, where the centroidal-axis displacement is defined as the extension of the line between two points located 31.5 mm apart and specified in Figure 4.10. Load points "A" through "E"[2] will be considered in more detail during the analysis of this geometry. The extension of this line-segment was used in order to ignore the effects of rigid-body rotation, which will later be shown to be important for the agreement between the experimentally-measured and numerically-predicted cohesive-zone displacements. Inscribed on the plot are five points that will be considered more-fully throughout the analysis, along with the estimated mode-II cohesive-length scale $\bar{\xi}_{II}$ at each point.[3] The lap-shear joint failed catastrophically instead of through stable crack-propagation.

An image of the specimen is shown in Figure 4.12. The two locations of the boundary conditions are shown, which will be necessary for the implementation of the numerical partial-model. The five lines along the interface that will be considered when analyzing the interface displacements.

Before comparing the experimental results with the numerical calculations, one first needs to accurately extract the boundary conditions. From Figure 4.12, boundary conditions along the two specified lines are extracted during the entire loading. Example horizontal displacment boundary conditions are shown in Figure 4.13 for the five points specified in Figure 4.11. Close observation of the extracted displacements show a fine structure, which is likely the result of the DIC interpolation functions. It should be noted that if one simply used standard DIC rotation output from the commercial software, it might appear that there exist non-uniform rotations within the beams. This ought to be avoided, however, because one can see that the beam really is deforming in a uniform fashion (as one would expect from beam theory) if one looks at the data as a whole instead of only at discrete points.

Boundary conditions are implemented in the partial-models by specifying displacement pairs at two points on each edge, and then forcing the entire edge to move in a uniform fashion (using a "tie" constraint in Abaqus). Affine fits (shown in Figure 4.13), are used to determine the displacements implemented in the numerical calculations (including a reasonable amount of experimental uncertainty). The points at which the displacement boundary conditions are

[2]These load points are independent from load points "A" through "E" defined in Chapter 2.

[3]The composite elastic modulus [27], $\bar{E}^* = 43.7$ GPa, was determined using the fiber-direction elastic modulus $E_{11} = 24.5$ GPa and the steel elastic modulus of 204 GPa. The left-hand side corner displacement, as defined in Figure 4.10, was the largest (shear) displacement and was used to determine the (mode-II) work done at the singularity using the traction-separation law in Figure 4.14b. The characteristic length was taken to be the smaller beam thickness of 3.15 mm. This value is an estimate, however, because DIC correlation limitations did not allow displacements to be taken precisely at the corner.

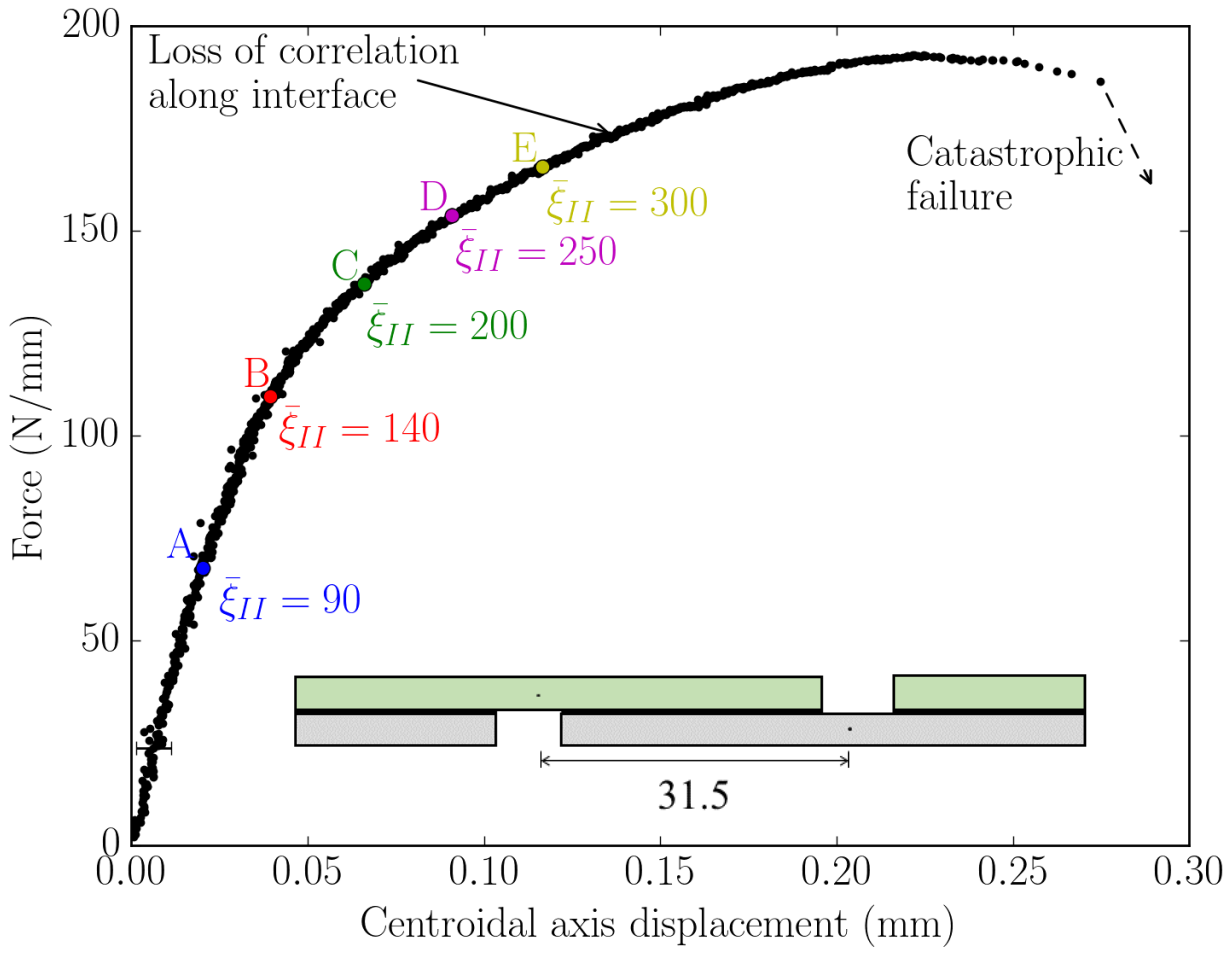

Figure 4.11: Load vs. centroidal-axis displacement plot of the composite-steel lap-shear joint analyzed here. The centroidal-axis displacement is defined as the extension of the line connecting the two dots in the engineering diagram, which has been inscribed on the plot for convenience. The estimated mode-II cohesive-length scales inscribed on the plot are generated using the left-hand side corner displacement, the work generated using the mode-II traction-separation law in Figure 4.14b, and the reduced modulus $\bar{E}^* = 43.7$ GPa [27], assuming the composite's elastic modulus is 24.5 GPa and steel's elastic modulus is 204 GPa. As the steel beam was slightly thinner than the composite beam, the smaller thickness was taken to be the characteristic length.

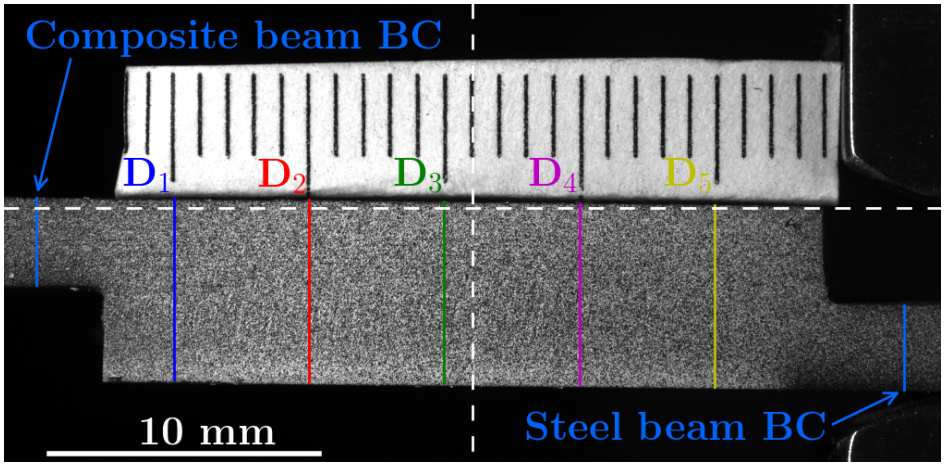

Figure 4.12: Image of the composite-steel lap-shear joint with the origin used for all analyses. Inscribed on the image are the locations of the two points where boundary conditions are measured in order to be implemented in the numerical model; note that the boundary condition lines are located at the two points from which the centroidal-axis displacement is measured, as noted in Figure 4.10. Five characteristic lines along the interface are also specified when analyzing the cohesive-zone displacements.

applied are located at the top and bottom of the vertical lines of data shown, approximately 0.3 mm from the top or bottom edge of each beam.

Having all the necessary components, it is now time to use the different parts in order to back out the mode-II traction-separation law. As explained in Section 4.4.2, a numerical partial-model was made matching the lap-shear specimen's dimensions, including the locations of the applied boundary conditions. The entire adhesive layer was replaced by cohesive elements, with a range of mode-I traction-separation laws characterized by Figure 4.9. It was assumed that the compressive mode-I law from Chapter 2 adequately described the adhesive layer, and the reader will see below this appears to be valid. Many numerical calculations were run along the full length of the experimental curve in Figure 4.14a. Note that only the mode-II traction-separation law was varied in the numerical calculations. The numerical predictions are presented by the hatched data, and one sees good agreement between the numerical results and the experimental data. The experimental-numerical agreement appeared only to be limited by how well one can approximate a curve by a 6-part piecewise-linear function. The extracted mode-II law is in Figure 4.14b. The peak strength was found to be 7.4 MPa and the mode-II toughness was 1800 ± 50 J/m^2. The uncertainty in the toughness is due to the range of mode-I traction-separation laws.

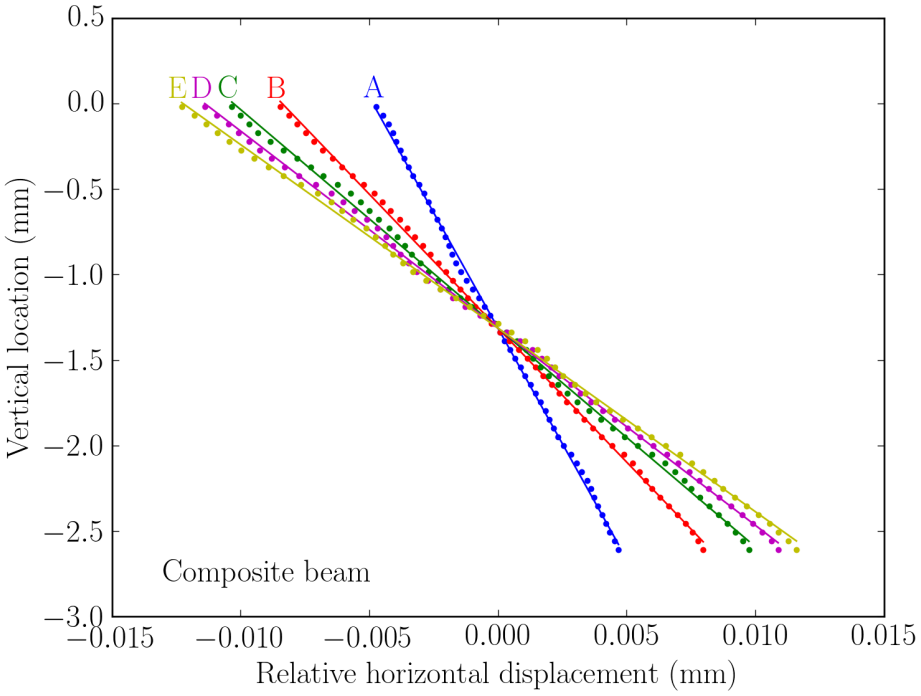

(a)

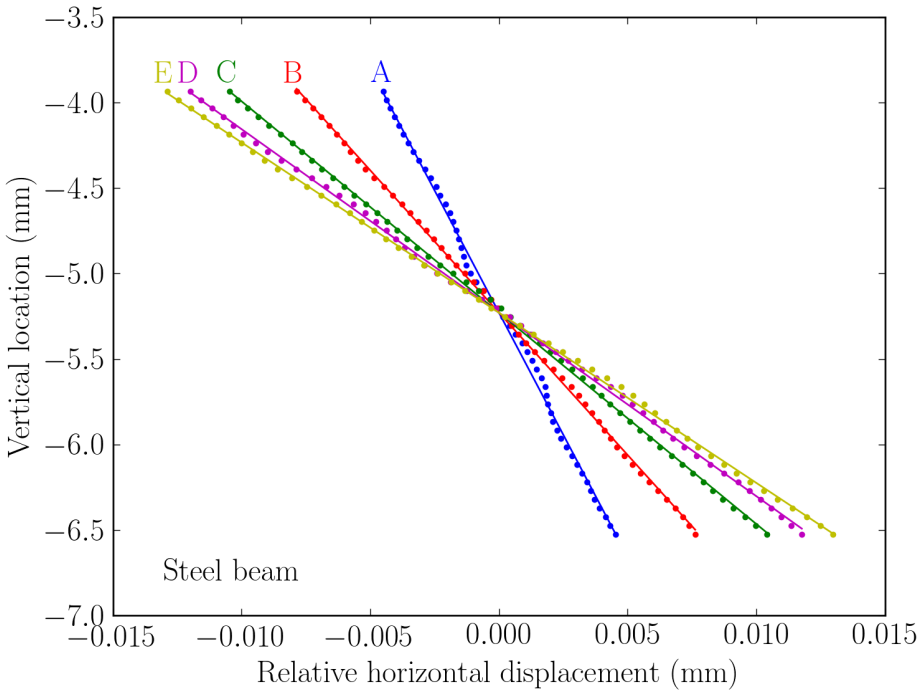

(b)

Figure 4.13: The relative horizontal displacements applied at the **(a)** composite and **(b)** steel beam boundary conditions for the five data points specified in Figure 4.11. Similar plots could be generated for the vertical displacements. The locations of where the displacement boundary conditions are extracted is shown in Figure 4.12. The affine fits for each line allow the reader to observe the fine structure in displacements which appear to be from the interpolation functions used by DIC.

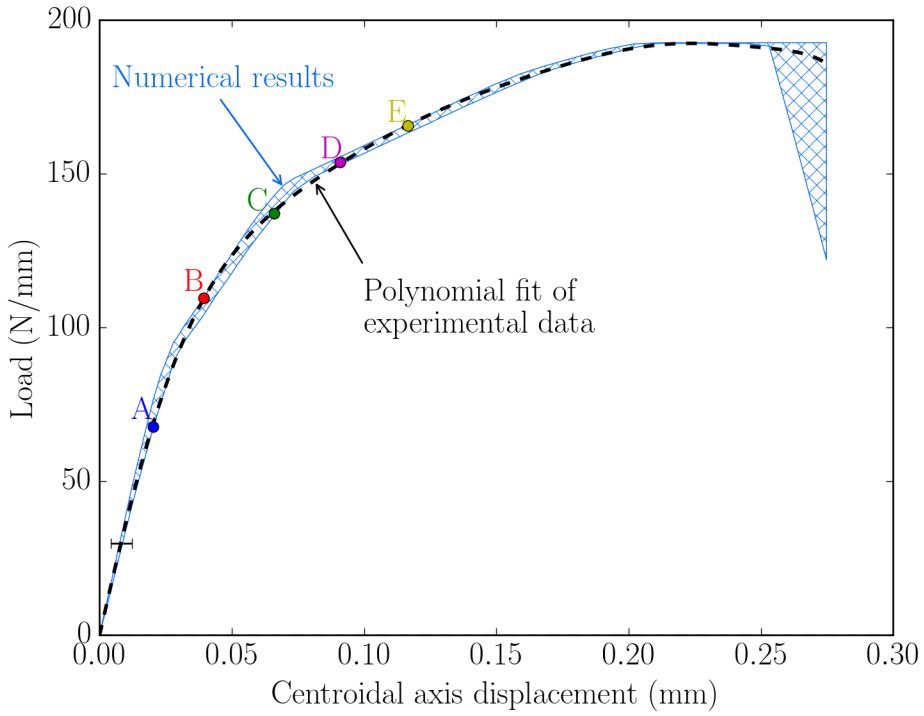

(a)

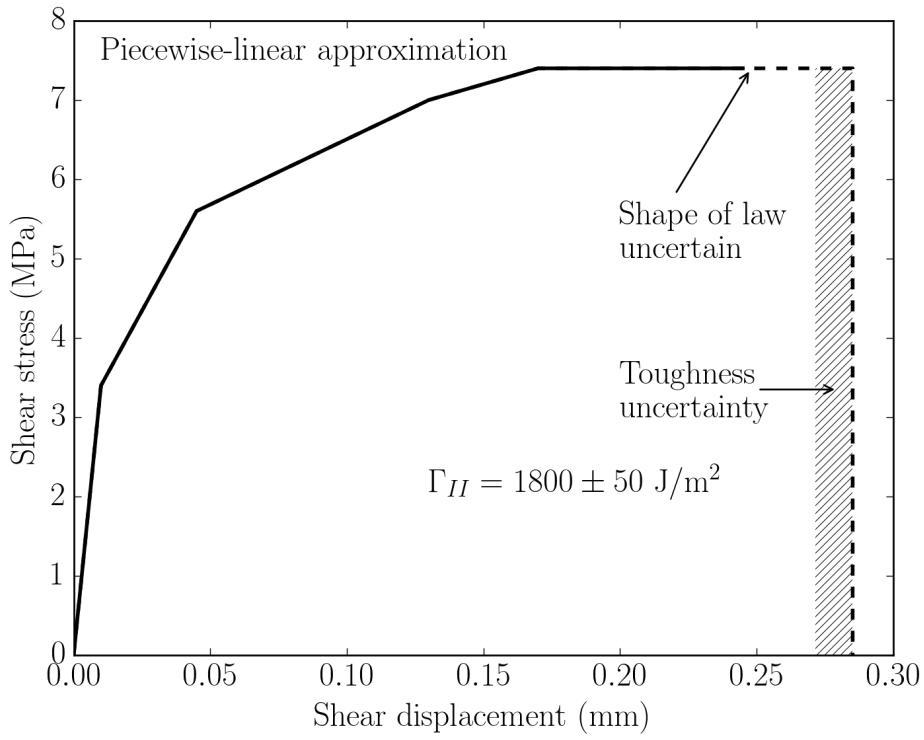

(b)

Figure 4.14: Using the load vs. centroidal-axis displacement plot in **(a)**, one can modify **(b)** the mode-II traction-separation law to get optimal numerical-experimental agreement. Only the mode-II cohesive law was varied to determine this agreement. One sees the piecewise-linear law adequately reproduces the experimental results, although near the end there exists a large uncertainty. This uncertainty is due to the mode-I traction-separation laws.

4.5.2 Quantitative replication

Having extracted the mode-II traction-separation law from the macroscopic deformation, it is now time to validate the law. Previously, one would be forced to measure the mode-I/-II laws separately, and then consider a separate system to validate the measured laws. One would also need to run enough tests so the range of values is statistically valid. However, the use of full-field deformation techniques allows one to separately measure and validate a traction-separation law on the same specimen, as was done in Chapter 2 for the DCB.

The first validation to be done is the comparison of the beam rotations. Simplistically, each numerical calculation is a boundary-value problem, and if the beam rotations do not match one would not expect the cohesive-zone displacements to match either. One can see in Figure 4.15 there is good agreement between the numerical predictions and experimental results. In both the composite and steel beams, the numerical predictions reproduce the shape of rotation curves.

While it is necessary to find good beam rotation agreement, the comparison of interest using the cohesive-zone model is the interface displacements. In Figure 4.12, five lines were marked, and the horizontal displacements for those lines at load-point "D" are found in Figure 4.16. These data are the raw displacement data from the DIC output and have not been corrected for rigid-body rotation.

Just like in the DCB results, one sees two slope discontinuities in each line corresponding to the transition between adherend and adhesive and adhesive to adherend. There was also a slight misalignment (less than 1°) between the camera and specimen, and this needed to be accounted for as well when calculating the cohesive-zone displacements. The use of subset-based DIC means that the sharp transition between adhesive and adherend is smoothed out: the adhesive layer was optically determined to be 260 ± 20 microns, while the interface region is larger than 600 microns. This requires that the displacements be measured within the adherends just outside of the data smoothing.

As with the symmetric DCB specimen, the adherends are substantially stiffer than the adhesive[4] and so the deformation is concentrated within the adhesive layer rather than the two adherends. It is therefore assumed that the deformation occurring within the adherends is negligible compared to the adhesive layer.

While the rigid-body rotation corrections were negligle for the normal displacements in the symmetric DCB, here they cannot be ignored because the beam rotations are larger and one needs to worry about the interfacial shear displacements. Therefore, the rotation-

[4]The adhesive is quoted [77] to have an elastic modulus of 870 MPa. The G-10 Garolite is over 20 times stiffer than that in the fiber direction, and the steel is two orders of magnitude stiffer.

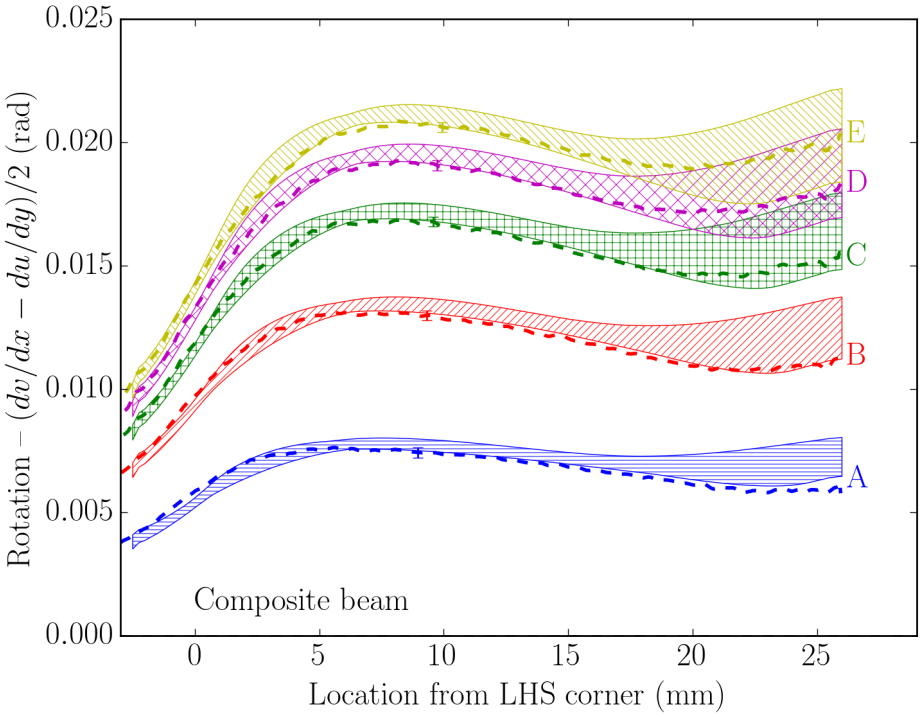

(a)

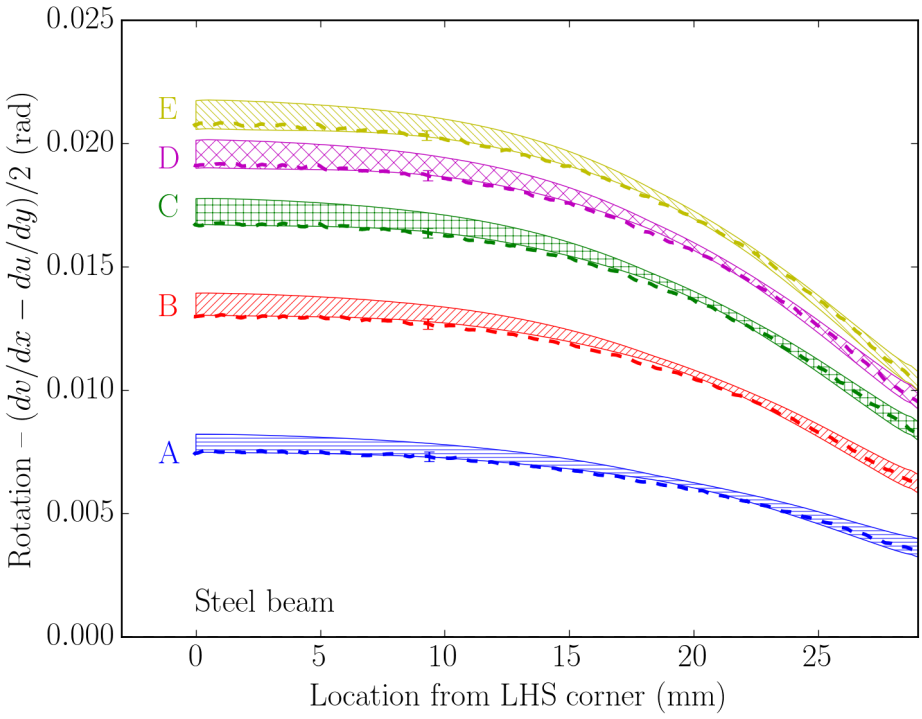

(b)

Figure 4.15: The beam rotation agreement along the **(a)** composite and **(b)** steel beams for the five data points specified in Figure 4.11, with the experimental results displayed as dashed lines and numerical predictions in the hatched regions. One sees the numerical calculations satisfactorily reproduce the experimental data, including the shape of the different curves for the composite and steel beams.

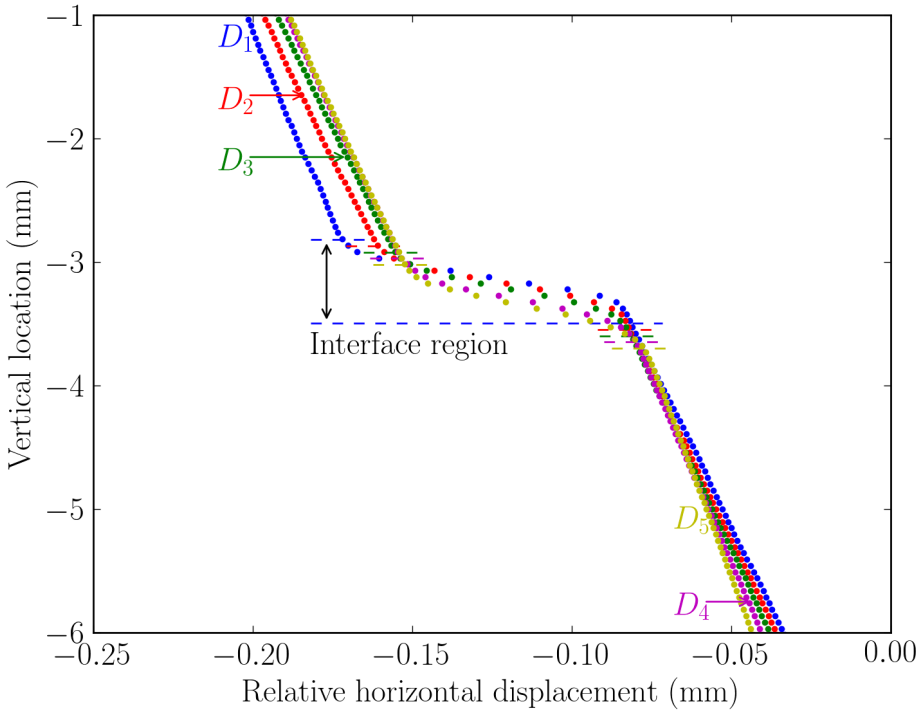

Figure 4.16: Five characteristic lines along the interface, specified in Figure 4.12, have their (relative) horizontal displacements plotted against their vertical location for load point "D". Note that no correction for rigid-body rotations have been applied to this data, only a shift in the horizontal displacements. The transition between the adherends and adhesive layer, the "interface region", is smoothed out due to the use of local, subset-based DIC. This requires displacements be taken outside of the adhesive layer in the adherends, which undergo much less deformation. The rotation of the adherends can be seen in the data, and this must be corrected when calculating the cohesive-zone displacements.

corrected shear displacements are

$$\delta_{II} = \Delta u' cos(\theta) + \Delta v' sin(\theta) + t\, sin(\theta), \tag{4.6}$$

and the rotation-corrected normal displacements are

$$\delta_{I} = -\Delta u' sin(\theta) + \Delta v' cos(\theta) + t\,(1 - cos(\theta)), \tag{4.7}$$

where $\Delta v'$ and $\Delta u'$ are the uncorrected normal and shear displacements across the interface, and t is the thickness of the "interface region" (the distance over which the interface displacements are measured and *not* the adhesive layer). θ is the *average* rotation of the top and bottom beams where the normal/shear displacements are being corrected.

The use of the average rotation of the two beams is nuanced, so additional discussion is warranted. In the lap-shear joint, whether the one analyzed here or other systems, the top and bottom beams will not necessarily have the same beam rotation, even if they are made of the same material. This is especially true when considering large cohesive-lengths. Due to this difference in beam rotation, it *does* matter what rotation value is used because it depends on where one measures the (uncorrected) cohesive-zone displacements. If the top reference point for the cohesive-zone displacements is farther into the adherend than the bottom reference point, then the measurement is more biased towards the top beam's rotation. Therefore, one needs to be aware of this rotation bias when measuring the cohesive-zone displacements.

It is worth noting that the commercial software used will not automatically correct for rigid-body rotations. Furthermore, even if rotations were exported from the DIC software and those were used to make rigid-body rotation corrects, there is no guarantee the rotations would be correct. Recall that it has already been observed standard DIC software differentiates data at discrete points, and this may result in increased noise. Rigid-body rotation correction would also be required for correct strain computation, but that is not a focus of this work.

The DIC software used here has a uniform subset across the entire region of interest. Therefore, the displacement smoothing should be uniform across the specimen and not be biased towards the top or bottom beams. Furthermore, the epoxy is compliant enough such that nearly all the deformation that occurs happens in the adhesive layer rather than in the adherends. Therefore, the displacement smoothing should occur an equal distance within each adherend. Because the cohesive-zone displacements were taken at regions just outside of the displacement smoothing without any bias towards one adherend or the other, the author used the average rotation from the beams.

Having discussed the nuance of the rigid-body rotation correction, one can see the comparison of the experimentally-measured cohesive-zone displacements with the numerical predictions from the cohesive-zone model. Overall, one sees good agreement between the numerical predictions/experimental results in both the normal (Figure 4.17a) and shear (Figure 4.17b) displacements. The numerical predictions do a fair job of reproducing the shape of the experimental curves. The five experimental data points from Figure 4.16 are reproduced on Figure 4.17b, after correcting for rigid-body rotations. Due to the satisfactory agreement found between the numerical predictions and experimentally-measured cohesive-zone displacements, the extracted mode-II cohesive law is considered validated.

Using the traction-separation law from Figure 4.14b, one can use this law along with the accompanying mode-I laws to determine a phase angle. These experimental results are shown in Figure 4.18, with phase angle asymptotes shown from both the LHS and RHS corners, as defined in the engineering diagram (Figure 4.10). The phase angles are predominantly mode-II, which one would expect from the numerical results in Figure 4.4. There is perhaps a bit of a surprise that the phase angle at both corners becomes more mixed-mode with increased loading, instead of shifting towards pure shear. However, one recognizes from the numerical results at the end of Chapter 3 that the phase angle asymptote is dependent on the shape of the traction-separation law. Even though DIC challenges limit correlation as one approaches the corner, this appears to be the first experimental results showing the phase angle plateau at a singularity.

The findings of Ref. [27] demonstrate that the phase angle changes during failure for nonlinear traction-separation laws, and this is experimentally observed here. Ref. [27] showed, at small cohesive-length scales, the second Dundurs parameter[5] $\bar{\beta} = -0.2$ shifted the crack-tip phase angle about 10°. Both corner singularities are far from the stiff, low-load LEFM phase angle value of $-49.1°$. This comparison is skewed, however, because the cohesive-length scales (Figure 4.11) are much larger than when LEFM is usefully valid.

Another difference between the two is the use of a corner instead of crack for the singularity in comparing the phase angles. Comparison of results from Figure 3.11 suggest that the small-CLS phase angle plateaus are smaller (mode-I preference) for the corner, which would result in an even larger phase angle shift between the two results. The observation of two different phase angle plateaus is not unexpected due to specimen asymmetry.

Overall, the numerical/experimental agreement throughout the entire numerical partial-model analysis in the load-displacement curve, beam rotations, and cohesive-zone displacements was satisfactory. The numerical partial-model approach is therefore considered ex-

[5]For the measured composite properties, using $\bar{E}_1 \equiv E_{11}$ and $\nu_1 \equiv \nu_{12}$, the two Dundurs parameters have the values $\bar{\alpha} = -0.79$ and $\bar{\beta} = -0.21$.

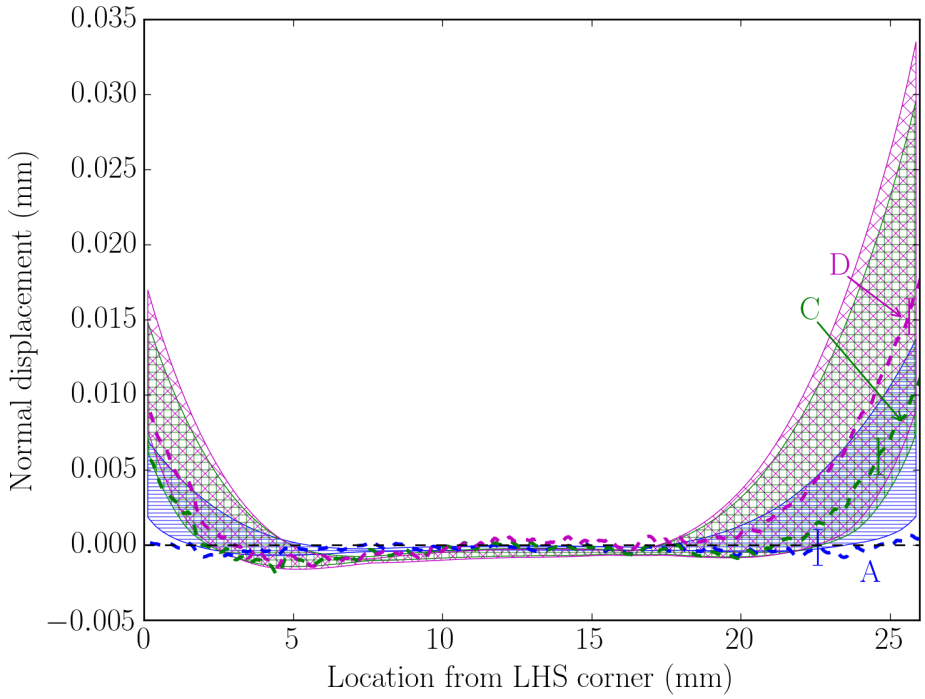

(a)

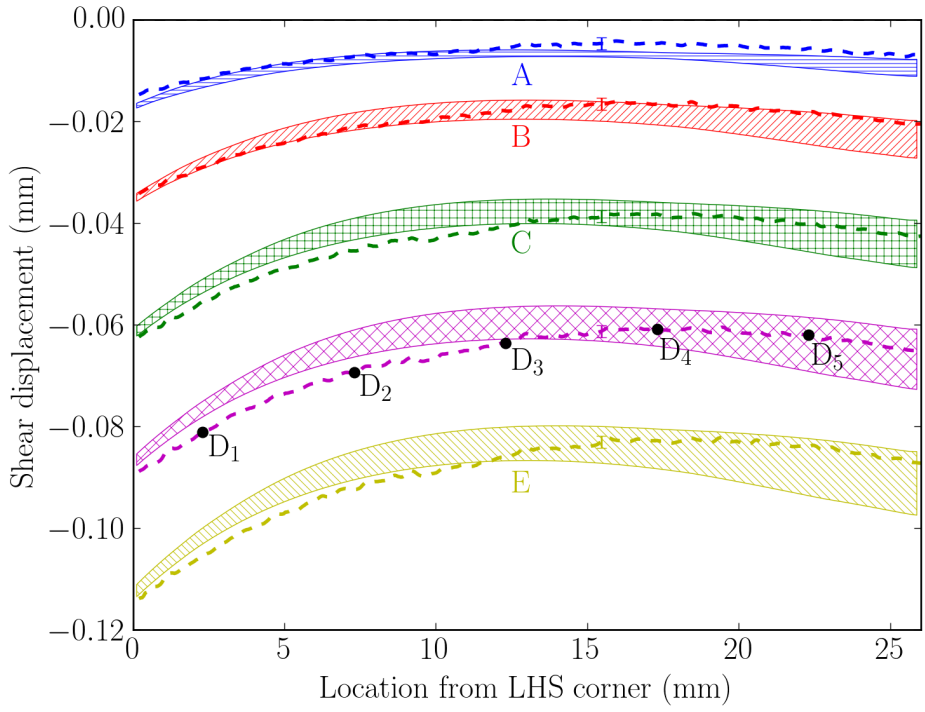

(b)

Figure 4.17: The **(a)** normal and **(b)** shear displacements along the adhesive interface for the five data points specified in Figure 4.11, with the experimental results displayed as dashed lines and numerical predictions in the hatched regions. As with the beam rotations in Figure 4.15, the numerical replication of the interface displacements is satisfactory. Less data was plotted in **(a)** because the normal displacements are so close together.

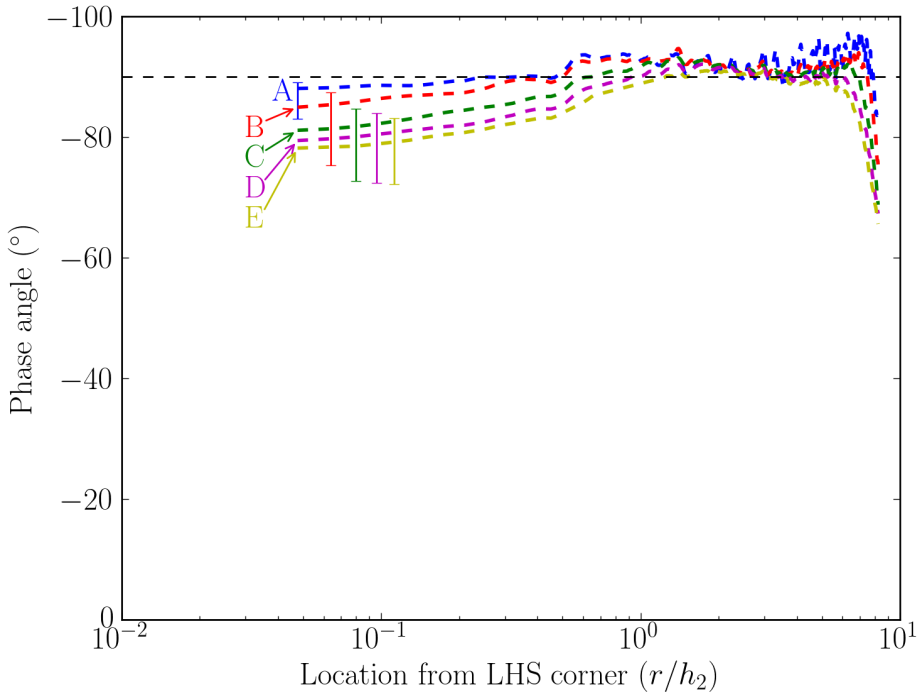

(a)

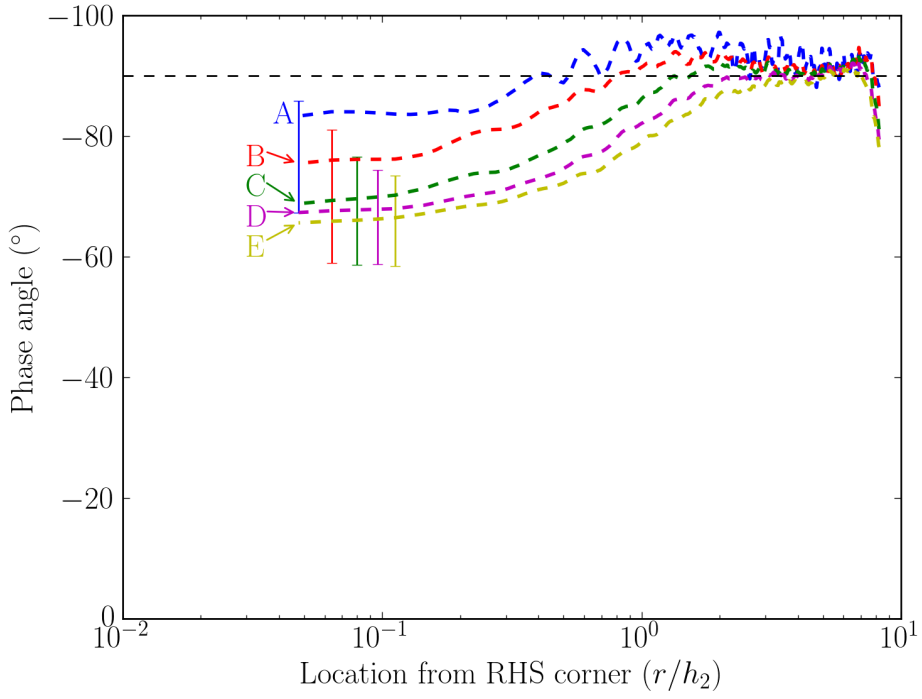

(b)

Figure 4.18: The phase angle measured from the **(a)** left corner and **(b)** right corner. The phase angles were calculated using the range of mode-I traction-separation laws, Figure 4.9, and the mode-II law extracted in Figure 4.14b. The two different phase angle asymptotes are not unexpected, as the two different adherends cause the anti-symmetry of the system to be lost. This appears to be the first experimental results showing the phase angle plateau at a singularity. h_2 is the thickness of the steel adherend.

perimentally validated. Additional experimental analyses could be run to extract a range of mode-II traction-separation laws, but that has yet to be accomplished.

A final word should be stated concerning the use of a continuum model. In Chapter 2, the CZM results were good but the elastic-plastic continuum results were found to be better, as it was able to account for the in-plane tension experienced by the adhesive during loading. Unfortunately, this was only the case in the case of nominally pure mode-I loading. In this case, when one deals with mixed-mode loading the mode-I or mode-II laws cannot simply be converted to a uniaxial-tension stress-strain relation with a von Mises yield criterion assuming J_2-flow theory. The load-displacement curves do not match, nor do the interface displacements. Even when the numerical load-displacement curve was fit to the experimental results, the interface displacements did not match. A continuum model might work if one combined the displacements into a cohesive-zone model formulation where an effective displacement was used [14, 43], but it was beyond the scope of this work to consider that extension.

4.6 Summary

The single lap-shear joint under general loading has been experimentally and numerically explored in this chapter. It was demonstrated that the neglect of the reactionary shear load resulting from "clamped" boundary conditions can result in incorrect crack-tip work values, particularly for stubby-armed lap-shear joints. Furthermore, the relative shear load was shown to be dependent on the geometry. Increasing the cohesive-length scale in a constrained lap-shear joint was shown to push delamination towards pure shear deformation, and can also change the relative shear load for a given geometry.

Two methods were provided for analyzing the single lap-shear joint with an applied shear load: the large-deformation J-integral method and the numerical partial-model method. The former is useful in that one can experimentally measure the J_{II} versus crack-tip shear displacement curve and back out the initial portion of the mode-II law by direct differentiation. However, this method is limited because it requires a small enough cohesive-length such that the interface displacements to go to zero to ensure a valid J-integral. The numerical partial-model approach has no such limitation, but may require a brute-force method to extract the initial portion of the mode-II traction-separation law. Because the single lap-shear joint typically has mixed-mode loading, the downside to both methods is that only the initial portion of the mode-II traction-separation law can be determined and the latter portion (including the shape of the law and the mode-II toughness) must be estimated.

The numerical partial-model approach was experimentally verified. It was shown one

could extract the appropriate boundary conditions from DIC, and these could be implemented in numerical calculations for satisfactory predictions of both the beam rotations and cohesive-zone displacements. To the best of the author's knowledge, this is the first instance of someone using experimentally-determined traction-separation laws to predict cohesive-zone displacements in the lap-shear joint and the first experimental observation of a phase angle plateau at a singularity.

CHAPTER 5

On the Deconvolution of Mixed-Mode Fracture

5.1 Overview

At the end of Chapter 4, the numerical partial-model method was validated on a composite-steel lap-shear joint. Up until now, failure has only been considered along a bonded-interface with the same material on each side. Now, it is time to relax that constraint and consider the effects of fracture along a dissimilar-material interface. This is particularly relevant because adhesives are often chosen for their ability to bond two different materials, and therefore it is important one can accurately predict their failure.

The first analytical work on fracture along a dissimilar-material interface was Williams [105], where he found an oscillatory stress field bounded by a previous elasticity solution [106]. One method around this was the use of an interface with uniform or varying elastic modulus between the bulk adherends to remove this oscillatory field [107]. As another possible fix, Comninou [108, 109] provided some solutions to the problem by allowing crack closing (*i.e.* contact) at crack-tips. Dunders [25] observed that one could reduce the non-dimensional parameters from three to two along a dissimilar-material interface for two isotropic materials. For such a system, as defined in Figure 5.1, the first Dundurs parameter is

$$\bar{\alpha} = \frac{\bar{E}_1 - \bar{E}_2}{\bar{E}_1 + \bar{E}_2}, \tag{5.1}$$

and the second is

$$\bar{\beta} = \frac{\bar{E}_1(1-\nu_2) - \bar{E}_2(1-\nu_1)}{2(\bar{E}_1 + \bar{E}_2)} = \frac{1}{4}(\nu_1 - \nu_2 - \bar{\alpha}(-2 + \nu_1 + \nu_2)), \tag{5.2}$$

where $\bar{E} = E$ in plane stress and $\bar{E} = E/(1-\nu)$ in plane strain, where ν is Poisson's ratio. For the composite-steel system used to validate the numerical partial-model method in Section 4.5, recall that the experimentally-measured G-10 Garolite composite's material

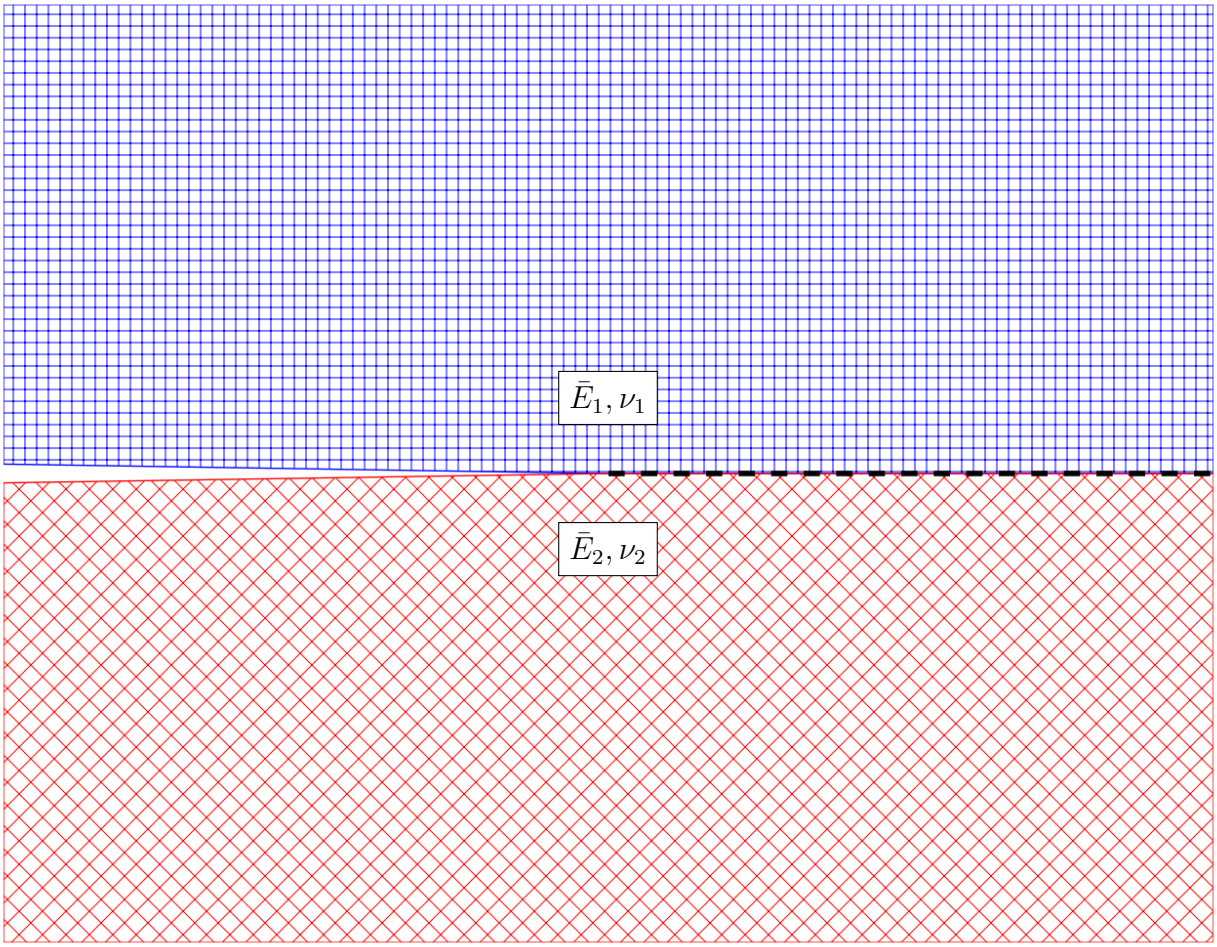

Figure 5.1: A generic bi-material interface made of two isotropic materials with elastic constants $\bar{E}_1$ and ν_1 for the top half, and $\bar{E}_2$ and ν_2 for the bottom half.

properties were $E_{11} = E_{33} = 24.5 \pm 2.0$ GPa, $E_{22} = 11.8 \pm 0.9$ GPa, $\nu_{12} = 0.44 \pm 0.21$, $\nu_{13} = 0.15 \pm 0.11$, $\nu_{23} = 0.23 \pm 0.10$, $G_{12} = G_{23} = 3.7 \pm 0.6$ GPa, and $G_{13} = 4.8 \pm 0.2$ GPa, while the 4130 steel was $\bar{E} = 204 \pm 8$ GPa and $\nu = 0.32 \pm 0.07$. Letting $\bar{E}_1 \equiv E_{11}$ and $\nu_1 \equiv \nu_{12}$, the Dundurs parameters for this system are $\bar{\alpha} = -0.79$ and $\bar{\beta} = -0.21$.

In practice, there is some finite thickness of a transition from one adherend to the other, whether it be an adhesive layer [2, 3] or a weld [21]. This is a reason one uses the cohesive-zone model, and is similar to the elastic solution method presented in Ref. [107]: cohesive failure of an adhesive where the crack travels through an isotropic material, or a material of varying moduli when a crack propagates through a weld. It is within this framework that one sees an additional benefit of CZM: the traction-separation laws govern the interface separation and the oscillitory stress and displacement fields are removed [27]. It was shown in Ref. [27] that a nonzero $\bar{\beta}$ shifted the phase angle from the homogenous-material LEFM

prediction. Their findings also showed that the shape of the traction-separation law can impact the phase angle asymptote as loading evolves, which was experimentally observed in Chapter 4.

Although the cohesive-zone model does not have to worry about oscillatory singular fields, it has its own challenges. In private communication, under the assumption of potential-based [110] traction-separation laws Thouless [111] demonstrated for mixed-mode loading that, generally, one can only measure the mode-I (mode-II) law if the mode-II (mode-I) law is known. Using the J-integral, this leads to[1]

$$\sigma(\delta_I^*, \delta_{II}^*) = \frac{dJ}{d\delta_{I,\circ}}|_{\delta_{I,\circ}=\delta_I^*;\delta_{II,\circ}=\delta_{II}^*} - \tau(\delta_I^*, \delta_{II}^*)\frac{d\delta_{II,\circ}}{d\delta_{I,\circ}}|_{\delta_{I,\circ}=\delta_I^*;\delta_{II,\circ}=\delta_{II}^*}, \tag{5.3}$$

and

$$\tau(\delta_I^*, \delta_{II}^*) = \frac{dJ}{d\delta_{II,\circ}}|_{\delta_{I,\circ}=\delta_I^*;\delta_{II,\circ}=\delta_{II}^*} - \sigma(\delta_I^*, \delta_{II}^*)\frac{d\delta_{I,\circ}}{d\delta_{II,\circ}}|_{\delta_{I,\circ}=\delta_I^*;\delta_{II,\circ}=\delta_{II}^*}, \tag{5.4}$$

Where δ_I^* and δ_{II}^* are the particular normal and shear crack-tip displacements of interest, respectively. Equations 5.3 and 5.4 can be reformulated into the matrix-vector system of the form $\underline{\underline{A}}\,\underline{x} = \underline{b}$, and by dropping where the values are evaluated this becomes:

$$\begin{pmatrix} 1 & \delta_{II,\circ}/\delta_{I,\circ} \\ \delta_{I,\circ}/\delta_{II,\circ} & 1 \end{pmatrix} \begin{pmatrix} \sigma \\ \tau \end{pmatrix} = \begin{pmatrix} dJ/d\delta_{I,\circ} \\ dJ/d\delta_{II,\circ} \end{pmatrix}. \tag{5.5}$$

Note that for a given experimental system, it is not unreasonable to assume one is able to measure J and the normal/shear crack-tip displacements. Without loss of generality, one can define $y \equiv \delta_{II,\circ}/\delta_{I,\circ}$ and see from

$$\begin{pmatrix} 1 & y \\ 1/y & 1 \end{pmatrix} \begin{pmatrix} \sigma \\ \tau \end{pmatrix} = \begin{pmatrix} dJ/d\delta_{I,\circ} \\ dJ/d\delta_{II,\circ} \end{pmatrix} \tag{5.6}$$

that $\underline{\underline{A}}$ is singular; therefore, one is dealing with a system with infinitely many solutions.

When dealing with a crack in a homogenous system (or an adhesive layer surrounded by homogenous adherends), there is an easy way around this cohesive-law coupling: one simply chooses specimen geometries that are nominally pure mode-I [2, 42] and pure mode-II [23, 16] such that the normal and shear cohesive laws can be separately determined. However, the particular challenge for cracks along a dissimilar-material interface (with $\bar{\beta} \neq 0$), is that the fracture is inherently mixed-mode and there is no mathematical way to separate them.

[1] While these results are derived from the assumption where the normal and shear stresses each depend on both the normal and shear displacements, one sees that removing this dependence doesn't change the convolution.

Knowing that each interface must be individually characterized, one runs into the conundrum that one cannot know one cohesive law without the other, and yet the fracture is inherently mixed-mode.

Wu *et. al.* [43, 112] developed methods of extracting mixed-mode traction-separation laws. In Ref. [43], a single geometry is used (the end-loaded split specimen) is used for mode extraction and the phase angle is varied through changing the adhesive thickness. The Abaqus implementation of the cohesive-zone model was used, which uses an effective displacement and stress, and has (in some versions) been shown [110] to be path dependent. In Ref. [112], the deconvolution is limited to those systems loaded using the edge-notched flexure (ENF) or end-loaded split (ELS) specimens[2] where one assumes a clamped geometry at the end away from the crack. This may or may not happen in practice, particularly for the ENF geometry which is often loaded using a three-point bend jig [23, 16]. In the present work, no such geometric assumptions are made, and the findings may be expanded to any geometry using a measured load-displacement curve, including the edge-notched flexure and end-loaded split geometries.

It should be noted that during the write-up of this manuscript, after the experiments and analyses were complete, it was observed that Pinto *et. al.* [114] extracted traction-separation laws using different adherends/methods: for mode-I, using bulk adhesive properties and a toughness from a DCB with steel adherends; for mode-II, a fitting procedure of the mode-II cohesive-law using a block-shear test with polyethylene adherends. This cohesive-law combination was then used to predict failure of single lap-shear joints with the similar and different adherends. For some combinations of adherends, aspects of specimen failure were able to be adequately reproduced. The authors' did not appear to realize the significance of their observation that there was no guarantee the approach would be valid/applicable.

5.2 Experimental deconvolution

A brief review of Section 4.5 is given below. The way around this inherent mixed-mode challenge was to assume the range of mode-I traction-separation laws extracted from the symmetric steel system adequately described the mode-I cohesive-failure along the composite-steel interface because both systems had crack propagation within the adhesive layer. Boundary conditions for the numerical partial-models were extracted from the geometry using DIC, with an appropriate measure of experimental uncertainty. With the mode-I cohe-

[2]Ref. [112] also varied one of the adherends throughout the testing in order to obtain wider range of (nominal) phase angle, and one wonders if some of the experimental scatter in the measurements might be due to varying the second adherend as opposed just the manufacturing variability of the adhesive. One also wonders how their choice of length scale affected the range of phase angles [113].

sive laws "known", the mode-II traction-separation law was manipulated until satisfactory agreement was found between the numerical predictions and experimental results *in the load-displacement data*. As an intital check, the experimental beam rotations were found to be in good agreement with the numerical predictions. The normal and shear cohesive-zone displacements were extracted using a method similar to that in Chapter 2, whereby the cohesive-zone displacements were measured just outside of the "interface region" caused by subset-based DIC. It was necessary to correct these displacements for rigid-body rotation for an accurate comparison to the numerical results, noting that the rotation correction needed to be done locally along the interface because the two beams did not rotate in unison. Following the rotation correction, the cohesive-zone displacements were found to have adequate agreement with the numerical predictions, and the traction-separation law was considered validated. The resulting traction-separation laws also allowed one to experimentally measure the phase angle along the interface.

5.3 Limitations and possible extensions

One method of extracting the mode-II traction-separation law has been presented above that is independent of the choice of geometry. It was observed during the experiments of the symmetric steel DCB experiments, the composite-steel lap-shear joint, and other geometries that are not presented here that the two-part structural epoxy (Dow Betamate® 73326M/73327M) nearly always failed via cohesive-failure (*i.e.* failure within the adhesive layer) regardless of the specimen geometry. Had the failure along the adhesive interface switched between cohesive-failure and adhesive-failure (failure between the adhesive layer and adherend), one could not assume the failure modes have similar fracture properties [2, 3]. Additionally, even though cohesive-failure occurred in both the symmetric steel system and the composite-steel system, there was no guarantee the mode-I traction-separation laws were equal as the adherend choice might have affected the adhesive's failure properties.

Unfortunately, the deconvolution method presented here does not address every issue. There may exist instances where the adhesive is bonded to different adherends and results in the case where the adhesive-failure (or cohesive-failure) is different than was previously characterized. In this instance, one is returned to the original problem: linear elasticity demonstrates that the normal/shear components are inherently coupled, and the cohesive-zone model requires knowledge of one traction-separation law to measure the other in a mixed-mode scenario.

If such a situation arises, one must consider a more general approach. It has been shown previously that load-displacement curves can be used to adequately determine traction-

separation laws [2, 23, 103, 21, 42, 104, 16]. Therefore, for a more general approach, perhaps two (or more) geometries need to be tested, using at least one mode-I dominant and mode-II dominant geometries: perhaps the double-cantilever beam and the lap-shear joint or edge-notched flexure specimens[3]. By running multiple trials of each geometry, one can then run numerical calculations (partial models or full models) and begin fitting the numerical load-displacement curves from different mode-I and mode-II laws to the experimental results. Upon finding the range of acceptable traction-separation laws that fit the (far-field) experimental results, one could then consider data fitting to individual specimens and comparing the cohesive-zone displacements.

One challenge in Section 4.5 was the fitting of a piecewise-linear function to a smooth curve. One solution to this might be to increase the number of segments so the lines do a better job approximating a curve. The downside to this improvement is that the numerical/experiment matching would become more tedious and time-consuming, and an optimization algorithm may need to be implemented to speed up the process [116, 117].

5.4 Summary

The constrained field-of-view/numerical partial-model method was validated using a composite-steel lap-shear joint in Chapter 4; however, the significance of this traction-separation law extraction is more than just the validation of analyzing the single lap-shear joint. This result provided an initial method demonstrating how one may deconvolute the inherently mixed-mode fracture along a dissimilar-material interface. Furthermore, this is a general method that is not constrained to only a particular geometry. A general method is proposed as to how one would tackle the problem of mixed-mode deconvolution in general, and this is a potential future project.

[3]Theoretically, the ENF specimen experiences pure shear at the crack-tip for arms of equal width and the same isotropic material [115]. The specimen also might be better for dealing with adhesives with a large cohesive-length because only one crack is present in the geometry, as opposed to two cracks/singularities in the single lap-shear joint.

CHAPTER 6

Conclusions

6.1 Summary

The analysis of the double-cantilever beam in Chapter 2 set the stage for more quantitative experimental analysis using digital image correlation. Numerous journal articles have been written about the DCB, yet none of the considered using full-field measurement capabilities to independently measure the mode-I traction-separation law and then compare the experimentally-measured cohesive-zone to numerical predictions. The standard beam theory assumption that "plane sections remain plane" when considering the deformation of beam-like geometries calls for the analog treatment of digital data, and this allows one to readily remove numerical artifacts. Such analyses allowed for the determination of the root rotation and elastic modulus, in addition to measuring the beam rotations and shear strain.

The next geometry to be considered was the single lap-shear joint in Chapter 3, with a varying fillet angle to determine the effect of different singularities. The subsequent numerical calculations and analyses gave a theoretical reason to the experimental observation that failure in lap-shear joints is (usually) independent of the presence or absence of a crack: as one increases the cohesive-length scale, the work done at the singularity approaches the value for that of a sharp crack. In the case of a corner, it just so happens that the work done at the singularity is close enough to the crack-tip value (at cohesive-length scale values where LEFM is a reasonable approximation) that any differences could be explained away as manufacturing variability. The agreement only gets better as one increases the cohesive-length scale. It was also found for non-crack singularities that both the cohesive-length scale and the shape of the cohesive laws determined the phase angle plateau.

Chapter 4 also analyzed the single lap-shear joint, but this time accounted for the unknown reactionary shear load required for clamped geometries and looked at geometric constraints. The shear load was found to be dependent on the cohesive laws and specimen geometry. Increasing the cohesive-length of the interface in a specimen pushed deformation

towards pure shear along the entire interface. Two methods for analyzing the lap-shear joint were demonstrated on a numerical model: the large-deformation J-integral and the numerical partial-model. The latter method was experimentally validated using the same adhesive from Chapter 2.

The experimental validation of the lap-shear geometry employed many of the same techniques that were used in Chapter 2: enforcing "plane sections remain plane" and the analog treatment of digital data. In exploratory numerical analyses, it was observed that the lap-shear joint was sensitive to boundary conditions, and therefore it is necessary to use a full-field measurement technique like DIC to extract them. Unlike the symmetric DCB, the lap-shear joint underwent mixed-mode loading and the rigid-body rotation correction was vital for the appropriate measurement of cohesive-zone displacements. With satisfactory agreement between the numerical predictions and experimental results of the beam rotations and cohesive-zone displacements, the numerical partial-model approach was considered validated.

The challenges of fracture along a dissimilar-material interface were considered in Chapter 5, along with the significance of the mixed-mode deconvolution that took place in Chapter 4. For a dissimilar-material interface the fracture is inherently mixed-mode, and in mixed-mode loading one must know one traction-separation law in order to extract the other. It was determined that the range of mode-I laws found in the symmetric steel DCB from Chapter 2 was an adequate measure of the mode-I cohesive laws for the composite-steel interface. This information was then used to successfully extract the mode-II cohesive-law by fitting the numerical results of the load-displacement curve to the experimental data. With the satisfactory agreement between the experimental beam rotations and cohesive-zone displacements and the numerical predictions, this mixed-mode deconvolution was considered a success.

In the experimental analysis of beam-like geometries, one expects that "plane sections remain plane" from standard beam theory. Put in the broader context of the DIC community, one could consider the experimental approach within this work to be similar to integrated-DIC (I-DIC) [118, 36] where *particular* shape functions are used to analyze the *expected* deformation of the system. This leads to increased measurement accuracy allowing for additional uses for I-DIC [119, 120, 121]. Instead of using specialized DIC software, a commerical software package is used with generic shape-functions, but the post-processing of the displacement data forced beams to deform according to beam theory. The additional thought taken during the analysis, whether during the image correlation or later in post-processing, allows for more accurate experimental measurements.

6.2 Future work

One of the author's long-term research interests lie in the field of dynamic fracture mechanics. The experimental work accomplished in Chapters 2 and 4 demonstrates a path forward to additional quantitative replication of cohesive-zone displacements in quasi-static experiments. Further work can and should be done on different geometries, but the methods developed here will provide a starting point for quantitative replication in dynamic fracture experiments. This thrust will help save resources long-term, with engineers knowing that the appropriate numerical calculations can accurately predict experimental results, minimzing the required physical testing of materials for design purposes.

Concerning quasi-static fracture, the edge-notched flexture (ENF) specimen is another system one could readily use full-field measurements to analyze. The symmetric double-cantilever beam provided a prototypical system for considering nominally pure mode-I fracture, and the symmetric ENF is nominally pure mode-II specimen [122, 123]. The ENF is typically loaded via a three-point bend jig, and has an analytical expression for the crack-tip work [115], though perhaps a J-integral formulation could be derived using Ref. [90]. Assuming a state of pure shear exists at the crack-tip, a direct differentiation approach could be used and the law could be numerically implemented in an FEM calculation to compare with the experimentally-measured displacements along the interface.

Ref. [124] considered the effect of wear on a corner with Coulomb friction and a limiting interfacial strength. In elastic contact, just like linear-elastic fracture mechanics, the nuanced details at the edge of the contact region determine the pressure distribution within the contacting region [124, 125]. By increasing the "slip" length scale (*i.e.* cohesive-length scale in fracture), the differences between the different fillet angle or smooth edge began to matter less [124].

The single lap-shear geometry worked was ideal for considering the effect of a fillet angle because one arm behind the singularity is free from loading, which is not the case for the DCB or ENF geometries. If one relaxes the requirement in Chapter 3 that the fillet angle must be a geometrical feature (*i.e.* the fillet angle must be the same value along the entire beam thickness) and consider the effect of microstructural features (as done in Ref. [124]), one would be able to analyze the DCB or ENF geometries. The findings from Ref. [124] and Chapter 3 suggest that at large enough cohesive-length scales any nuanced change at the singularity would be irrelevant, but at small cohesive-length scales these minute differences change in the interface deformation.

The work contained within this dissertation was originally motivated by the challenge of the deconvolution of the inherently mixed-mode fracture along a dissimilar-material in-

terface. The path to such success was not straightforward, but a solution was found. The numerical predictions of experimental results of the composite-steel lap-shear joint in Chapter 4 suggests one method for mixed-mode deconvolution now exists that is not dependent on using a particular specimen. Unfortunately, a general method of mixed-mode deconvolution of a dissimilar-material interface has not been determined, and therefore more work remains to be done.

As discussed in Section 5.3, one potential path forward on the general mixed-mode deconvolution problem is to simultaneously use multiple specimens with an experimental range of load-displacement curves, and use numerical models to match the macroscopic results of the experiments, with a range of acceptable uncertainty. Afterwards, one would then verify the extracted traction-separation laws adequately reproduce the experimental cohesive-zone displacements. If the results do not match, one may need to consider if the choice of traction-separation law (coupled versus uncoupled, effective displacement versus treating normal and shear displacements independently, etc.) is appropriate. To improve the matching capabilities, the number of segments in the piecewise-linear traction-separation laws may need to be increased. This increased complexity may end up requiring an optimization algorithm to match the far-field numerical-experimental comparison.

The challenge to both the validated method in Chapter 4 and the improvements suggested here is that they are inverse methods. Inverse methods are typically ill-posed [126], and in nonlinear problems there is no guarantee of a unique solution. The difficulty here is that the numerical partial-model method is reminiscent of finite element method updating (FEMU) [127, 128], an inverse method used to solve for constitutive properties of materials. FEMU works by comparing FEM results with experimental results, and trying to minimize some measure of error. In constitutive property identification, the other primary method is the virtual fields method (VFM) [129, 130, 131]. While FEMU requires numerous FEM calculations to converge to a solution, VFM allows material properties to be determined by analyzing experimental data alone. In this respect, Refs. [74, 101, 73] have accomplished the equivalent of this in extracting traction-separation laws directly from image deformation.

That being said, the author still suggests fitting the experimental data to load-displacement curves followed by comparison of the cohesive-zone displacements. This provides a secondary check on the experimental results, which was one of the main points of the experimental portions of Chapters 2 and 4: measure the traction-separation law using the far-field data, and validate the measured law using the close field-of-view data. If the displacement differences are large enough than what might be explained from experimental uncertainties or specimen variation/imperfections, the physics of the interface may be different. As an example, if one is able to match the loads well but not the cohesive-zone displacements, initially-

assumed uncoupled traction-separation laws may require coupled traction-separation laws. Using multiple samples with varying phase angles may also help determine whether or not the cohesive laws are coupled or uncoupled.

The work presented here has assumed planar geometries which can readily be measured by full-field measurement techniques such as digital image correlation. In practice, one knows that a full treatment requires three-dimensional specimens. The disadvantage of surface displacements was observed in Chapter 2 with the advent of a surface crack but no crack-propagation through the thickness. While 3-D displacement measurement has become more commonplace (*e.g.* digital volume correlation [132, 133, 134, 135]), fracture mechanics methods will likely move from planar analysis to 3-D analysis only in special cases (*e.g.* soft materials) where 3-D imaging is readily available. A more immediate improvement to the current work would be to use stereo-DIC, which uses multiple cameras in order to track out-of-plane motion [39]. Stereo DIC also allows for better planar displacement measurements. The methods developed here will be immediately applicable to analyzing planar geometries using Stereo-DIC, while similar methods could be used in the special case where one has internal three-dimensional displacement data of fracture.

APPENDIX A

Fortran-based user-defined element subroutine

The FORTRAN code below was implemented into Abaqus 6.14 as as user-defined element. It consists of 6-part, piecewise-linear traction-separation laws and a bi-linear traction-separation law for compression. It could be improved by expanding the code from a 2-D element to a 3-D element to include all three fracture modes: normal, in-plane shear, and out-of-plane shear.

```
CCCCCCCCCCCCCCCCCCCCCCCCCCCCCCCCCCCCCCCCCCCCCCCCCCCCCCCCCCCCCCCCCCCCCCCCCCCC

C UEL.f CCZM C
C
C This subroutine will implement a mixed-mode six-part, piecewise-linear
C traction-separation law (with a two-part normal compression option)
C CZM model to a user-defined element for use by Abaqus.

CCCCCCCCCCCCCCCCCCCCCCCCCCCCCCCCCCCCCCCCCCCCCCCCCCCCCCCCCCCCCCCCCCCCCCCCCCCC

  SUBROUTINE UEL(RHS,AMATRX,SVARS,ENERGY,NDOFEL,NRHS,NSVARS,
     1 PROPS,NPROPS,COORDS,MCRD,NNODE,U,DU,V,A,JTYPE,TIME,DTIME,
     2 KSTEP,KINC,JELEM,PARAMS,NDLOAD,JDLTYP,ADLMAG,PREDEF,NPREDF,
     3 LFLAGS,MLVARX,DDLMAG,MDLOAD,PNEWDT,JPROPS,NJPROP,PERIOD)

INCLUDE 'ABA_PARAM.INC'

DIMENSION RHS(MLVARX,*),AMATRX(NDOFEL,NDOFEL),PROPS(*),
     1 SVARS(*),ENERGY(8),COORDS(MCRD,NNODE),U(NDOFEL),
     2 DU(MLVARX,*),V(NDOFEL),A(NDOFEL),TIME(2),PARAMS(*),
```

```
     3 JDLTYP(MDLOAD,*),ADLMAG(MDLOAD),DDLMAG(MDLOAD,*),
     4 PREDEF(2,NPREDF,NNODE),LFLAGS(*),JPROPS(*)

DIMENSION C_COOR(2,4), R_COOR(2,4), R_F(8), R_MATRX(8,8),
     1 UY(2),UX(2),UY_P(2),UX_P(2),CI(2),C(2),PHI(2,2),
     2 STRN(2),STRT(2),SKNN(2),SKTT(2),SKNT(2),SKTN(2),FN(2),FT(2),
     3 STFN(2,2),STFT(2,2),SYMBOL(2),F_CRT(2),G_I(2),G_II(2),THIK(2)

! updated specifying variables...
DOUBLE PRECISION LAMBDAN1, LAMBDAN2, LAMBDAN3, LAMBDAN4,
     1 LAMBDAN5
DOUBLE PRECISION LAMBDAT1, LAMBDAT2, LAMBDAT3, LAMBDAT4,
     1 LAMBDAT5
C DOUBLE PRECISION SNC1, SNC2, DLTNC1, DLTNC2

C READ THE PROPERTIES OF CZM MODEL

C These values are for the mode-I tension law
SN1 = PROPS(1) !PEAK NORMAL STRESS 1
SN2 = PROPS(2) !PEAK NORMAL STRESS 2
SN3 = PROPS(3) !PEAK NORMAL STRESS 3
SN4 = PROPS(4) !PEAK NORMAL STRESS 4
SN5 = PROPS(5) !PEAK NORMAL STRESS 5
LAMBDAN1 = PROPS(6) !SHAPE PARAMETER LAMBDA1
LAMBDAN2 = PROPS(7) !SHAPE PARAMETER LAMBDA2
LAMBDAN3 = PROPS(8) !SHAPE PARAMETER LAMBDA3
LAMBDAN4 = PROPS(9) !SHAPE PARAMETER LAMBDA4
LAMBDAN5 = PROPS(10) !SHAPE PARAMETER LAMBDA5
DLTNC = PROPS(11) !CRITICAL NORMAL DISPLACEMENT
DLTN1 = LAMBDAN1
DLTN2 = LAMBDAN2
DLTN3 = LAMBDAN3
DLTN4 = LAMBDAN4
DLTN5 = LAMBDAN5
G_I0 = 0.5D0*(SN1*DLTN2-SN2*DLTN1+SN2*DLTN3-SN3*DLTN2
     1 +SN3*DLTN4-SN4*DLTN3+SN4*DLTN5-SN5*DLTN4+SN5*DLTNC)
```

```
C These values are for the mode-II law
ST1 = PROPS(12) !PEAK SHEAR STRESS 1
ST2 = PROPS(13) !PEAK SHEAR STRESS 2
ST3 = PROPS(14) !PEAK SHEAR STRESS 3
ST4 = PROPS(15) !PEAK SHEAR STRESS 4
ST5 = PROPS(16) !PEAK SHEAR STRESS 5
LAMBDAT1 = PROPS(17) !SHAPE PARAMETER LAMBDA1
LAMBDAT2 = PROPS(18) !SHAPE PARAMETER LAMBDA2
LAMBDAT3 = PROPS(19) !SHAPE PARAMETER LAMBDA3
LAMBDAT4 = PROPS(20) !SHAPE PARAMETER LAMBDA4
LAMBDAT5 = PROPS(21) !SHAPE PARAMETER LAMBDA5
DLTTC = PROPS(22) !CRITICAL SHEAR DISPLACEMENT
DLTT1 = LAMBDAT1
DLTT2 = LAMBDAT2
DLTT3 = LAMBDAT3
DLTT4 = LAMBDAT4
DLTT5 = LAMBDAT5
G_II0 = 0.5D0*(ST1*DLTT2-ST2*DLTT1+ST2*DLTT3-ST3*DLTT2
     1 +ST3*DLTT4-ST4*DLTT3+ST4*DLTT5-ST5*DLTT4+ST5*DLTTC)

C These values generate the mode-I bi-linear compression law
SNC1 = PROPS(25) !Compressive normal stress 1;
SNC2 = PROPS(26) !Compressive normal stress 2;
DLTNC1 = PROPS(27) !Compressive normal displacement 1
DLTNC2 = PROPS(28) !Compressive normal displacement 2

C This check sees if the user wants to use the bi-linear law
C ...generated, that is, if they input values equal to zero or are
C ... greater than zero, then they don't get to choose their bi-
C ...linear compression law.

 IF(DLTNC1 .GE. 0.0D0) THEN
SNC1 = -1.0D0*SN1
SNC2 = -1.0D0*SN2
DLTNC1 = -1.0D0*DLTN1
```

```
DLTNC2 = -1.0D0*DLTN2
 ENDIF
 IF(DLTNC2 .GE. 0.0D0) THEN
SNC1 = -1.0D0*SN1
SNC2 = -1.0D0*SN2
DLTNC1 = -1.0D0*DLTN1
DLTNC2 = -1.0D0*DLTN2
 ENDIF
 IF(SNC1 .GE. 0.0D0) THEN
SNC1 = -1.0D0*SN1
SNC2 = -1.0D0*SN2
DLTNC1 = -1.0D0*DLTN1
DLTNC2 = -1.0D0*DLTN2
 ENDIF
 IF(SNC2 .GE. 0.0D0) THEN
SNC1 = -1.0D0*SN1
SNC2 = -1.0D0*SN2
DLTNC1 = -1.0D0*DLTN1
DLTNC2 = -1.0D0*DLTN2
 ENDIF


SK = SN1/DLTN1 ! COMPRESSIVE STIFFNESS
FC = 0.0D0 ! FRICTION COEFFICIENT

AA=SVARS(1)
DT=SVARS(3)
AK=SVARS(5)
AG1=SVARS(6)
AG2=SVARS(7)

DT2=TIME(2)
X1=COORDS(1,1)
X2=COORDS(1,2)

BB1=SVARS(10)
```

```
KBB2=SVARS(11)
BB4=SVARS(13)

IF (BB1.GT.10.0D0) THEN

BB3=SVARS(12)
BB5=SVARS(14)
BB6=SVARS(15)
BB7=SVARS(16)
BB8=SVARS(17)

WRITE(*,2000) KBB2,BB3,BB4,BB5,BB6,BB7,BB8
2000  Format(I3," ",F10.6," ",F6.2," ",F6.3," ",F6.3," ",F6.3," ",
     1 F6.3)

END IF


DO 100 K1=1,NDOFEL
R_F(K1)=0.0D0
DO 110 KRHS=1,NRHS
RHS(K1,KRHS)=0.0D0
110  CONTINUE

DO 120 K2=1,NDOFEL
AMATRX(K2,K1)=0.0D0
R_MATRX(K2,K1)=0.0D0
120  CONTINUE
100  CONTINUE

C   READ THE STATE VARIABLES
C   SYMBOL(1)>=1.0 ==> 1ST LUMPED POINT HAS BEEN "SEPARATED"
C    SYMBOL(2)>=1.0 ==> 2ND LUMPED POINT HAS BEEN "SEPARATED"

SYMBOL(1)=SVARS(1)
SYMBOL(2)=SVARS(2)
```

```
C CURRENT COORDINATES FOR THE FOUR POINTS OF AN ELEMENT

C_COOR(1,1)=COORDS(1,1)+U(1)
C_COOR(2,1)=COORDS(2,1)+U(2)
C_COOR(1,2)=COORDS(1,2)+U(3)
C_COOR(2,2)=COORDS(2,2)+U(4)
C_COOR(1,3)=COORDS(1,3)+U(5)
C_COOR(2,3)=COORDS(2,3)+U(6)
C_COOR(1,4)=COORDS(1,4)+U(7)
C_COOR(2,4)=COORDS(2,4)+U(8)


THIK1_0=SQRT((COORDS(1,1)-COORDS(1,4))**2
     1   +(COORDS(2,1)-COORDS(2,4))**2.0)

THIK2_0=SQRT((COORDS(1,2)-COORDS(1,3))**2
     1   +(COORDS(2,2)-COORDS(2,3))**2.0)


THIK(1) = THIK1_0
THIK(2) = THIK2_0

C  COMPUTE THE ROTATION ANGLE

P1_X=(C_COOR(1,1)+C_COOR(1,4))/2.0D0
P1_Y=(C_COOR(2,1)+C_COOR(2,4))/2.0D0
P2_X=(C_COOR(1,2)+C_COOR(1,3))/2.0D0
P2_Y=(C_COOR(2,2)+C_COOR(2,3))/2.0D0


ALEN=SQRT((P1_X-P2_X)**2.0D0 + (P1_Y-P2_Y)**2.0D0) !LENGTH OF ELEMENT

IF((P2_Y-P1_Y).GE. 0.0D0) THEN

THETA= ACOS((P2_X - P1_X)/ALEN)
```

```
ELSE
THETA=-ACOS((P2_X - P1_X)/ALEN)

ENDIF

COS_PI = COS(THETA)

SIN_PI = SIN(THETA)

C COORDINATES TRANSFORMATION

R_COOR(1,1)= C_COOR(1,1)*COS_PI+C_COOR(2,1)*SIN_PI
R_COOR(2,1)=-C_COOR(1,1)*SIN_PI+C_COOR(2,1)*COS_PI
R_COOR(1,2)= C_COOR(1,2)*COS_PI+C_COOR(2,2)*SIN_PI
R_COOR(2,2)=-C_COOR(1,2)*SIN_PI+C_COOR(2,2)*COS_PI
R_COOR(1,3)= C_COOR(1,3)*COS_PI+C_COOR(2,3)*SIN_PI
R_COOR(2,3)=-C_COOR(1,3)*SIN_PI+C_COOR(2,3)*COS_PI
R_COOR(1,4)= C_COOR(1,4)*COS_PI+C_COOR(2,4)*SIN_PI
R_COOR(2,4)=-C_COOR(1,4)*SIN_PI+C_COOR(2,4)*COS_PI


C COMPUTE THE RELATIVE DISPLACEMENTS IN LOCAL COORDINATE SYSTEM

UX(1) = R_COOR(1,4) - R_COOR(1,1) !U(7)-U(1)
UX(2) = R_COOR(1,3) - R_COOR(1,2) !U(5)-U(3)
UY(1) = R_COOR(2,4) - R_COOR(2,1) - THIK1_0 !U(8)-U(2)
UY(2) = R_COOR(2,3) - R_COOR(2,2) - THIK2_0 !U(6)-U(4)


C THE NODE FORCES AND STIFF MATRIX IS INTEGRATED USING 2 POINT LUMPED
C QUADRATURE SCHEME

CI(1) =-1.0D0 !LUMPED INTEGRATION POINT1
CI(2) = 1.0D0 !LUMPED INTEGRATION POINT2
C(1) =-1.0D0
```

```
C(2) = 1.0D0


DO 200 I=1, 2

UY_P(I) = 0.0D0
UX_P(I) = 0.0D0


DO 210 J=1, 2

!Jth INTERPOLATION FUNCTION EVALUATED IN Ith LUMPED POINT
PHI(J,I)= (1.0D0+C(J)*CI(I))/2.0D0
!RELATIVE DISPLACEMENT EVALUATED IN Ith LUMPED POINT
UY_P(I) = UY_P(I) + PHI(J,I)*UY(J)
UX_P(I) = UX_P(I) + PHI(J,I)*UX(J)

210  CONTINUE

C CALCULATE THE NORMAL COHESIVE STRESS, SLOPE AND ENERGY RELEASE
C RATE IN Ith LUMPED POINT

CALL NOR(SN1,SN2,SN3,SN4,SN5,DLTN1,DLTN2,DLTN3,DLTN4,DLTN5,
     1 DLTNC,SNC1,SNC2,DLTNC1,DLTNC2,UY_P(I),STRN(I),SKNN(I),G_I(I))
C UY_P(I),STRN(I),SKNN(I),G_I(I))!


C CALCULATE THE SHEAR COHESIVE STRESS, SLOPE AND ENERGY RELEASE
C RATE IN Ith LUMPED POINT

CALL SHR(ST1,ST2,ST3,ST4,ST5,DLTT1,DLTT2,DLTT3,DLTT4,DLTT5,
     1 DLTTC,UX_P(I),STRT(I),SKTT(I),G_II(I))

C FAILURE CRITERION IN Ith LUMPED POINT

F_CRT(I)=G_I(I)/G_I0 + G_II(I)/G_II0
```

```
C Ith LUMPED POINT HAVE BEEN "SEPARATED"
C PREVENT "BROKEN" ELEMENTS FROM BEING INVOLVED AGAIN


IF((SYMBOL(I) .LE. 1.0D0)) THEN
SYMBOL(I)=F_CRT(I)
END IF


200  CONTINUE

DO 300 I=1,2
C  IF ONE OF THE LUMPED POINT IS BROKEN

IF(SYMBOL(I) .GE. 1.0D0) THEN
STRT(I) = 0.0D0
STRN(I) = 0.0D0
SKTT(I) = 0.0D0
SKNN(I) = 0.0D0


C AVOID INTERPENETRATION IN LUMPED POINT

IF( UY_P(I) .LE. -1.0D-6) THEN
!NODES I HAVE BEEN "INTERPENETRATED"
STRN(I) = SK*UY_P(I)
SKNN(I) = SK
SYMBOL(I)= 10.0D0

END IF

END IF
300  CONTINUE

DO 400 I=1,2
```

```
FN(I) = 0.0D0
FT(I) = 0.0D0
DO 410 J=1,2
FN(I) = FN(I)+PHI(I,J)*STRN(J)*ALEN/2.0D0
FT(I) = FT(I)+PHI(I,J)*STRT(J)*ALEN/2.0D0
STFN(I,J) = 0.0D0
STFT(I,J) = 0.0D0


DO 420 K=1,2
STFN(I,J) = STFN(I,J)+PHI(I,K)*PHI(J,K)*SKNN(K)*
     1 ALEN/2.0D0
STFT(I,J) = STFT(I,J)+PHI(I,K)*PHI(J,K)*SKTT(K)*
     1 ALEN/2.0D0

420  CONTINUE
410  CONTINUE

C MODIFIED TANGENTIAL STIFFNESS


IF (STFN(I,I) .LT. 0.0D0) THEN
STFN(I,I) = 0.0D0
END IF
IF (STFT(I,I) .LT. 0.0D0) THEN

STFT(I,I) = 0.0D0
END IF
400  CONTINUE

C  LOCAL STIFFNESS MATRIX AND RESIDUE FORCE VECTOR

DO 500 I = 1, 2
DO 510 J = 1, 2

C LOCAL STIFFNESS MATRIX
```

```
R_MATRX(2*(I-1)+1, 2*(J-1)+1) = STFT(I,J)
R_MATRX(2*(I-1)+2, 2*(J-1)+2) = STFN(I,J)
R_MATRX(2*(4-I)+1, 2*(J-1)+1) =-STFT(I,J)
R_MATRX(2*(4-I)+2, 2*(J-1)+2) =-STFN(I,J)
R_MATRX(2*(I-1)+1, 2*(4-J)+1) =-STFT(I,J)
R_MATRX(2*(I-1)+2, 2*(4-J)+2) =-STFN(I,J)
R_MATRX(2*(4-I)+1, 2*(4-J)+1) = STFT(I,J)
R_MATRX(2*(4-I)+2, 2*(4-J)+2) = STFN(I,J)

510  CONTINUE


C  LOCAL RESIDUE FORCE VECTOR
R_F(2*(I-1)+1) = FT(I)
R_F(2*(4-I)+1) =-FT(I)
R_F(2*(I-1)+2) = FN(I)
R_F(2*(4-I)+2) =-FN(I)

C  UPDATE INTERNAL VARIABLES

SVARS(I) =SYMBOL(I)

500  CONTINUE


C  CCZM: factors

 DK=THIK(1)/ALEN
ADK=-UX_P(1)/ALEN
ADK2=-UX_P(2)/ALEN


C  IF ONE OF THE LUMPED POINT IS BROKEN
IF((SYMBOL(1) .GE. 1.0D0).OR.(SYMBOL(2) .GE. 1.0D0)) THEN
DK = 0.0D0
ADK = 0.0D0
```

```
ADK2 = 0.0D0
IF( UY_P(I) .LE. -1.0D-6) THEN
ADK=-UX_P(1)/ALEN
ADK2=-UX_P(2)/ALEN
END IF
END IF

C CCZM: BALANCING THE MOMENT EFFECTS

 R_MATRX(2,1)=DK*SKTT(1)*ALEN/2.0D0
R_MATRX(2,7)=-DK*SKTT(1)*ALEN/2.0D0
R_MATRX(4,1)=-DK*SKTT(1)*ALEN/2.0D0
R_MATRX(4,7)=DK*SKTT(1)*ALEN/2.0D0

 R_MATRX(8,3)=DK*SKTT(2)*ALEN/2.0D0
R_MATRX(8,5)=-DK*SKTT(2)*ALEN/2.0D0
R_MATRX(6,3)=-DK*SKTT(2)*ALEN/2.0D0
R_MATRX(6,5)=DK*SKTT(2)*ALEN/2.0D0

R_F(2)=R_F(2)+DK*FT(1)
R_F(4)=R_F(4)-DK*FT(1)
R_F(6)=R_F(6)-DK*FT(2)
R_F(8)=R_F(8)+DK*FT(2)

 R_MATRX(2,2)=R_MATRX(2,2)+ADK*SKNN(1)*ALEN/2.0D0
R_MATRX(2,8)=R_MATRX(2,8)-ADK*SKNN(1)*ALEN/2.0D0
R_MATRX(4,2)=R_MATRX(4,2)-ADK*SKNN(1)*ALEN/2.0D0
R_MATRX(4,8)=R_MATRX(4,8)+ADK*SKNN(1)*ALEN/2.0D0

 R_MATRX(8,4)=R_MATRX(8,4)+ADK2*SKNN(2)*ALEN/2.0D0
R_MATRX(8,6)=R_MATRX(8,6)-ADK2*SKNN(2)*ALEN/2.0D0
R_MATRX(6,4)=R_MATRX(6,4)-ADK2*SKNN(2)*ALEN/2.0D0
R_MATRX(6,6)=R_MATRX(6,6)+ADK2*SKNN(2)*ALEN/2.0D0



R_F(2)=R_F(2)+ADK*FN(1)
```

```
R_F(4)=R_F(4)-ADK2*FN(1)
R_F(6)=R_F(6)-ADK2*FN(2)
R_F(8)=R_F(8)+ADK*FN(2)


C OUTPUT THE CRACK LENGTH AS THE CZ ELEMENT IS BROKEN

SVARS(3)=DT2
SVARS(6)=G_I(1)
SVARS(7)=G_II(1)
SVARS(21)=STRN(1)
SVARS(22)=STRT(1)
SVARS(5)=KINC

C Phase angle calculation...
C This was updated such that phase angles could include the full
C range from -180->180 degrees.

C when we have tensile opening displacements...
IF (G_I(1).GE. 0.0D0) THEN !A
C ...and positive shear
IF (UX(1) .GE. 0.0D0) THEN !B
SVARS(16)=ATAN2(SQRT(G_II(1)),SQRT(G_I(1)))*180.0D0/3.14D0
C ...and negative shear
ELSE !B
SVARS(16)=ATAN2(-1.D0*SQRT(G_II(1)),SQRT(G_I(1)))*180.0D0/3.14D0
END IF !B
C when we have compressive opening displacements...
ELSE !A
C ...and positive shear
IF (UX(1) .GE. 0.0D0) THEN !C
SVARS(16)=ATAN2(SQRT(G_II(1)),-1.0D0*SQRT(ABS(G_I(1))))
     1   *180.0D0/3.14D0
C ...and negative shear
ELSE !C
SVARS(16)=ATAN2(-1.0D0*SQRT(G_II(1)),-1.0D0*SQRT(ABS(G_I(1))))
```

```
     1   *180.0D0/3.14D0
END IF !C
END IF !A



IF ((AA.LT.1.0D0).AND.(SYMBOL(1).GE.1.0D0)) THEN
AC=100.0


SVARS(11)=AK
SVARS(12)=DT
SVARS(13)=X1
SVARS(14)=AG1
SVARS(15)=AG2


ELSE

AC=1.0

END IF

C  IF ELEMENT HAS FAILED, ASSIGN A 0 TO SDV(17)
IF (F_CRT(1).GE.1.0D0) THEN
SVARS(17)=F_CRT(1)
ELSE
SVARS(17)=F_CRT(1)
END IF

SVARS(10)=AC
SVARS(18)=STRT(1)
SVARS(19)=UY_P(1)
SVARS(20)=UX_P(1)
```

```
C  FORM THE GLOBAL STIFFNESS MATRIX AND RESIDUAL FORCE
DO 600 I=1,7,2
DO 610 J=1,7,2
AMATRX( I, J) = R_MATRX( I, J)*COS_PI**2.0D0
     1  +R_MATRX(I+1,J+1)*SIN_PI**2.0D0
     2  -R_MATRX( I,J+1)*SIN_PI*COS_PI
     3  -R_MATRX(I+1, J)*SIN_PI*COS_PI

AMATRX(I+1, J) = R_MATRX( I, J)*SIN_PI*COS_PI-
     1  R_MATRX(I+1,J+1)*SIN_PI*COS_PI-
     2  R_MATRX( I,J+1)*SIN_PI**2.0D0+
     3  R_MATRX(I+1, J)*COS_PI**2.0D0

AMATRX( I,J+1) = R_MATRX( I, J)*SIN_PI*COS_PI-
     1  R_MATRX(I+1,J+1)*SIN_PI*COS_PI+
     2  R_MATRX( I,J+1)*COS_PI**2.0D0-
     3  R_MATRX(I+1, J)*SIN_PI**2.0D0

AMATRX(I+1,J+1) = R_MATRX( I, J)*SIN_PI**2.0D0+
     1  R_MATRX(I+1,J+1)*COS_PI**2.0D0+
     2  R_MATRX( I,J+1)*SIN_PI*COS_PI+
     3  R_MATRX(I+1, J)*SIN_PI*COS_PI

610  CONTINUE
RHS(I ,1)= R_F(I)*COS_PI - R_F(I+1)*SIN_PI
RHS(I+1,1)= R_F(I)*SIN_PI + R_F(I+1)*COS_PI

600  CONTINUE

RETURN
END


C  CALCULATE THE NORMAL COHESIVE STRESS, SLOPE AND ENERGY RELEASE
C  RATE IN Ith LUMPED POINT
```

```
SUBROUTINE NOR(SN1,SN2,SN3,SN4,SN5,DLTN1,DLTN2,DLTN3,DLTN4,
     1 DLTN5,DLTNC,SNC1,SNC2,DLTNC1,DLTNC2,UY,STRN,SKN,G_I)
IMPLICIT DOUBLE PRECISION(A-H, O-Z)
SN0 = 0.0D0
SN6 = 0.0D0  !modified
DLTN0= 0.0D0

C for the regions in tension...
SKN1 = (SN1-SN0)/(DLTN1-DLTN0)
SKN2 = (SN2-SN1)/(DLTN2-DLTN1)
SKN3 = (SN3-SN2)/(DLTN3-DLTN2)
SKN4 = (SN4-SN3)/(DLTN4-DLTN3)
SKN5 = (SN5-SN4)/(DLTN5-DLTN4)
SKN6 = (SN6-SN5)/(DLTNC-DLTN5)

C for the regions in compression...
SKNC1 = (SN0-SNC1)/(DLTN0-DLTNC1)
SKNC2 = (SNC1-SNC2)/(DLTNC1-DLTNC2)

STRN = 0.0D0
SKN = 0.0D0
G_I = 0.0D0
C0 = 0.0D0

C Here, we consider whether or not to allow a two-part compression law.
C This selection allows one to have a two-part compression.
 IF(UY .LE. DLTNC1) THEN ! IF UY is less than the bi-linear kink
 IF(SKNC2 .GE. 0.0D0) THEN !IF SKNC2 is positive -- done
STRN = -1.0D0*(ABS(SNC1)+ABS(SKNC2)*(ABS(UY)-ABS(DLTN1)))
SKN = SKNC2
G_I = -1.0D0*(0.5D0*(SN0+SNC1)*(DLTNC1-DLTN0)+
     1  0.5D0*(SNC1+STRN)*(UY -DLTNC1))

C However, if the slope of the second line (from point 1 to point 2) is
C ...negative, then there is only a one-part compression law. This is a
```

```
C ...safety check, because if the second line's slope is negative, then
C ...one might eventually get a positive normal displacement for
C ...compression, which is not physical.
 ELSE IF(SKNC2 .LT. 0.0D0) THEN !IF SKNC2 is negative -- done
STRN = UY*SKNC1
SKN = SKNC1
G_I = -0.5D0*SKNC1*UY*UY
 ENDIF! ENDIF SKNC2 is negative
 ENDIF!ENDIF UY is less than the bi-linear kink

 IF((UY .GT. DLTNC1) .AND. (UY .LE. C0)) THEN
STRN = UY*SKNC1
SKN = SKNC1
G_I = -0.5D0*SKNC1*UY*UY
 ENDIF

 IF((UY .GT. C0) .AND. (UY .LE. DLTN1)) THEN
STRN = UY*SKN1
SKN = SKN1
G_I = 0.5D0*SKN1*UY*UY
 ENDIF

IF((UY .GT. DLTN1).AND.(UY .LE. DLTN2)) THEN

STRN = SN1+SKN2*(UY-DLTN1)
SKN = SKN2
G_I = 0.5D0*(SN0+SN1)*(DLTN1-DLTN0)+
     1  0.5D0*(SN1+STRN)*(UY -DLTN1)
ENDIF

 IF((UY .GT. DLTN2).AND.(UY .LE. DLTN3)) THEN

STRN = SN2+SKN3*(UY-DLTN2)
SKN = SKN3
G_I = 0.5D0*(SN0+SN1)*(DLTN1-DLTN0)+
     1  0.5D0*(SN1+SN2)*(DLTN2-DLTN1)+
```

```
     2   0.5D0*(SN2+STRN)*(UY -DLTN2)
ENDIF

 IF((UY .GT. DLTN3).AND.(UY .LE. DLTN4)) THEN

STRN = SN3+SKN4*(UY-DLTN3)
SKN = SKN4
G_I = 0.5D0*(SN0+SN1)*(DLTN1-DLTN0)+
     1  0.5D0*(SN1+SN2)*(DLTN2-DLTN1)+
     2   0.5D0*(SN2+SN3)*(DLTN3-DLTN2)+
     3 0.5D0*(SN3+STRN)*(UY -DLTN3)
ENDIF

 IF((UY .GT. DLTN4).AND.(UY .LE. DLTN5)) THEN

STRN = SN4+SKN5*(UY-DLTN4)
SKN = SKN5
G_I = 0.5D0*(SN0+SN1)*(DLTN1-DLTN0)+
     1  0.5D0*(SN1+SN2)*(DLTN2-DLTN1)+
     2   0.5D0*(SN2+SN3)*(DLTN3-DLTN2)+
     3 0.5D0*(SN3+SN4)*(DLTN4-DLTN3)+
     4 0.5D0*(SN4+STRN)*(UY -DLTN4)
ENDIF

 IF((UY .GT. DLTN5).AND.(UY .LE. DLTNC)) THEN

STRN = SN5+SKN6*(UY-DLTN5)
SKN = SKN6
G_I = 0.5D0*(SN0+SN1)*(DLTN1-DLTN0)+
     1  0.5D0*(SN1+SN2)*(DLTN2-DLTN1)+
     2   0.5D0*(SN2+SN3)*(DLTN3-DLTN2)+
     3 0.5D0*(SN3+SN4)*(DLTN4-DLTN3)+
     4 0.5D0*(SN4+SN5)*(DLTN5-DLTN4)+
     5 0.5D0*(SN5+STRN)*(UY -DLTN5)
ENDIF
C IF BROKEN WRT MODE I, SET G_I TO G_I0
```

```
 IF(UY .GT. DLTNC) THEN
STRN = 0.0D0
SKN = 0.0D0
G_I = 0.5D0*(SN1*DLTN2-SN2*DLTN1+SN2*DLTN3-SN3*DLTN2
     1 +SN3*DLTN4-SN4*DLTN3+SN4*DLTN5-SN5*DLTN4+SN5*DLTNC)
 ENDIF

RETURN
END


C CALCULATE THE SHEAR COHESIVE STRESS, SLOPE AND ENERGY RELEASE
C RATE IN Ith LUMPED POINT

SUBROUTINE SHR(ST1,ST2,ST3,ST4,ST5,DLTT1,DLTT2,DLTT3,DLTT4,
     1 DLTT5,DLTTC,UX,STRT,SKT,G_II)
IMPLICIT DOUBLE PRECISION(A-H, O-Z)

ST0 = 0.0D0
ST6 = 0.0D0
DLTT0= 0.0D0

SKT1 = (ST1-ST0)/(DLTT1-DLTT0)
SKT2 = (ST2-ST1)/(DLTT2-DLTT1)
SKT3 = (ST3-ST2)/(DLTT3-DLTT2)
SKT4 = (ST4-ST3)/(DLTT4-DLTT3)
SKT5 = (ST5-ST4)/(DLTT5-DLTT4)
SKT6 = (ST6-ST5)/(DLTTC-DLTT5)

STRT = 0.0D0
SKT = 0.0D0


 IF(ABS(UX) .LE. DLTT1) THEN
STRT = UX*SKT1
```

```
SKT = SKT1
G_II = 0.5D0*SKT1*ABS(UX)*ABS(UX)

 ENDIF

 IF((ABS(UX) .GT. DLTT1).AND.(ABS(UX) .LE. DLTT2)) THEN
STRT =(ST1+SKT2*(ABS(UX)-DLTT1))*ABS(UX)/UX
SKT = SKT2
G_II = 0.5D0*(ABS(ST0)+ABS(ST1))*(DLTT1 -DLTT0)+
     1  0.5D0*(ABS(ST1)+ABS(STRT))*(ABS(UX)-DLTT1)
ENDIF

 IF((ABS(UX) .GT. DLTT2).AND.(ABS(UX) .LE. DLTT3)) THEN

STRT =(ST2+SKT3*(ABS(UX)-DLTT2))*ABS(UX)/UX
SKT = SKT3
G_II = 0.5D0*(ABS(ST0)+ABS(ST1))*(DLTT1 -DLTT0)+
     1  0.5D0*(ABS(ST1)+ABS(ST2))*(DLTT2 -DLTT1)+
     2  0.5D0*(ABS(ST2)+ABS(STRT))*(ABS(UX)-DLTT2)
ENDIF

 IF((ABS(UX) .GT. DLTT3).AND.(ABS(UX) .LE. DLTT4)) THEN

STRT =(ST3+SKT4*(ABS(UX)-DLTT3))*ABS(UX)/UX
SKT = SKT4
G_II = 0.5D0*(ABS(ST0)+ABS(ST1))*(DLTT1 -DLTT0)+
     1  0.5D0*(ABS(ST1)+ABS(ST2))*(DLTT2 -DLTT1)+
     2  0.5D0*(ABS(ST2)+ABS(ST3))*(DLTT3 -DLTT2)+
     3  0.5D0*(ABS(ST3)+ABS(STRT))*(ABS(UX)-DLTT3)
ENDIF

 IF((ABS(UX) .GT. DLTT4).AND.(ABS(UX) .LE. DLTT5)) THEN

STRT =(ST4+SKT5*(ABS(UX)-DLTT4))*ABS(UX)/UX
SKT = SKT5
G_II = 0.5D0*(ABS(ST0)+ABS(ST1))*(DLTT1 -DLTT0)+
```

```
     1  0.5D0*(ABS(ST1)+ABS(ST2))*(DLTT2 -DLTT1)+
     2  0.5D0*(ABS(ST2)+ABS(ST3))*(DLTT3 -DLTT2)+
     3  0.5D0*(ABS(ST3)+ABS(ST4))*(DLTT4 -DLTT3)+
     4  0.5D0*(ABS(ST4)+ABS(STRT))*(ABS(UX)-DLTT4)
ENDIF

 IF((ABS(UX) .GT. DLTT5).AND.(ABS(UX) .LE. DLTTC)) THEN

STRT =(ST5+SKT6*(ABS(UX)-DLTT5))*ABS(UX)/UX
SKT = SKT6
G_II = 0.5D0*(ABS(ST0)+ABS(ST1))*(DLTT1 -DLTT0)+
     1  0.5D0*(ABS(ST1)+ABS(ST2))*(DLTT2 -DLTT1)+
     2  0.5D0*(ABS(ST2)+ABS(ST3))*(DLTT3 -DLTT2)+
     3  0.5D0*(ABS(ST3)+ABS(ST4))*(DLTT4 -DLTT3)+
     4  0.5D0*(ABS(ST4)+ABS(ST5))*(DLTT5 -DLTT4)+
     5  0.5D0*(ABS(ST5)+ABS(STRT))*(ABS(UX)-DLTT5)
ENDIF

C IF BROKEN WRT MODE II, SET G_II TO G_II0

 IF(ABS(UX) .GT. DLTTC) THEN
STRT = 0.0D0
SKT = 0.0D0
G_II = 0.5D0*(ST1*DLTT2-ST2*DLTT1+ST2*DLTT3-ST3*DLTT2
     1 +ST3*DLTT4-ST4*DLTT3+ST4*DLTT5-ST5*DLTT4+ST5*DLTTC)

 ENDIF

RETURN
END
```

APPENDIX B

Python-based piecewise polynomial, C^1-continuous, least squares fitting scheme

The code below works for Python 2.7. Unfortunately, due to the use of the Vandermonde matrix, it is ill-conditioned. It could be improved by using LU factorization, QR factorization, or singular value decomposition (SVD) to solve the constrained least-squares problem. The use of the SVD is not expected to noticeably slow down the fitting script as the number of data points one typically fits is "small".

```
import csv                          #used to write output file(s)
import numpy as np                  #math/array manipulation module
import scipy as sp                  #scientific computing module
from scipy import optimize          #optimization module
import matplotlib.pyplot as plt     #plotting library
from matplotlib import rc           #nicer plot fonts

rc('font',**{'family':'serif','serif':['Computer Modern']})
rc('text', usetex=True)

text_size=18

#used to have rotate through line colors when plotting fits
color_line = ['b-', 'r-', 'g-', 'c-', 'm-', 'y-', 'k-']

#Ax=b ---- standard least squares minimization
def objective(x_vec, b_vec, A_mat):
```

```
    return np.sum(np.power((b_vec - np.dot(A_mat, x_vec)), 2.))

#A_1 x_1 = b_1, A_2 x_2 = b_2----combined least squares minimization of two
#...separate sections: here, the two sections are cubic and affine (linear)
def objective2(x_vec, short_dat, lhs_bdry, rhs_bdry):
  global x_column, y_column

  short_dat_cub = np.delete(data, np.where(np.logical_or(data[:,x_column]<\
  lhs_bdry, data[:,x_column] > x_vec[4])), axis=0)
  short_dat_aff = np.delete(data, np.where(np.logical_or(data[:,x_column]<\
  x_vec[4], data[:,x_column] > rhs_bdry)), axis=0)
  for j in range(0, len(short_dat_cub[:,x_column])):
    if j==0:
      a_mat3 = [[np.power(short_dat_cub[j,x_column], 3.), \
      np.power(short_dat_cub[j,x_column], 2.), short_dat_cub[j,x_column] \
      , 1.]]
      b_vec3 = [short_dat_cub[j,y_column]]
    else:
      a_mat3.append([np.power(short_dat_cub[j,x_column], 3.), \
      np.power(short_dat_cub[j,x_column], 2.), short_dat_cub[j,x_column] \
      , 1.])
      b_vec3.append(short_dat_cub[j,y_column])
  for j in range(0, len(short_dat_aff[:,x_column])):
    if j==0:
      a_mat1 = [[short_dat_aff[j,x_column], 1.]]
      b_vec1 = [short_dat_aff[j,y_column]]
    else:
      a_mat1.append([short_dat_aff[j,x_column], 1.])
      b_vec1.append(short_dat_aff[j,y_column])
  least_squares_val = np.sum(np.power((b_vec3 - np.dot(a_mat3, [x_vec[0],\
  x_vec[1], x_vec[2], x_vec[3]])), 2.)) + np.sum(np.power((b_vec1 - \
  np.dot(a_mat1, [3.*x_vec[0]*x_vec[4]*x_vec[4]+2.*x_vec[1]*x_vec[4] + \
  x_vec[2], -2.*x_vec[0]*x_vec[4]*x_vec[4]*x_vec[4] - \
  x_vec[1]*x_vec[4]*x_vec[4]+x_vec[3]])), 2.))
  return least_squares_val
```

```
def on_key(event):
  global count,lhs_bdry,rhs_bdry,steady_state_x_value,x_column,y_column
  #letter (capital and lowercase) on the keyboard...
  if event.key=='e':
    raise SystemExit
#============================================================================
  if event.key=='q':
    plt.close()
#============================================================================
  if event.key=='w':
  #intermediary location least-squares affine fit
  #use a cubic spline to enforce continuity...
    if aff_guess1 > aff_guess2:
      temp_lhs_bdry = aff_guess2; temp_rhs_bdry = aff_guess1;
    else:
      temp_lhs_bdry = aff_guess1; temp_rhs_bdry = aff_guess2;
    short_dat = np.delete(data, np.where(np.logical_or(data[:,x_column] < \
    temp_lhs_bdry, data[:,x_column] > temp_rhs_bdry)), axis=0)
    for j in range(0, len(short_dat[:,x_column])):
      if j==0:
        a_mat = [[short_dat[j,x_column], 1.]]
        b_vec = [short_dat[j,y_column]]
      else:
        a_mat.append([short_dat[j,x_column], 1.])
        b_vec.append(short_dat[j,y_column])
  #solve system
    a_mat_trans = np.transpose(a_mat)
    a_tr_a_mat = np.dot(a_mat_trans, a_mat)
    a_tr_b_vec = np.dot(a_mat_trans, b_vec)
    x_vec = np.linalg.solve(a_tr_a_mat, a_tr_b_vec)
    print x_vec[0]
  #plot affine fit for guessing
    plt.plot(data[:,x_column], x_vec[0]*data[:,x_column] + x_vec[1], 'r:')
    plt.show()
#============================================================================
```

```
elif event.key=='c':
#cubic spline fit
  short_dat = np.delete(data, np.where(np.logical_or(data[:,x_column] < \
  lhs_bdry, data[:,x_column] > rhs_bdry)), axis=0)
  c_l = raw_input('LHS section number: '); c_l = int(c_l)
  c_r = raw_input('RHS section number: '); c_r = int(c_r)
#specify constants
  output_dat = np.genfromtxt(export_file,delimiter=',', skip_header=1)
  x_l = short_dat[0,x_column];
  y_l = output_dat[c_l,4]*x_l*x_l*x_l + output_dat[c_l,5]*x_l*x_l + \
  output_dat[c_l,6]*x_l + output_dat[c_l,7];
  k_l = 3.*output_dat[c_l,4]*x_l*x_l + 2.*output_dat[c_l,5]*x_l + \
  output_dat[c_l,6]
  x_r = short_dat[-1,x_column];
  y_r = output_dat[c_r,4]*x_r*x_r*x_r + output_dat[c_r,5]*x_r*x_r + \
  output_dat[c_r,6]*x_r + output_dat[c_r,7];
  k_r = 3.*output_dat[c_r,4]*x_r*x_r + 2.*output_dat[c_r,5]*x_r + \
  output_dat[c_r,6]
#solve cubic spline
  x3_c = 1./np.power(x_l-x_r,3.)*((k_l+k_r)*(x_l-x_r)-2.*y_l+2.*y_r)
  x2_c = 1./np.power(x_l-x_r,3.)*(-1.*k_l*(x_l-x_r)*(x_l+\
  2.*x_r)+k_r*(-2.*x_l*x_l+x_l*x_r+x_r*x_r)+3.*(x_l+x_r)*(y_l-y_r))
  x1_c = 1./np.power(x_l-x_r,3.)*(k_r*x_l*(x_l-x_r)*(x_l+2.*x_r)-\
  x_r*(k_l*(-2.*x_l*x_l+x_l*x_r+x_r*x_r)+6.*x_l*(y_l-y_r)))
  x0_c = 1./np.power(x_l-x_r,3.)*(x_r*(x_l*(-1.*x_l+x_r)*(k_r*x_l+\
  k_l*x_r)-x_r*(-3.*x_l+x_r)*y_l)+x_l*x_l*(x_l-3.*x_r)*y_r)
#output data
  output.append([count, 3.01, short_dat[0,x_column], \
  short_dat[-1,x_column], x3_c, x2_c, x1_c, x0_c])
#increase count...
  count=count+1.
#export data
  with open(export_file, 'wb') as f:
    writer = csv.writer(f)
    for row in output:
    writer.writerow(row)
```

```
  #plot cubic spline
    spline_dat = np.linspace(x_l, x_r, 100)
    plt.plot(spline_dat, np.multiply(x3_c,np.power(spline_dat,3.)) + \
    np.multiply(x2_c,np.power(spline_dat,2.)) + np.multiply(x1_c,\
    np.power(spline_dat,1.)) + np.multiply(x0_c,np.power(spline_dat,0.)), \
    color_line[int(np.mod(count,1.*len(color_line))-1)])
    plt.show()
#=========================================================================
  elif event.key=='0':
  #steady state value... no data is recorded here...
    short_dat = np.delete(data, np.where(np.logical_or(data[:,x_column] < \
    lhs_bdry, data[:,x_column] > rhs_bdry)), axis=0)
    steady_state_y_value = np.mean(short_dat[:,y_column])
    steady_val = np.full(len(short_dat[:,x_column]), steady_state_y_value)
    steady_state_x_value = np.amin(short_dat[:,x_column])
    print('mean value: '+str(steady_state_y_value))
    plt.plot(short_dat[:,x_column], steady_val, 'k:')
#=========================================================================
  elif event.key=='1':
    if count==0.:
    #initial section least squares affine fit
      short_dat = np.delete(data, np.where(np.logical_or(data[:,x_column]\
       < lhs_bdry, data[:,x_column] > rhs_bdry)), axis=0)
      for j in range(0, len(short_dat[:,x_column])):
        if j==0:
          a_mat = [[short_dat[j,x_column], 1.]]
          b_vec = [short_dat[j,y_column]]
        else:
          a_mat.append([short_dat[j,x_column], 1.])
          b_vec.append(short_dat[j,y_column])
    #solve system
      a_mat_trans = np.transpose(a_mat)
      a_tr_a_mat = np.dot(a_mat_trans, a_mat)
      a_tr_b_vec = np.dot(a_mat_trans, b_vec)
      x_vec = np.linalg.solve(a_tr_a_mat, a_tr_b_vec)
    #output data
```

```
  output.append([count, 1., np.amin(short_dat[:,x_column]), \
  np.amax(short_dat[:,x_column]), 0., 0., x_vec[0], x_vec[1]])
#increase count...
  count=count+1.
#export data
  with open(export_file, 'wb') as f:
    writer = csv.writer(f)
    for row in output:
    writer.writerow(row)
#plot affine fit
  plt.plot(short_dat[:,x_column], x_vec[0]*short_dat[:,x_column] + \
  x_vec[1], color_line[int(np.mod(count,1.*len(color_line))-1)])
  plt.show()

else:
#intermediary location least-squares affine fit
#use a cubic spline to enforce continuity...
  short_dat = np.delete(data, np.where(np.logical_or(data[:,x_column]\
   < lhs_bdry, data[:,x_column] > rhs_bdry)), axis=0)
  for j in range(0, len(short_dat[:,x_column])):
    if j==0:
      a_mat = [[short_dat[j,x_column], 1.]]
      b_vec = [short_dat[j,y_column]]
    else:
      a_mat.append([short_dat[j,x_column], 1.])
      b_vec.append(short_dat[j,y_column])
#solve system
  a_mat_trans = np.transpose(a_mat)
  a_tr_a_mat = np.dot(a_mat_trans, a_mat)
  a_tr_b_vec = np.dot(a_mat_trans, b_vec)
  x_vec = np.linalg.solve(a_tr_a_mat, a_tr_b_vec)
#output data
  output.append([count, 1., np.amin(short_dat[:,x_column]), \
  np.amax(short_dat[:,x_column]), 0., 0., x_vec[0], x_vec[1]])
#increase count...
  count=count+1.
```

```
    #export data
      with open(export_file, 'wb') as f:
        writer = csv.writer(f)
        for row in output:
        writer.writerow(row)
    #plot affine fit
      plt.plot(short_dat[:,x_column], x_vec[0]*short_dat[:,x_column] + \
      x_vec[1], color_line[int(np.mod(count,1.*len(color_line))-1)])
      plt.show()

#=========================================================================
  elif event.key=='2':
    if count==0.:
    #standard least-squares quadratic fit
      short_dat = np.delete(data, np.where(np.logical_or(data[:,x_column]\
       < lhs_bdry, data[:,x_column] > rhs_bdry)), axis=0)
      for j in range(0, len(short_dat[:,x_column])):
        if j==0:
          a_mat = [[np.power(short_dat[j,x_column], 2.), \
          short_dat[j,x_column], 1.]]
          b_vec = [short_dat[j,y_column]]
        else:
          a_mat.append([np.power(short_dat[j,x_column], 2.), \
          short_dat[j,x_column], 1.])
          b_vec.append(short_dat[j,y_column])
    #solve system
      a_mat_trans = np.transpose(a_mat)
      a_tr_a_mat = np.dot(a_mat_trans, a_mat)
      a_tr_b_vec = np.dot(a_mat_trans, b_vec)
      x_vec = np.linalg.solve(a_tr_a_mat, a_tr_b_vec)
    #output data
      output.append([count, 2., np.amin(short_dat[:,x_column]), \
      np.amax(short_dat[:,x_column]), 0., x_vec[0], x_vec[1], x_vec[2]])
    #increase count...
      count=count+1.
    #export data
```

```
  with open(export_file, 'wb') as f:
    writer = csv.writer(f)
    for row in output:
    writer.writerow(row)
#plot quadratic fit
  plt.plot(short_dat[:,x_column], \
  x_vec[0]*np.power(short_dat[:,x_column],2.) + \
  x_vec[1]*short_dat[:,x_column] + x_vec[2], \
  color_line[int(np.mod(count,1.*len(color_line))-1)])
  plt.show()

else:
#constrained least-squares quadratic fit
  short_dat = np.delete(data, np.where(np.logical_or(data[:,x_column]\
   < lhs_bdry, data[:,x_column] > rhs_bdry)), axis=0)
  for j in range(0, len(short_dat[:,x_column])):
    if j==0:
      a_mat = [[np.power(short_dat[j,x_column], 2.), \
      short_dat[j,x_column], 1.]]
      b_vec = [short_dat[j,y_column]]
    else:
      a_mat.append([np.power(short_dat[j,x_column], 2.), \
      short_dat[j,x_column], 1.])
      b_vec.append(short_dat[j,y_column])
#specify initial point and slope...
  short_dat2 = np.delete(data, np.where(data[:,x_column] < \
  lhs_bdry), axis=0)
  lhs_fit_bdry = np.amin(short_dat2[:,x_column])
  x_0 = lhs_fit_bdry;
  y_0 = output[-1][4]*x_0*x_0*x_0 + output[-1][5]*x_0*x_0 + \
  output[-1][6]*x_0 + output[-1][7];
  slope = 3.*output[-1][4]*x_0*x_0 + 2.*output[-1][5]*x_0 + \
  output[-1][6];
#initial guess and constraints for optimization
  guess = np.polyfit(short_dat[:,x_column], short_dat[:,y_column], 2)
  cons = ({'type': 'eq', 'fun': lambda guess: 2.*guess[0]*x_0 + \
```

```
      guess[1] - slope},
      {'type': 'eq', 'fun': lambda guess: guess[0]*np.power(x_0, 2.) + \
      guess[1]*x_0 + guess[2] - y_0})
    #solve optimization
    #x_vec is the optimized solution of the 'guess' array values...
      res = sp.optimize.minimize(objective, guess, args=(b_vec, a_mat), \
      method='SLSQP', constraints=cons)
      x_vec = res.x
    #output data
      output.append([count, 2., np.amin(short_dat[:,x_column]), \
      np.amax(short_dat[:,x_column]), 0.0, x_vec[0], x_vec[1], x_vec[2]])
    #increase count...
      count=count+1.
    #export data
      with open(export_file, 'wb') as f:
        writer = csv.writer(f)
        for row in output:
        writer.writerow(row)
    #plot quadratic fit
      plt.plot(short_dat[:,x_column], \
      x_vec[0]*np.power(short_dat[:,x_column],2.) + \
      x_vec[1]*short_dat[:,x_column] + x_vec[2], \
      color_line[int(np.mod(count,1.*len(color_line))-1)])
      plt.show()

#=============================================================================
  elif event.key=='3':
    if count==0.:
    #standard least-squares cubic fit
      short_dat = np.delete(data, np.where(np.logical_or(data[:,x_column]\
       < lhs_bdry, data[:,x_column] > rhs_bdry)), axis=0)
      for j in range(0, len(short_dat[:,x_column])):
        if j==0:
          a_mat = [[np.power(short_dat[j,x_column], 3.), \
          np.power(short_dat[j,x_column], 2.), \
          short_dat[j,x_column], 1.]]
```

```
      b_vec = [short_dat[j,y_column]]
    else:
      a_mat.append([np.power(short_dat[j,x_column], 3.), \
      np.power(short_dat[j,x_column], 2.), \
      short_dat[j,x_column], 1.])
      b_vec.append(short_dat[j,y_column])
#solve system...
  a_mat_trans = np.transpose(a_mat)
  a_tr_a_mat = np.dot(a_mat_trans, a_mat)
  a_tr_b_vec = np.dot(a_mat_trans, b_vec)
  x_vec = np.linalg.solve(a_tr_a_mat, a_tr_b_vec)
#output data
  output.append([count, 3., np.amin(short_dat[:,x_column]), \
  np.amax(short_dat[:,x_column]), x_vec[0], x_vec[1], x_vec[2], \
  x_vec[3]])
#increase count...
  count=count+1.
#export data
  with open(export_file, 'wb') as f:
    writer = csv.writer(f)
    for row in output:
    writer.writerow(row)
#plot cubic fit
  plt.plot(short_dat[:,x_column], \
  x_vec[0]*np.power(short_dat[:,x_column],3.) + \
  x_vec[1]*np.power(short_dat[:,x_column],2.) + \
  x_vec[2]*short_dat[:,x_column] + x_vec[3], \
  color_line[int(np.mod(count,1.*len(color_line))-1)])
  plt.show()

else:
#constrained least-squares cubic fit
  short_dat = np.delete(data, np.where(np.logical_or(data[:,x_column]\
   < lhs_bdry, data[:,x_column] > rhs_bdry)), axis=0)
  for j in range(0, len(short_dat[:,x_column])):
    if j==0:
```

```
      a_mat = [[np.power(short_dat[j,x_column], 3.), \
      np.power(short_dat[j,x_column], 2.), \
      short_dat[j,x_column], 1.]]
      b_vec = [short_dat[j,y_column]]
    else:
      a_mat.append([np.power(short_dat[j,x_column], 3.), \
      np.power(short_dat[j,x_column], 2.), \
      short_dat[j,x_column], 1.])
      b_vec.append(short_dat[j,y_column])
#specify initial point and slope...
  short_dat2 = np.delete(data, np.where(data[:,x_column] < lhs_bdry),\
   axis=0)
  lhs_fit_bdry = np.amin(short_dat2[:,x_column])
  x_0 = lhs_fit_bdry;
  y_0 = output[-1][4]*x_0*x_0*x_0 + output[-1][5]*x_0*x_0 + \
  output[-1][6]*x_0 + output[-1][7];
  slope = 3.*output[-1][4]*x_0*x_0 + 2.*output[-1][5]*x_0 + \
  output[-1][6];
#initial guess and constraints for optimization
  guess = np.polyfit(short_dat[:,x_column], short_dat[:,y_column], 3)
  cons = ({'type': 'eq', 'fun': lambda guess: 3.*guess[0]*x_0*x_0 + \
  2.*guess[1]*x_0 + guess[2] - slope},
  {'type': 'eq', 'fun': lambda guess: guess[0]*x_0*x_0*x_0 + \
  guess[1]*x_0*x_0 + guess[2]*x_0 + guess[3] - y_0})
#solve optimization
#x_vec is the optimized solution of the 'guess' array values...
  res = sp.optimize.minimize(objective, guess, args=(b_vec, a_mat), \
  method='SLSQP', constraints=cons)
  x_vec = res.x
#output data
  output.append([count, 3., np.amin(short_dat[:,x_column]), \
  np.amax(short_dat[:,x_column]), x_vec[0], x_vec[1], x_vec[2], \
  x_vec[3]])
#increase count
  count=count+1.
#export data
```

```
      with open(export_file, 'wb') as f:
        writer = csv.writer(f)
        for row in output:
        writer.writerow(row)
    #plot cubic fit
      plt.plot(short_dat[:,x_column], \
      x_vec[0]*np.power(short_dat[:,x_column],3.) + \
      x_vec[1]*np.power(short_dat[:,x_column],2.) + \
      x_vec[2]*short_dat[:,x_column] + x_vec[3], \
      color_line[int(np.mod(count,1.*len(color_line))-1)])
      plt.show()

#=========================================================================
  elif event.key=='4':
    if count==0.:
    #coupled cubic and linear fit...
      short_dat = np.delete(data, np.where(np.logical_or(data[:,x_column]\
       < lhs_bdry, data[:,x_column] > rhs_bdry)), axis=0)
    #initial guess and constraints for optimization
    #guess[0]-guess[3] are the a-d constants of the polynomial
    #guess[4] is the point where the cubic fit transitions to an affine fit
      guess_pre=np.polyfit(short_dat[:,x_column],short_dat[:,y_column],3)
      guess = [guess_pre[0], guess_pre[1], guess_pre[2], guess_pre[3], \
      0.5*(np.amin(short_dat[:,x_column])+np.amax(short_dat[:,x_column]))]

      cons = ({'type': 'eq', 'fun': lambda guess: \
      (3.*guess[0]*guess[4]*guess[4] + 2.*guess[1]*guess[4] + guess[2]) -\
       (3.*guess[0]*guess[4]*guess[4]+2.*guess[1]*guess[4]+guess[2])},
      #^^^derivative continuity...
      {'type': 'eq', 'fun': lambda guess: \
      (guess[0]*guess[4]*guess[4]*guess[4] +guess[1]*guess[4]*guess[4] + \
      guess[2]*guess[4] + guess[3]) - ((3.*guess[0]*guess[4]*guess[4]+ \
      2.*guess[1]*guess[4]+guess[2])*guess[4] + \
      -2.*guess[0]*guess[4]*guess[4]*guess[4]-guess[1]*guess[4]*guess[4]+\
      guess[3])})  #function continuity...
    #solve optimization
```

```
#x_vec is the optimized solution of the 'guess' array values...
  res = sp.optimize.minimize(objective2, guess, args=(short_dat, \
  lhs_bdry, rhs_bdry), method='SLSQP', constraints=cons, \
  options={'disp':True,'ftol': 1e4})
  x_vec = res.x
#output data
  output.append([count, 3., np.amin(short_dat[:,x_column]), x_vec[4],\
   x_vec[0], x_vec[1], x_vec[2], x_vec[3]])
  output.append([count, 1., x_vec[4], np.amax(short_dat[:,x_column]),\
   0.,0.,3.*x_vec[0]*x_vec[4]*x_vec[4]+2.*x_vec[1]*x_vec[4]+x_vec[2],\
  -2.*x_vec[0]*x_vec[4]*x_vec[4]*x_vec[4]-x_vec[1]*x_vec[4]*x_vec[4]+\
  x_vec[3]])
#increase count...
  count=count+1.
#export data
  with open(export_file, 'wb') as f:
    writer = csv.writer(f)
    for row in output:
    writer.writerow(row)
#plot cubic and affine fits
  cubic_fit = np.linspace(np.amin(short_dat[:,x_column]), x_vec[4], \
  100);
  affine_fit = np.linspace(x_vec[4], np.amax(short_dat[:,x_column]), \
  100);
  plt.plot(cubic_fit, x_vec[0]*np.power(cubic_fit,3.) + \
  x_vec[1]*np.power(cubic_fit,2.) +x_vec[2]*cubic_fit + x_vec[3], \
  color_line[int(np.mod(count,1.*len(color_line))-1)])
  plt.plot(affine_fit, (3.*x_vec[0]*x_vec[4]*x_vec[4]+\
  2.*x_vec[1]*x_vec[4]+x_vec[2])*affine_fit + \
  (-2.*x_vec[0]*x_vec[4]*x_vec[4]*x_vec[4]-\
  x_vec[1]*x_vec[4]*x_vec[4]+x_vec[3]), \
  color_line[int(np.mod(count,1.*len(color_line))-1)])
  plt.show()

else:
#additionally-constrainsed, coupled cubic and linear fit...
```

```
  short_dat = np.delete(data, np.where(np.logical_or(data[:,x_column]\
   < lhs_bdry, data[:,x_column] > rhs_bdry)), axis=0)
#specify initial point and slope...
  short_dat2 = np.delete(data, np.where(data[:,x_column] < lhs_bdry),\
   axis=0)
  lhs_fit_bdry = np.amin(short_dat2[:,x_column])
  x_0 = lhs_fit_bdry;
  y_0 = output[-1][4]*x_0*x_0*x_0 + output[-1][5]*x_0*x_0 + \
  output[-1][6]*x_0 + output[-1][7];
  slope = 3.*output[-1][4]*x_0*x_0 + 2.*output[-1][5]*x_0 + \
  output[-1][6];
#initial guess and constraints for optimization
#guess[0]-guess[3] are the a-d constants of the polynomial
#guess[4] is the point where the cubic fit transitions to an affine fit
  guess_pre=np.polyfit(short_dat[:,x_column],short_dat[:,y_column],3)
  guess = [guess_pre[0], guess_pre[1], guess_pre[2], guess_pre[3], \
  0.5*(np.amin(short_dat[:,x_column])+np.amax(short_dat[:,x_column]))]
  cons = ({'type': 'eq', 'fun': lambda guess: 3.*guess[0]*x_0*x_0 + \
  2.*guess[1]*x_0 + guess[2] - slope},  #function continuity
  #...(from section b/f)
  {'type': 'eq', 'fun': lambda guess: guess[0]*x_0*x_0*x_0 + \
  guess[1]*x_0*x_0 + guess[2]*x_0 + guess[3] - y_0},  #derivative
  #...continuity (from section b/f)
  {'type': 'eq', 'fun': lambda guess: (3.*guess[0]*guess[4]*guess[4]+\
   2.*guess[1]*guess[4] + guess[2]) - (3.*guess[0]*guess[4]*guess[4]+\
  2.*guess[1]*guess[4]+guess[2])},   #derivative continuity...
  {'type': 'eq', 'fun': lambda guess: \
  (guess[0]*guess[4]*guess[4]*guess[4] +guess[1]*guess[4]*guess[4] + \
  guess[2]*guess[4] + guess[3]) - ((3.*guess[0]*guess[4]*guess[4]+\
  2.*guess[1]*guess[4]+guess[2])*guess[4] + \
  -2.*guess[0]*guess[4]*guess[4]*guess[4]-guess[1]*guess[4]*guess[4]+\
  guess[3])})  #function continuity...
#solve optimization
#x_vec is the optimized solution of the 'guess' array values...
  res = sp.optimize.minimize(objective2, guess, args=(short_dat, \
  lhs_bdry, rhs_bdry), method='SLSQP', constraints=cons, \
```

```
      options={'disp':True,'ftol': 1e4})
      x_vec = res.x
    #output data
      output.append([count, 3., np.amin(short_dat[:,x_column]), x_vec[4],\
       x_vec[0], x_vec[1], x_vec[2], x_vec[3]])
      output.append([count, 1., x_vec[4], np.amax(short_dat[:,x_column]),\
       0.,0.,3.*x_vec[0]*x_vec[4]*x_vec[4]+2.*x_vec[1]*x_vec[4]+x_vec[2],\
      -2.*x_vec[0]*x_vec[4]*x_vec[4]*x_vec[4]-x_vec[1]*x_vec[4]*x_vec[4]+\
      x_vec[3]])
    #increase count
      count=count+1.
    #export data
      with open(export_file, 'wb') as f:
        writer = csv.writer(f)
        for row in output:
        writer.writerow(row)
    #plot cubic and affine fits
      cubic_fit=np.linspace(np.amin(short_dat[:,x_column]), x_vec[4],100);
      affine_fit=np.linspace(x_vec[4],np.amax(short_dat[:,x_column]),100);
      plt.plot(cubic_fit, x_vec[0]*np.power(cubic_fit,3.) + \
      x_vec[1]*np.power(cubic_fit,2.) +x_vec[2]*cubic_fit + x_vec[3], \
      color_line[int(np.mod(count,1.*len(color_line))-1)])
      plt.plot(affine_fit, (3.*x_vec[0]*x_vec[4]*x_vec[4]+\
      2.*x_vec[1]*x_vec[4]+x_vec[2])*affine_fit + \
      (-2.*x_vec[0]*x_vec[4]*x_vec[4]*x_vec[4]-x_vec[1]*x_vec[4]*x_vec[4]\
      +x_vec[3]), color_line[int(np.mod(count,1.*len(color_line))-1)])
      plt.show()
#=============================================================================
  fig.canvas.draw()
  #end of on_key event...


def on_click(event):
  #event.button gives the button number
  #event.x gives the x pixel of the plot
  #event.y gives the y pixel of the plot
```

```
  #event.xdata gives the x data point value of the plot
  #event.ydata gives the y data point value of the plot
  #print 'button=%d,x=%d,y=%d,xdata=%f ydata=%f'%(event.button, event.x,\
  #...event.y, event.xdata, event.ydata)
  global lhs_bdry, rhs_bdry, aff_guess1, aff_guess2
  button=event.button
  x=event.xdata
  y=event.ydata

  if button==1:  #left mouse button click is 1
    plt.plot(x,y,'b|')
    lhs_bdry = event.xdata

  elif button==3:  #right mouse button click is 3
    plt.plot(x,y,'m|')
    rhs_bdry = event.xdata

  else:  #center mouse button click is 2
    aff_guess2 = aff_guess1;
    aff_guess1 = event.xdata
    plt.plot(x,y,'ro')
    print('(x,y): ('+str(np.round(x,6))+','+str(np.round(y,6))+')')
#=============================================================================
  fig.canvas.draw()
  #end of on_click event...

#columns of data file used for curve fitting
x_column = 0
y_column = 1

data = np.genfromtxt('example_fitting_data.csv',delimiter=',',skip_header=1)

count=0.;  #used to specify section number

#specify the region where you will fit data
lhs_bdry = np.amin(data[:,x_column]); rhs_bdry = np.amax(data[:,x_column]);
```

```
#specify region where you want to plot and affine fit--note, no data\
#...will be saved from fit...
aff_guess1=np.amin(data[:,x_column]); aff_guess2=np.amax(data[:,x_column])

#plot the average value of a specified section
steady_state_x_value = 0.

export_file = 'fitting_data_export.csv'
output=[['sect.','polynomial order','x_left','x_right','x^3','x^2','x','1']]



#sort data to ensure increasing x
data = data[data[:,x_column].argsort()]

fig = plt.figure(0)
plt.plot(data[:,x_column], data[:,y_column], 'k.')
plt.xlabel('x-axis label (-)', size=text_size)
plt.ylabel('y-axis label (-)', size=text_size)
fig.canvas.mpl_connect('button_press_event', on_click)
fig.canvas.mpl_connect('key_press_event', on_key)
plt.show()
```

BIBLIOGRAPHY

[1] ABAQUS version 6.14-1. User Documentation, Dassault Systems, 2014.

[2] Yang, Q. D., Thouless, M. D., and Ward, S. M. Numerical Simulations of Adhesively-Bonded Beams Failing with Extensive Plastic Deformation. *Journal of the Mechanics and Physics of Solids*, 1999. 47(6):1337–1353.

[3] Yang, Q. D. and Thouless, M. D. Mixed-mode fracture analyses of plastically-deforming adhesive joints. *International Journal of Fracture*, 2001. 110:175–187.

[4] Sun, C., Thouless, M. D., Waas, A. M., Schroeder, J. A., and Zavattieri, P. D. Rate effects for mixed-mode fracture of plastically-deforming, adhesively-bonded structures. *International Journal of Adhesion and Adhesives*, 2008. 29(4):434–443.

[5] Anderson, T. L. *Fracture Mechanics*. Taylor & Francis, 3rd edition, 2005. ISBN 0849316561.

[6] Griffith, A. A. The Phenomena of Rupture and Flow in Solids. *Philosophical Transactions of the Royal Society A: Mathematical, Physical and Engineering Sciences*, 1920. 221(582-593):163–198.

[7] Paris, P. C. Cleavage fracture: An overview of some historical aspects to honor G. R. Irwin. *Engineering Fracture Mechanics*, 1998. 59(4):411–413.

[8] Irwin, G. Linear fracture mechanics, fracture transition, and fracture control. *Engineering Fracture Mechanics*, 1968. 1(2):241–257.

[9] Dugdale, D. S. Yielding of steel sheets containing slits. *Journal of the Mechanics and Physics of Solids*, 1960. 8(2):100–104.

[10] Barenblatt, G. I. The mathematical theory of equilibrium cracks in brittle fracture. *Advances in Applied Mechanics*, 1962. 7:55–129.

[11] Modéer, A., Hillerborg, M., and Petersson, P.-E. Analysis of crack formation and crack growth in concrete by means of fracture mechanics and finite elements. *Cement and Concrete research*, 1976. 6:773–782.

[12] Needleman, A. A Continuum Model for Void Nucleation by Inclusion Debonding. *Journal of Applied Mechanics*, 1987. 54(3):525.

[13] Xu, X. P. and Needleman, A. Void nucleation by inclusion debonding in a crystal matrix. *Modelling and Simulation in Materials Science and Engineering*, 1993. 1(2):111–132.

[14] Park, K., Paulino, G. H., and Roesler, J. R. A unified potential-based cohesive model of mixed-mode fracture. *Journal of the Mechanics and Physics of Solids*, 2009. 57(6):891–908.

[15] Sørensen, B. F. and Jacobsen, T. K. Determination of cohesive laws by the J integral approach. *Engineering Fracture Mechanics*, 2003. 70(14):1841–1858.

[16] Li, S., Thouless, M. D., Waas, A. M., Schroeder, J. A., and Zavattieri, P. D. Mixed-mode cohesive-zone models for fracture of an adhesively bonded polymermatrix composite. *Engineering Fracture Mechanics*, 2006. 73(1):64–78.

[17] Li, S., Thouless, M. D., Waas, A. M., Schroeder, J. A., and Zavattieri, P. D. Competing failure mechanisms in mixed-mode fracture of an adhesively bonded polymer-matrix composite. *International Journal of Adhesion and Adhesives*, 2006. 26(8):609–616.

[18] Wang, J. S. and Suo, Z. Experimental determination of interfacial toughness using Brazil-nut-sandwich. *Acta Metallurgica*, 1990. 38:1279–1290.

[19] Hutchinson, J. W. and Suo, Z. Mixed Mode Cracking in Layered Materials. *Advances in Applied Mechanics*, 1992. 29:63–191.

[20] Kafkalidis, M. S. and Thouless, M. D. The effects of geometry and material properties on the fracture of single lap-shear joints. *International Journal of Solids and Structures*, 2002. 39(17):4367–4383.

[21] Cavalli, M. N., Thouless, M. D., and Yang, Q. D. Cohesive-zone modelling of the deformation and fracture of spot-welded joints. *Fatigue and Fracture of Engineering Materials and Structures*, 2005. 28(10):861–874.

[22] Fang, X. J., Zhou, Z. Q., Cox, B. N., and Yang, Q. D. High-fidelity simulations of multiple fracture processes in a laminated composite in tension. *Journal of the Mechanics and Physics of Solids*, 2011. 59(7):1355–1373.

[23] Yang, Q. D., Thouless, M. D., and Ward, S. M. Elasticplastic mode-II fracture of adhesive joints. *International Journal of Solids and Structures*, 2001. 38(18):3251–3262.

[24] Suo, Z. and Hutchinson, J. W. Interface crack between two elastic layers. *International Journal of Fracture*, 1990. 43(1):1–18.

[25] Dundurs, J. Edge-Bonded Dissimilar Orthogonal Elastic Wedges. *Journal of Applied Mechanics*, 1969. 36:650–652.

[26] Parmigiani, J. P. and Thouless, M. D. The effects of cohesive strength and toughness on mixed-mode delamination of beam-like geometries. *Engineering Fracture Mechanics*, 2007. 74(17):2675–2699.

[27] Sills, R. B. and Thouless, M. D. The effect of cohesive-law parameters on mixed-mode fracture. *Engineering Fracture Mechanics*, 2013. 109:353–368.

[28] Sills, R. B. and Thouless, M. D. Cohesive-length scales for damage and toughening mechanisms. *International Journal of Solids and Structures*, 2015. 55:32–43.

[29] Peters, W. H., Ranson, W. F., Sutton, M. A., Chu, T. C., and Anderson, J. Application of digital correlation methods to rigid body mechanics. *Optical Engineering*, 1983. 22(6):738–742.

[30] Sutton, M. A., Mingqi, C., Peters, W. H., Chao, Y. J., and McNeill, S. R. Application of an optimized digital correlation method to planar deformation analysis. *Image and Vision Computing*, 1986. 4(3):143–150.

[31] McNeill, S., Peters, W., and Sutton, M. Estimation of stress intensity factor by digital image correlation. *Engineering Fracture Mechanics*, 1987. 28(1):101–112.

[32] Luo, P. F., Chao, Y. J., Sutton, M. A., and Peters, W. H. Accurate measurement of three-dimensional deformations in deformable and rigid bodies using computer vision. *Experimental Mechanics*, 1993. 33(2):123–132.

[33] Cheng, P., Sutton, M. A., Schreier, H. W., and McNeill, S. R. Full-field speckle pattern image correlation with B-Spline deformation function. *Experimental Mechanics*, 2002. 42(3):344–352.

[34] Bornert, M., Brémand, F., Doumalin, P., Dupré, J.-C., Fazzini, M., Grédiac, M., Hild, F., Mistou, S., Molimard, J., Orteu, J.-J., Robert, L., Surrel, Y., Vacher, P., and Wattrisse, B. Assessment of Digital Image Correlation Measurement Errors: Methodology and Results. *Experimental Mechanics*, 2009. 49(3):353–370.

[35] Reedlunn, B., Daly, S., Hector, L., Zavattieri, P., and Shaw, J. A. Tips and tricks for characterizing shape memory wire part 5: Full-field strain measurement by digital image correlation. *Experimental Techniques*, 2010. 37(3):62–78.

[36] Baldi, A. Residual Stress Measurement Using Hole Drilling and Integrated Digital Image Correlation Techniques. *Experimental Mechanics*, 2014. 54(3):379–391.

[37] Kammers, A. D. and Daly, S. Self-Assembled Nanoparticle Surface Patterning for Improved Digital Image Correlation in a Scanning Electron Microscope. *Experimental Mechanics*, 2013. 53(8):1333–1341.

[38] Reu, P. L. Uncertainty Quantification for 3D Digital Image Correlation. In H. Jin, C. Sciammarella, C. Furlong, and S. Yoshida, editors, *Imaging Methods for Novel Materials and Challenging Applications, Volume 3*. Springer New York, New York, NY. ISBN 978-1-4614-4235-6, 2013 pages 311–317.

[39] LePage, W. S. Multiscale Investigation of Shape Memory Alloy Fatigue. Ph.D. thesis, University of Michigan, 2018.

[40] Daly, S. H. Digital Image Correlation in Experimental Mechanics for Aerospace Materials and Structures. In *Encyclopedia of Aerospace Engineering*. ISBN 9780470686652, 2010.

[41] Reu, P. L., Toussaint, E., Jones, E., Bruck, H. A., Iadicola, M., Balcaen, R., Turner, D. Z., Siebert, T., Lava, P., and Simonsen, M. DIC Challenge: Developing Images and Guidelines for Evaluating Accuracy and Resolution of 2D Analyses. *Experimental Mechanics*, 2018. 58(7):1067–1099.

[42] Li, S., Thouless, M. D., Waas, A. M., Schroeder, J. A., and Zavattieri, P. D. Use of mode-I cohesive-zone models to describe the fracture of an adhesively-bonded polymer-matrix composite. *Composites Science and Technology*, 2005. 65(2):281–293.

[43] Wu, C., Gowrishankar, S., Huang, R., and Liechti, K. M. On determining mixed-mode traction–separation relations for interfaces. *International Journal of Fracture*, 2016. 202:1–19.

[44] Zhu, Y., Liechti, K. M., and Ravi-Chandar, K. Direct extraction of rate-dependent tractionseparation laws for polyurea/steel interfaces. *International Journal of Solids and Structures*, 2009. 46(1):31–51.

[45] Obriemoff, J. W. The splitting strength of mica. *Proceedings of the Royal Society of London*, 1930. 127A:290–297.

[46] Sørensen, B. F., Horsewell, A., Jørgensen, O., Kumar, A. N., and Engbæk, P. Fracture resistance measurement method for in situ observation of crack mechanisms. *Journal of the American Ceramic Society*, 1998. 81:661–669.

[47] Sørensen, B. F., Jørgensen, K., Jacobsen, K. T., and Østergaard, R. C. {DCB}-specimen loaded with uneven bending moments. *International Journal of Fracture*, 2006. 141:163–176.

[48] ASTM 3433-99. Standard Test Method for Fracture Strength in Cleavage of Adhesives in Bonded Metal Joints, 1999.

[49] ASTM 5528-13. Standard Test Method for Mode I Interlaminar Fracture Toughness of Unidirectional Fiber-Reinforced Polymer Matrix Composites, 2013.

[50] British Standard 7991. Determination of the mode I adhesive fracture energy G_{IC} of structure adhesives using the double cantilever beam (DCB) and tapered double cantilever beam (TDCB) specimens, 2001.

[51] Gillis, P. P. and Gilman, J. J. Double-Cantilever Cleavage Mode of Crack Propagation. *Journal of Applied Physics*, 1964. 35(3):647–658.

[52] Kanninen, M. F. Augmented double cantilever beam model for studying crack propagation and arrest. *International Journal of Fracture*, 1973. 9:83–92.

[53] Mostovoy, S., Crosley, P. B., and Ripling, E. J. Use of crack-line-loaded specimens for measuring plane-strain fracture toughness. *Journal of Materials*, 1967. 2:661–681.

[54] Andrews, M. G. and Massabò, R. The effects of shear and near tip deformations on energy release rate and mode mixity of edge-cracked orthotropic layers. *Engineering Fracture Mechanics*, 2007. 74(17):2700–2720.

[55] Li, S., Wang, J., and Thouless, M. D. The Effects of Shear on Delamination of Beam-Like Geometries. *Journal of the Mechanics and Physics of Solids*, 2004. 52:193–214.

[56] Sun, C. T. and Pandey, R. K. Improved Method for Calculating Strain Energy Release Rate Based on Beam Theory. *AIAA Journal*, 1994. 32(1):184–189.

[57] Suo, Z., Bao, G., Fan, B., Wang, T. C., Fan, Z Suo, G Bao, B., Wang, T. C., Suo, Z., Bao, G., Fan, B., and Wang, T. C. Orthotropy rescaling and implications for fracture in composites. *International Journal of Solids and Structures*, 1991. 28(2):235–248.

[58] Wang, J. and Qiao, P. Mechanics of Bimaterial Interface: Shear Deformable Split Bilayer Beam Theory and Fracture. *Journal of Applied Mechanics*, 2005. 72(5):674.

[59] Wiederhorn, S. M., Shorb, A. M., and Moses, R. L. Critical Analysis of the Theory of the Double Cantilever Method of Measuring FractureSurface Energies. *Journal of Applied Physics*, 1968. 39(3):1569–1572.

[60] Williams, J. G. End corrections for orthotropic DCB specimens. *Composites Science and Technology*, 1989. 35(4):367–376.

[61] Thouless, M. D. Shear Forces, Root Rotations, Phase Angles and Delamination of Layered Materials. *Engineering Fracture Mechanics*, 2018. 191:153–167.

[62] Tamuzs, V., Tarasovs, S., and Vilks, U. Delamination properties of translaminar-reinforced composites. *Composites Science and Technology*, 2003. 63(10):1423–1431.

[63] de Moura, M. F. S. F., Morais, J. J. L., and Dourado, N. A new data reduction scheme for mode I wood fracture characterization using the double cantilever beam test. *Engineering Fracture Mechanics*, 2008. 75(13):3852–3865.

[64] Xu, W. and Guo, Z. A simple method for determining the mode I interlaminar fracture toughness of composite without measuring the growing crack length. *Engineering Fracture Mechanics*, 2018. 191:476–485.

[65] Rice, J. R. A Path Independent Integral and the Approximate Analysis of Strain Concentration by Notches and Cracks. *Journal of Applied Mechanics*, 1968. 35(2):379–386.

[66] Olsson, P. and Stigh, U. On the determination of the constitutive properties of thin interphase layers - an exact solution. *International Journal of Fracture*, 1989. 41(4):R71–R76.

[67] Paris, A. J. and Paris, P. C. Instantaneous evaluation of J and $Cˆ*$. *International Journal of Fracture*, 1988. 38:R19–R21.

[68] Williams, J. G. Large Displacement and End Block Effects in the DCB Interlaminar Test in Modes I and II. *Journal of Composite Materials*, 1987. 21:330–347.

[69] Li, V. C., Chan, C.-M., and Leung, C. K. Experimental determination of the tension-softening relations for cementitious composites. *Cement and Concrete Research*, 1987. 17:441–452.

[70] Desai, C. K., Basu, S., and Parameswaran, V. Determination of Traction Separation Law for Interfacial Failure in Adhesive Joints at Different Loading Rates. *The Journal of Adhesion*, 2016. 92:819–839.

[71] Rajan, S., Sutton, M. A., Fuerte, R., and Kidane, A. Traction-separation relationship for polymer-modified bitumen under Mode I loading: Double cantilever beam experiment with stereo digital image correlation. *Engineering Fracture Mechanics*, 2018. 187:404–421.

[72] Blaysat, B., Hoefnagels, J. P. M., Lubineau, G., Alfano, M., and Geers, M. G. D. Interface debonding characterization by image correlation integrated with double Cantilever Beam kinematics. *International Journal of Solids and Structures*, 2015. 55:79–91.

[73] Ruybalid, A., Hoefnagels, J. P. M., van der Sluis, O., van Maris, M., and Geers, M. G. D. Mixed-mode cohesive zone parameters from integrated digital image correlation on micrographs only. *International Journal of Solids and Structures*, 2019. 156-157:179–193.

[74] Shen, B. and Paulino, G. H. Direct Extraction of Cohesive Fracture Properties from Digital Image Correlation: A Hybrid Inverse Technique. *Experimental Mechanics*, 2011. 51:143–163.

[75] McMaster-Carr. Easy-to-Weld 4130 Alloy Steel Sheets and Bars. https://www.mcmaster.com/grade-4130-steel, Accessed: 26 April 2019.

[76] Liu, C., Rae, P. J., Cady, C. M., and Lovato, M. L. Damage and Fracture of High-Explosive Mock Subject to Cyclic Loading. In T. Proulx, editor, *Mechanics of Time-Dependent Materials and Processes in Conventional and Multifunctional Materials*, volume 3 of *Conference Proceedings of the Society for Experimental Mechanics Series*. Springer, New York, NY, USA, 2011 pages 151–157.

[77] Dow Automotive Systems. Total Solutions for Commercial Transportation. http://msdssearch.dow.com/PublishedLiteratureDOWCOM/dh_0894/0901b8038089473e.pdf, Accessed: 13 March 2018.

[78] Réthoré, J., Roux, S., and Hild, F. From pictures to extended finite elements: extended digital image correlation (X-DIC). *Comptes Rendus Mécanique*, 2007. 335(3):131–137.

[79] Réthoré, J., Hild, F., and Roux, S. Shear-band capturing using a multiscale extended digital image correlation technique. *Computer Methods in Applied Mechanics and Engineering*, 2007. 196(49-52):5016–5030.

[80] Barber, J. R. *Intermediate Mechanics of Materials*. Springer, Dordrecht, The Netherlands, 2011.

[81] Adams, R. D., Chambers, S. H., Del Strother, P. H. A., and Peppiatt, N. A. Rubber model for adhesive lap joints. *Journal of Strain Analysis*, 1973. 8(1):52–57.

[82] Adams, R. D. and Peppiatt, N. A. Stress analysis of adhesive-bonded lap joints. *Journal of Strain Analysis*, 1974. 9(3):185–196.

[83] Crocombe, A. D. and Adams, R. D. Influence of the Spew Fillet and other Parameters on the Stress Distribution in the Single Lap Joint. *The Journal of Adhesion*, 1981. 13(2):141–155.

[84] Adams, R. D. and Harris, J. A. The influence of local geometry on the strength of adhesive joints. *International Journal of Adhesion and Adhesives*, 1987. 7(2):69–80.

[85] Tsai, M. and Morton, J. The effect of a spew fillet on adhesive stress distributions in laminated composite single-lap joints. *Composite Structures*, 1995. 32(1-4):123–131.

[86] Tsai, M. and Morton, J. An experimental investigation of nonlinear deformations in single-lap joints. *Mechanics of Materials*, 1995. 20(3):183–194.

[87] Tsai, M., Oplinger, D., and Morton, J. Improved theoretical solutions for adhesive lap joints. *International Journal of Solids and Structures*, 1998. 35(12):1163–1185.

[88] ASTM D1002-10. Standard Test Method for Apparent Shear Strength of Single-Lap-Joint Adhesively Bonded Metal Specimens by Tension Loading (Metal-to-Metal), 2010.

[89] ASTM D5868-01. Standard Test Method for Lap Shear Adhesion for Fiber Reinforced Plastic (FRP) Bonding, 2014.

[90] Fernlund, G., Papini, M., McCammond, D., and Spelt, J. K. Fracture load predictions for adhesive joints. *Composites Science and Technology*, 1994. 51(4):587–600.

[91] Mohammed, I. and Liechti, K. M. Cohesive zone modeling of crack nucleation at bimaterial corners. *Journal of the Mechanics and Physics of Solids*, 2000. 48(4):735–764.

[92] Meng, F. Stochastic Aspects of Crack Propagation: Experiments and Cohesive-zone Modeling. Ph.D. thesis, University of Michigan, 2018.

[93] Barber, J. R. *Elasticity*. Springer, Dordrecht, The Netherlands, 2010.

[94] Churchman, C. M. and Hills, D. A. Slip zone length at the edge of a complete contact. *International Journal of Solids and Structures*, 2006. 43(7-8):2037–2049.

[95] Goland, M. and Reissner, E. The stresses in cemented joints. *Journal of Applied Mechanics*, 1944. 11:A17–A27.

[96] Moreira, D. C. and Nunes, L. C. Experimental analysis of bonded single lap joint with flexible adhesive. *Applied Adhesion Science*, 2014. 2(1):1–8.

[97] Razavi, S., Berto, F., Peron, M., and Torgersen, J. Parametric study of adhesive joints with non-flat sinusoid interfaces. *Theoretical and Applied Fracture Mechanics*, 2018. 93:44–55.

[98] Karachalios, E. F., Adams, R. D., and da Silva, L. F. M. Single lap joints loaded in tension with high strength steel adherends. *International Journal of Adhesion and Adhesives*, 2013. 43:81–95.

[99] Karachalios, E. F., Adams, R. D., and da Silva, L. F. M. Single lap joints loaded in tension with ductile steel adherends. *International Journal of Adhesion and Adhesives*, 2013. 43:96–108.

[100] Moya-Sanz, E. M., Ivañez, I., and Garcia-Castillo, S. K. Effect of the geometry in the strength of single-lap adhesive joints of composite laminates under uniaxial tensile load. *International Journal of Adhesion and Adhesives*, 2017. 72:23–29.

[101] Ruybalid, A. P., Hoefnagels, J. P. M., van der Sluis, O., and Geers, M. G. D. Image-based interface characterization with a restricted microscopic field of view. *International Journal of Solids and Structures*, 2018. 132:218–231.

[102] Love, A. E. H. *A treatise on the mathematical theory of elasticity*. Cambridge University Press, 1927.

[103] Cavalli, M. N., Thouless, M. D., and Yang, Q. D. Cohesive Modeling of the Deformation and Fracture of Weld-bonded Joints. *Welding Research*, 2004. 83(4):133–139.

[104] Li, S., Thouless, M. D., Waas, A. M., Schroeder, J. A., and Zavattieri, P. D. Use of a cohesive-zone model to analyze the fracture of a fiber-reinforced polymermatrix composite. *Composites Science and Technology*, 2005. 65(3):537–549.

[105] Williams, M. L. The stresses around a fault or crack in dissimilar media. *Bulletin of the Seismological Society of America*, 1959. 49(2):199–204.

[106] Williams, M. L. On the Stress Distributions at the Base of a Stationary Crack. *Journal of Applied Mechanics*, 1956. 24(1):109–114.

[107] Atkinson, C. On stress singularities and interfaces in linear elastic fracture mechanics. *International Journal of Fracture*, 1977. 13(6):807–820.

[108] Comninou, M. The Interface Crack. *Journal of Applied Mechanics*, 1977. 44(4):631–636.

[109] Comninou, M. Exterior interface cracks. *International Journal of Engineering Science*, 1980. 18(3):501–506.

[110] Goutianos, S. and Sørensen, B. F. Path dependence of truss-like mixed mode cohesive laws. *Engineering Fracture Mechanics*, 2012. 91:117–132.

[111] Thouless, M. D. Comments on extracting mixed-mode laws, 2017.

[112] Wu, C., Huang, R., and Liechti, K. M. Simultaneous extraction of tensile and shear interactions at interfaces. *Journal of the Mechanics and Physics of Solids*, 2019. 125:225–254.

[113] Rice, J. R. Elastic Fracture Mechanics Concepts for Interfacial Cracks. *Journal of Applied Mechanics*, 1988. 55(1):98.

[114] Pinto, A. M., Magalhães, A. G., Campilho, R. D., de Moura, M. F., and Baptista, A. P. Single-lap joints of similar and dissimilar adherends bonded with an acrylic adhesive. *Journal of Adhesion*, 2009. 85(6):351–376.

[115] Thouless, M. D. The effects of transverse shear on the delamination of edge-notch flexure and 3-point bend geometries. *Composites Part B: Engineering*, 2009. 40(4):305–312.

[116] Nelder, J. A. and Mead, R. A Simplex Method for Function Minimization. *The Computer Journal*, 1965. 7(4):308–313.

[117] Kennedy, J. and Eberhart, R. Particle Swarm Optimization. In *Proceedings of IEEE International Conference on Neural Networks*, volume IV. 1995 pages 1942–1948.

[118] Roux, S. and Hild, F. Stress intensity factor measurements from digital image correlation: post-processing and integrated approaches. *International Journal of Fracture*, jul 2006. 140(1-4):141–157.

[119] Hild, F. and Roux, S. Measuring stress intensity factors with a camera: Integrated digital image correlation (I-DIC). *Comptes Rendus Mécanique*, jan 2006. 334(1):8–12.

[120] Charbal, A., Dufour, J.-E., Guery, A., Hild, F., Roux, S., Vincent, L., and Poncelet, M. Integrated Digital Image Correlation considering gray level and blur variations: Application to distortion measurements of IR camera. *Optics and Lasers in Engineering*, mar 2016. 78:75–85.

[121] Kleinendorst, S., Hoefnagels, J., and Geers, M. Mechanical Shape Correlation: A novel integrated digital image correlation approach. *Computer Methods in Applied Mechanics and Engineering*, mar 2019. 345:983–1006.

[122] Barrett, J. and Foschi, R. Mode II stress-intensity factors for cracked wood beams. *Engineering Fracture Mechanics*, 1977. 9(2):371–378.

[123] Gillespie, J., Carlsson, L., and Pipes, R. Finite element analysis of the end notched flexure specimen for measuring mode II fracture toughness. *Composites Science and Technology*, 1986. 27(3):177–197.

[124] Hu, Z., Lu, W., and Thouless, M. Slip and wear at a corner with Coulomb friction and an interfacial strength. *Wear*, 2015. 338-339:242–251.

[125] Barber, J. R. *Contact Mechanics*. Springer International Publishing, 1st edition, 2018. ISBN 978-3-319-70938-3.

[126] Kirsch, A. *An Introduction to the Mathematical Theory of Inverse Problems*. Springer, New York, NY, USA, New York, NY, 2nd edition, 2011. ISBN 9781441984739.

[127] Guery, A., Hild, F., Latourte, F., and Roux, S. Identification of crystal plasticity parameters using DIC measurements and weighted FEMU. *Mechanics of Materials*, 2016. 100:55–71.

[128] Wang, Y., Coppieters, S., Lava, P., and Debruyne, D. Anisotropic yield surface identification of sheet metal through stereo finite element model updating. *Journal of Strain Analysis for Engineering Design*, 2016. 51(8):598–611.

[129] Grédiac, M. and Pierron, F. Applying the Virtual Fields Method to the identification of elasto-plastic constitutive parameters. *International Journal of Plasticity*, 2006. 22(4):602–627.

[130] Rossi, M., Pierron, F., and Štamborská, M. Application of the virtual fields method to large strain anisotropic plasticity. *International Journal of Solids and Structures*, 2016. 97_98:322–335.

[131] Fletcher, L., Lamberson, L., and Pierron, F. An Image-Based Approach for Measuring Dynamic Fracture Toughness. In J. Kimberley, L. E. Lamberson, and S. Mates, editors, *Dynamic Behavior of Materials, Volume 1*. Springer International Publishing, Cham. ISBN 978-3-319-95089-1, 2019 pages 247–250.

[132] Bay, B. K., Smith, T. S., Fyhrie, D. P., and Saad, M. Digital volume correlation: Three-dimensional strain mapping using x-ray tomography. *Experimental Mechanics*, 1999. 39(3):217–226.

[133] Bay, B. K. Methods and applications of digital volume correlation. *Journal of Strain Analysis for Engineering Design*, 2008. 43(8):745–760.

[134] Leclerc, H., Périé, J.-N., Roux, S., and Hild, F. Voxel-Scale Digital Volume Correlation. *Experimental Mechanics*, 2011. 51(4):479–490.

[135] Wang, B. and Pan, B. Self-Adaptive Digital Volume Correlation for Unknown Deformation Fields. *Experimental Mechanics*, 2019. 59(2):149–162.